GROWTH AND CHARACTERIZATION OF ALUMINUM EPITAXIAL LAYERS ON INAS QUANTUM WELL STRUCTURES FOR TOPOLOGICAL QUANTUM COMPUTING

by

Tiantian Wang

A Dissertation

Submitted to the Faculty of Purdue University

In Partial Fulfillment of the Requirements for the degree of

Doctor of Philosophy

Department of Physics and Astronomy

West Lafayette, Indiana

May 2021

THE PURDUE UNIVERSITY GRADUATE SCHOOL
STATEMENT OF COMMITTEE APPROVAL

Dr. Michael J. Manfra, Chair

Department of Physics and Astronomy

Dr. Michael A. Capano

School of Electrical and Computer Engineering

Dr. Rosa E. Diaz

Birck Nanotechnology Center

Dr. Oana Malis

Department of Physics and Astronomy

Dr. Martin Kruczenski

Department of Physics and Astronomy

Approved by:

Dr. John P. Finley

I dedicate this work to my family.

ACKNOWLEDGMENTS

First and foremost, I would like to express my deepest appreciation to my advisor, Professor Michael Manfra, for his constant support during the years of my Ph.D. He introduced me to the field of molecular beam epitaxy and helped me to establish my understanding of the techniques. During the work of my Ph.D., he provided clear directions towards the goal of the project, extensive mentoring that showed me how to think like a scientist, and invaluable expertise in multiple fields related to the work. It is my great honor to join Prof. Manfra's research group, which is the world-leading research group in the field.

I would also like to extend my deepest gratitude to Prof. Michael Capano and Dr. Rosa Diaz as my committee members and as collaborators of my Ph.D. work. Professor Capano's expertise in solid-state physics, transmission electron microscopy, and X-ray diffraction techniques are invaluable for me to learn from. His critical thinking always helped me to improve the consistency of my work. Dr. Diaz helped me with most TEM imaging and analysis in this thesis. Her great expertise in TEM techniques made difficult sample preparation and imaging feasible. She also sparked my interest in the field of microscopy.

I would also like to extend my sincere thanks to other members of my committee - Prof. Oana Malis and Prof. Martin Kruczenski, for their time and support during my thesis writing and defense.

I would like to acknowledge my colleagues in Manfra's Group MBE growth team. I would like to give my special thanks to Dr. Geoffrey Gardner. When I was new to the field of MBE growth, his mentoring made my transition to a skilled researcher in MBE techniques. I thank other members, including Dr. Candice Thomas, Dr. Sergei Gronin, Dr. Di Xiao, Dr. Jeffery Alex Webster, and Tyler Lindemann. It was my great pleasure to learn from you and work with you.

I would also like to acknowledge my colleagues in other teams in Manfra's Group, including Dr. Hatke, Dr. Kallaher, Dr. Fallahi, Dr. Nakamura, Dr. Wu, Dr. Ramirez, Dr. Qian, Dr. Roark, Shuang Liang, Teng Zhang, Sara Metti, and Lindsay Murphy, who shared knowledge in different fields and made scientific communications that helped me with my development as a researcher.

I would also like to acknowledge my colleagues that I worked with in the TEM lab, including Trang Nguyen, Xingtao Liu, and Brandon Dzuba, together with whom we learned TEM techniques and developed sample preparation techniques that satisfy special requirements of our sampless.

I would like to give my special thanks to Dr. Guo in the Department of Electrical and Computer Engineering for her efforts in image processing and MATLAB programming that helped me in developing the division methods in the analysis of TEM images.

Additionally, I would like to recognize the help and support I received from Purdue University and Birck Nanotechnology Center faculties and staff. Especially, I am grateful to Sandy Formica, who was always kind and helpful to all graduate students.

Finally, I am extremely grateful to my family for their forever love and support. This is my seventh years as a graduate student at Purdue University and my family was whom I cannot be together with during these years. However, their love was always together with me.

TABLE OF CONTENTS

LIST OF TABLES 8

LIST OF FIGURES 9

ABSTRACT 12

1 INTRODUCTION 13

1.1 Superconductor-semiconductor heterostructures for topological quantum computing 13

1.2 Aluminum deposition on semiconductors 15

1.2.1 Epitaxial orientation 16

1.2.2 Analysis of epitaxial interfaces 18

1.2.3 Growth modes of thin-film deposition 29

1.2.4 A summary of this section 36

2 EXPERIMENTAL METHODS 38

2.1 Aluminum Layer Growth 38

2.1.1 Introduction to molecular beam epitaxy (MBE) 38

2.1.2 MBE System setup for sample growth 39

2.1.3 MBE of the aluminum superconducting layer 44

2.2 Transmission Electron Microscopy (TEM) characterization 46

2.2.1 The electron-specimen interaction 46

2.2.2 The TEM imaging 48

2.2.3 TEM Sample Preparation 52

2.3 X-ray Diffraction (XRD) characterization 58

2.3.1 Principle of XRD characterization 58

2.3.2 Application of XRD in sample characterization 59

3 GROWTH ORIENTATION OF THE ALUMINUM FILMS 62

3.1 Sample growth 62

3.2 Characterization of growth orientation 64
3.3 Dependence of growth orientation of aluminum films 67
3.3.1 Lattice parameter of semiconductor 67
3.3.2 Residual strain in aluminum layer 68
3.3.3 Discussion 70

4 GRAIN PROPERTIES OF THE ALUMINUM FILMS 78
4.1 Grain properties of Al(111) 79
4.1.1 Cross-sectional TEM imaging and twin grains 79
4.1.2 Plan view TEM imaging of Al(111) 83
4.2 Grain properties of Al(110) 94
4.2.1 Cross-sectional TEM imaging 94
4.2.2 Plan view TEM imaging of Al(110) - Dark-field 95
4.2.3 Plan view TEM imaging of Al(110) - Bright-field 101
4.2.4 Discussion 109

REFERENCES 114

LIST OF TABLES

3.1 Identification and details for samples S1 - S7. 64

3.2 The relationship between growth orientation of Al and in-plane lattice parameter on the semiconductor surface. 68

3.3 Relationship between in-plane lattice parameters of semiconductor surface, Al normal strain, Al in-plane strain, and Al growth orientations. 70

LIST OF FIGURES

1.1 A schematic diagram of the coincidence lattice model. 19

1.2 A 3D ball-and-stick model of a piece of GaAs crystal with no surface reconstructions. 20

1.3 A schematic diagram of the ball-and-stick model of the epitaxial interface of two semiconductor layers. 20

1.4 A top-down view of the epitaxial interface of Al(001). 22

1.5 A cross-sectional schematic diagram of a possible atomic configuration of the aluminum layer formed near a surface step of GaAs. 23

1.6 A top-down view of the Al(001)-InAs interface. 25

1.7 A top-down view of the Al(111)-InAs interface. 27

1.8 A top-down view of the Al(110)-InAs interface. 29

1.9 A plot of the chemical potential as a function of the layer number. 31

1.10 The three growth modes in heteroepitaxy. 32

1.11 The work done in removing one Al atom from the side of each monolayer can be divided into side and vertical bond energy. 33

1.12 The number of vertical Al-Al bonds is different in different aluminum orientations. 35

2.1 Pictures of the MBE system. 40

2.2 A diagram of the important components in the main MBE chamber. 41

2.3 Cooling assembly in the metallization MBE chamber. 43

2.4 A typical layer stack of the Al-InAs quantum well heterostructure grown on an InP substrate. 44

2.5 Electron scattering signals in electron microscopy. 47

2.6 The TEM beam diagram when imaging a specimen using a parallel electron beam. 49

2.7 A schematic diagram of diffraction pattern and dark-field imaging in TEM. . . . 52

2.8 An example of grain orientation analysis using dark field TEM. 53

2.9 Traditional ion-milling technique of Cross-sectional TEM sample preparation. . 55

2.10 A normal FIB system contains SEM and FIB columns. 55

2.11 A schematic diagram of in-situ lift-out FIB process for cross-section TEM sample preparation. 56

2.12 A schematic diagram of H-bar FIB process for plan view TEM sample preparation. 57

2.13 Bragg's Law of X-ray Diffraction. 58

2.14 XRD symmetric scan configuration for growth orientation detection. 60
2.15 A typical RSM collected on a sample with layer stack Figure 2.4 using (224) reflection. 61
3.1 A sample can be described by its substrate, buffer layers, top layers, capping layer, and the deposited Al film. 63
3.2 An HRTEM image of aluminum layer with (111) orientation in sample S1. . . . 65
3.3 An HRTEM image of aluminum layer with (110) orientation in sample S4. . . . 67
3.4 Symmetric scan of (a) Al(111) reflection from sample S3 and (b) Al(220) reflection from S5. 69
3.5 A schematic illustration of a growing Al island on a semiconductor surface. . . . 71
3.6 The lattice parameter dependence of lattice mismatch between semiconductor and Al(111) and Al(110) films. 72
3.7 Cross-sectional HRTEM images of Al/Sm interfaces having Al growth orientations of (110) and (111) from S2. 75
3.8 The unfilled nearest neighboring positions of Al atoms on Al(110) and Al(111) surface. 77
4.1 A grain boundary analysis based on HRTEM images in S1 with (111) growth orientation. 80
4.2 The atomic arrangement near the twin boundary 1 in Figure 4.1. 81
4.3 The 180° rotated Al(111) crystal can be treated as stacking difference. 82
4.4 The diffraction pattern of the plan view sample of Al(111) film made in sample S3. 85
4.5 A g-vector of a double-diffraction beam is the vector resultant of the two g-vectors. 86
4.6 The double-diffraction pattern can be treated as semiconductor DP translated by an Al g-vector. 87
4.7 All double-diffracted reflections can be obtained by translating semiconductor DP with different Al g-vectors. 88
4.8 A dark-field TEM image of the plan view sample from S3. 90
4.9 The representative features in Figure 4.8. 91
4.10 The average-intercept method to determine the grain size in Al(111) film in S3. 93
4.11 An HRTEM image of the aluminum film in sample S4 with (110) growth orientation. 94
4.12 The configuration of two atomic layers of the Al(110) crystal. 95
4.13 The diffraction pattern of the plan view sample of Al(110) film made in sample S5. 96

4.14 The g-vector of the double-diffracted reflection is the vector resultant of g-vectors of Al and semiconductor. 97
4.15 A dark-field TEM image of the plan view sample from S5. 99
4.16 The blue curve plots the relationship between α and θ in Equation 4.16. 101
4.17 A bright-field TEM imaging of the thin area in the plan view sample from S5. . 102
4.18 An analysis of in-plane rotation based on HRTEM and FFT in the area near letter "A" in Figure 4.17 103
4.19 The first (top-left) image and its FFT of the 20×20 division of Figure 4.17. . . . 104
4.20 The rotation angle contour of Figure 4.17. 106
4.21 The rotation angle contour of Figure 4.17 overlapped with the original image. . 107
4.22 The rotation angle contour of a bright-field images of the Al/Sm overlapped area in the plan view sample from S5. 108
4.23 The average-intercept method to determine the grain size of Al(110) film in S5. 110
4.24 A schematic diagram of an aluminum film that contains grains. 110
4.25 The expected relationship between aluminum in-plane rotation angle and interfacial energy. 112

ABSTRACT

Superconductor-semiconductor heterostructures is studied for the applications in topological quantum computing. It has been approved that structural quality plays an important role in the application. This thesis focuses on the growth and characterization of Al films on InAs two-dimensional systems. The goal is to generate new knowledge and a complete understanding of the structural properties of the Al films that will lead to higher quality material for further research. The study of aluminum growth orientation and in-plane grain properties are presented.

To study the growth orientation of aluminum, the growth orientation of seven samples are characterized by cross-sectional TEM analysis and compared with the surface lattice parameter of the semiconductor (Sm) layers (characterized by RSM). A strong dependence is discovered. Al(111) films are grown on surfaces with a lower lattice parameter ($a < 5.98$ Å), while Al(110) films are grown on surfaces with a higher lattice parameter ($a > 5.98$ Å). One sample is observed to have an aluminum film with both (111) and (110) orientations. The transition of the growth orientation is related to the residual strain in Al film and the interfacial energy of the Al/Sm interface.

The grain properties of the Al films are studied using plan view TEM analysis. For Al(111) film, the diffraction pattern of plan view sample reveals $[-8°, 8°]$ in-plane rotation between grains. Clear grain boundaries are observed in dark-field imaging, which leads to an average grain size of 50 nm. For Al(110) film, the diffraction pattern of the plan view sample and the analysis of Al/Sm Moire fringes show the in-plane rotation is $[-1.5°, 1.5°]$, much smaller than Al(111). The average grain size of Al(110) film is also 50 nm. The difference in in-plane rotation angle reveals the difference in interfacial energy-angle dependence between Al(111) and Al(110) films.

1. INTRODUCTION

1.1 Superconductor-semiconductor heterostructures for topological quantum computing

Superconductor-semiconductor heterostructures have been studied for both fundamental physics and application prospects because of the possibility to observe and manipulate novel exotic phenomena. At the interface between the superconductor and the semiconductor, the Andreev reflection process allows the semiconductor to inherit properties of the superconductor while retaining the original properties of the semiconductor [1], [2].

In particular, an induced gap will appear in the density of state of the semiconductor, which is related to the superconducting energy gap in the density of state of the superconductor. This induced gap, along with the original properties of the semiconductor such as high spin-obit coupling and high g-factor, allows the possibility of driving the system through a topological phase transition [3]–[8]. In the topological phase, the quasiparticle excitations - the Majorana zero modes (MZMs) - obey non–abelian statistics and have been proposed as a candidate for fault-tolerant topological quantum computing [9]–[12], which gives a solution to the quantum decoherence problem [13]. In recent years, this proposal has attracted much interest from both material science and quantum transport research communities.

The first generation of the experiments simply used high spin-obit coupling III-V semiconductor nanowires (e.g. InAs or InSb) and put the nanowires in contact with superconducting material (e.g. Al, Nb or NbTiN). The transport experiments resulted in a zero-bias conductance peak, which showed strong evidence for the existence of the MZMs [14]–[16]. On the other hand, all these results showed states that have energy inside the proximity-induced gap which can lead to degradation of topological protection. This was called the softgap problem. A theoretical investigation has indicated that the source of the sub-gap states can be disorder (e.g., inhomogeneity of the superconductor/semiconductor interface) in the material[17]. This is a situation scientists have seen in the development of semiconductor technology. The disorder caused by the structural quality once limited the performance of devices and the discovery of fractional quantum Hall effect [18]. In 2015, Krogstrup et al., developed a method to epitaxially grow hybrid Al-InAs one-dimensional heterostructures

[19]. In their work, the superconducting aluminum layer was grown in the MBE system after the growth of the semiconductor nanowire, maintaining an *in-situ* condition. This prevented the semiconductor surface from being exposed to impurities. It is suggested in their work that growing at low temperatures allows the formation of a continuous aluminum crystalline film. This method resulted in clean semiconductor/superconductor interfaces and uniform single crystal morphology. In a separate article, an induced gap with minimal sub-gap states was demonstrated in one-dimensional system [20].

Research on the generation of MZMs in a two-dimensional system has also progressed. Compared to one-dimensional systems (e.g. nanowires), two-dimensional systems are more convenient because they can be handled more easily and perform large-scale engineering. However, one of the main challenges is the extremely large lattice mismatch between the semiconductor and superconductor, which gives rise to high strain in the superconductor layer that produces strain-induced defects. In a one-dimensional system, the strain can be partially relieved by the bending of the nanowire [19], which is not possible in a two-dimensional growth. Another challenge is that growth of two-dimensional semiconductor material, like InAs quantum well, is usually heterogeneous, for example, starting from an InP substrate, which requires more complex strain engineering to improved crystal properties [21], [22]. Defects and residual strain can exist on the surface, which makes the growth of a superconducting layer more complicated. In 2016, Shabani et al. reported that good morphology can be achieved by epitaxially growing aluminum superconducting layer on InAs quantum well structure [23]. Their results showed a proximity-induced gap close to the superconducting gap of aluminum, which indicated the 2-D systems may be a viable platform for topological quantum computing [23], [24]. X-ray diffraction (XRD) and transmission electron microscopy (TEM) experiments revealed well-crystallized aluminum layer. These promising results are the first steps toward fully-developed two-dimensional heterostructures that exhibit MZMs. A research opportunity has been created that calls for a deeper look into aluminum/semiconductor interfaces, including a more complete analysis of aluminum layer orientation and defects. It is the goal of this thesis to generate new knowledge pertaining to aluminum orientation and defects. In this work, we focus on Al-InAs two-dimensional system for experiments and discussion. A systematic investigation is performed on the topics

mentioned above providing a more complete understanding of aluminum growth on semiconductors that will lead to higher quality material for the research of topological quantum computing.

The growth of the aluminum layer is a multi-dimensional problem. Many parameters, such as deposition rate, substrate temperature, and the reconstruction of the semiconductor surface control the output of a growth experiment. The next section is dedicated to a brief review of previous investigations and established understanding germane to aluminum deposition on semiconductors.

1.2 Aluminum deposition on semiconductors

Aluminum deposition on semiconductors like GaAs or InAs is a heteroepitaxy process. The aluminum crystal and the semiconductor crystal are different both geometrically and energetically. The lattice parameter of the two materials are different ($a_{\mathrm{Al}} = 4.0495$, $a_{\mathrm{GaAs}} = 5.6532$ and $a_{\mathrm{InAs}} = 6.0583$) [25]. At the same time, the nature and the strength of the chemical bonds in aluminum and semiconductors are very different, too. III-V semiconductors such as GaAs and InAs are best described by covalent bonding. Each III atom contributes three electrons from its $4s$ and $4p$ subshells and each V atom contributes five electrons from its $4s$ and $4p$ subshells. The eight electrons in total are shared to form four near-covalent bonds. The bonds are directional: each III(V) atom is bonded with four neighboring V(III) atoms which are mutually separated by the tetrahedral bond angle 109.47° [26]. This is because of the angular property of the orbitals of the valence electrons [27]. On the other hand, aluminum is best described by metallic bonding. A good picture of metallic bonding is a gas of free electrons embedded by a lattice of positive ions. The electron gas works like glue which holds the metal ions together to form close-packed structures such as face-centered cubic (FCC) and body-centered cubic (BCC). Metallic bonding does not have directional property in contrast to covalent bonding [27]. Therefore, an interface between the aluminum crystal and the semiconductor crystal requires a transition from covalent bonding to metallic bonding. Based on the above reason, heteroepitaxial processes have substantial

complications compared to homoepitaxy. These complications include defect generation, residual strain, unexpected epitaxial orientation, and impact on active growth mode. In this section, a general discussion about epitaxial orientation and growth modes, as well as the application of established understanding on the topic of aluminum deposition are presented.

1.2.1 Epitaxial orientation

In perfect homoepitaxial growth conditions, the deposited crystal adopts the same crystal orientation of the substrate. For example, GaAs grown on a GaAs(001) substrate aligns its [001] direction with the normal direction of the surface as well as aligning its $[1\bar{1}0]$ direction with the same direction of the substrate [28]. This makes sense because each atom attached to the substrate crystal finds the lowest energy configuration by following the original structure of the crystal.

The above orientation is written as GaAs(001)$[1\bar{1}0]$ ∥ GaAs(001)$[1\bar{1}0]$ for easier discussion. Note "( )" instead of "[ ]" is used to mark the alignment along the surface normal direction, or growth orientation in this notation. This notation is consistently used throughout the thesis. In the above notation, it is immediately seen that the [001] direction of the deposit crystal and the substrate are parallel, while the $[1\bar{1}0]$ direction of the deposit crystal and the substrate are parallel as well. The parallelism of the corresponding directions between the deposit crystal and the substrate is called "parallel epitaxial orientation". This also happens in some of the heteroepitaxial processes. For example, in the deposition of copper on Ag(111) surface, in certain growth condition, Cu(111)$[1\bar{1}0]$ ∥ Ag(111)$[1\bar{1}0]$ was observed [29].

Parallel epitaxial orientation is not always the case in heteroepitaxial growth. Take the deposition of silver on GaAs(001) as an example. Both silver and GaAs have a face-centered cubic (FCC) structure (GaAs has a zinc blende stucture which is based on FCC). At a growth temperature higher than 200 °C, the silver deposited on As-terminated GaAs(001) surface showed parallel epitaxial orientation Ag(001)$[1\bar{1}0]$ ∥ GaAs(001)$[1\bar{1}0]$ [30]–[32]. However, at growth temperature lower than 200 °C, the same material system showed alignment

of Ag(110)[1$\bar{1}$1] ‖ GaAs(001)[1$\bar{1}$0] [30]–[32]. The non-parallel epitaxial alignments were also observed in other metal-semiconductor systems, such as Ag(110)[1$\bar{1}$0] ‖ InP(001)[110] [33], [34] and Au(001)[100] ‖ InP(001)[110] [34]. The existence of various epitaxial alignments reflected the interaction between the deposited crystal and the substrate across the epitaxial interface as well as kinetic effects determined by substrate temperature and other growth conditions.

Aluminum deposition on III-V semiconductors was studied by previous researchers. For Al on GaAs(001) surface, three types of epitaxial orientation were observed: Al(001)[100] ‖ GaAs(001)[1$\bar{1}$0] [31], [35]–[39], Al(110)[$\bar{1}$10] ‖ GaAs (001)[1$\bar{1}$0] [31], [36]–[38], [40], and Al(110)[001] ‖ GaAs (001)[1$\bar{1}$0] [37], [38]. Among these references, some of them observed multiple types of Al orientation presented in varying proportions and discussed how growth conditions affected the orientations. Although some disagreement existed on the proportion of (110) and (001) grains, there are some general agreements. Reference [31] and [36] stated the aluminum layer preferred (110) orientation more than (001) orientation in higher substrate temperature. Reference [36] also stated that the (110) orientation was more preferred with lower growth rates. Reference [31], [36], [37], and [38] studied the effect of the semiconductor surface reconstruction. They were in agreement that Ga-stablized (4×6) surface generated only (001) orientation while As-stablized c(2×8) surface generated more (110) orientation. For Al on InAs(001) surface, Al(111)[1$\bar{1}$0] ‖ InAs(001)[1$\bar{1}$0] [23], [41], [42] and Al (110)[1$\bar{1}$0] ‖ InAs (001)[110] were observed [41], [42]. Research about aluminum deposition on III-V semiconductor surfaces with larger lattice constants such as GaSb(001) [42] and InSb(001) [43] showed the growth orientation of aluminum layer is (110). Some references about Al-semiconductor deposition will be mentioned again in the following sections.

It is noteworthy that in some cases even the lattice structure of the deposited crystal can also change. When copper was deposited on Ag(001) surface, in certain growth conditions the copper thin film showed a body-centered cubic (BCC) structure rather than a natural FCC structure, with an alignment Cu(001)[1$\bar{1}$0]$_{\mathrm{BCC}}$ ‖ Ag(001)[010]$_{\mathrm{FCC}}$ [44]. Note there is no evidence of the existence of BCC copper in nature. This implies that the energy of the BCC copper lattice has much higher energy than the natural FCC lattice. However, the existence of BCC copper lattice in the thin copper film implies that the interaction energy on the epi-

taxial interface overcompensated the energy difference between the BCC and FCC copper lattice. This example also showed the importance of the structural behavior of the epitaxial interface. In the next section, some established understanding of the epitaxial interface is presented.

1.2.2 Analysis of epitaxial interfaces

An essential question about the epitaxial interface is: how should the deposit crystal orient to make the interfacial energy lower? The analysis of this question varies according to the nature of the interfacial bonding. The coincidence lattice model [45] was established to analysis the interfaces with metallic or van der Waals bonding. In the coincidence lattice model, the interfacial lattice of the substrate and the deposited layer is considered as fixed grids. To obtain the lowest energy configuration, the deposit crystal should be arranged in such a way that a maximum number of the lattice points can be brought into coincidence. The model is illustrated in Figure 1.1. In the figure, he crystal with blue atoms is rotated in the plane of the interface to allow a maximum number of coincident red and blue atoms.

The ball-and-stick model [46], [47] on the other hand assumes that the chemical bonds are anisotropic, which can be applied to semiconductor material with directional covalent bonds. Figure 1.2 shows a 3D ball-and-stick model of a GaAs (same for InAs) crystal with no surface reconstructions. One can see the directional dangling bonds on the surface of the crystal. In a heterojunction made up of two pieces of semiconductor crystal with different lattice parameters, the ball-and-stick model is able to describe the misfit dislocations at the interface (shown in Figure 1.3).

The isotropic and anisotropic bonding can be considered as two extreme cases of the atomic bonds near the epitaxial interface. However, in the case of aluminum deposition on III-V semiconductors, the condition lies somewhere in the middle. On one hand, the dangling

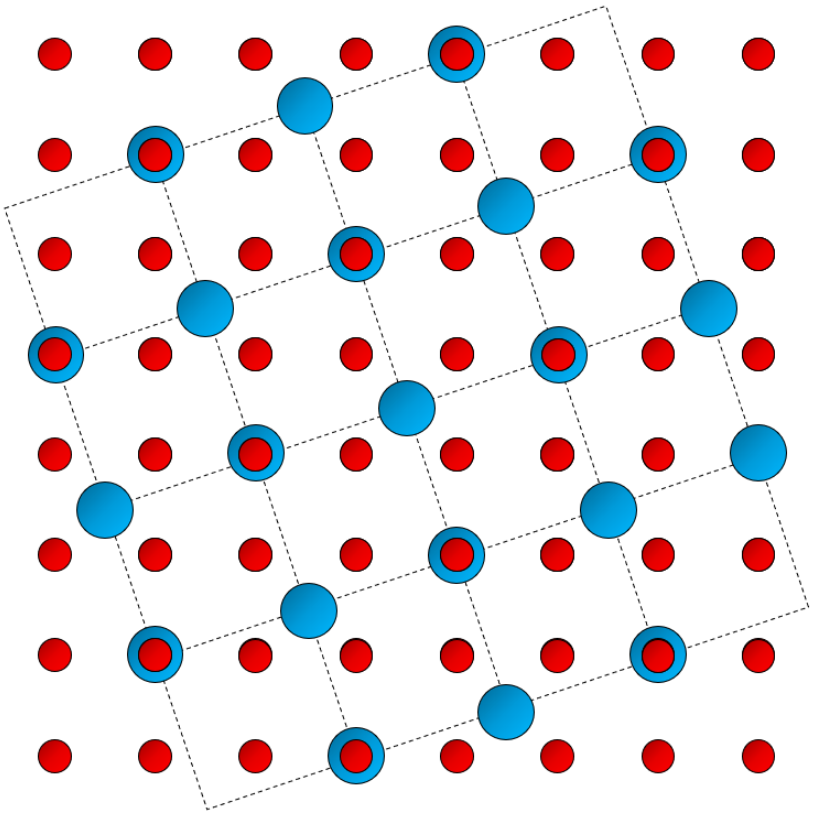

Figure 1.1. A schematic diagram of the coincidence lattice model. The red atomic plane and the blue atomic plane are in contact on each side of the epitaxial interface. The crystal with blue atoms is rotated in the plane of the interface to allow a maximum number of coincident red and blue atoms. The dash lines are used to clearly visualize the lattice of the blue crystal.

bonds on the surface of the semiconductor are directional. On the other hand, aluminum as a metal has metallic bonds between the aluminum atoms, which is isotropic. For isotropic interaction, the interfacial energy is lowered by maximizing the number of the coincident lattice points. However, the configuration that maximizes the number of the coincident lattice points can also increases the energy of the dangling bonds. This is a difficulty when analyzing the Al-semiconductor interface. The following part of this section will discuss how this applies to Al-GaAs and Al-InAs interfaces by discussing some experimental results by previous researchers.

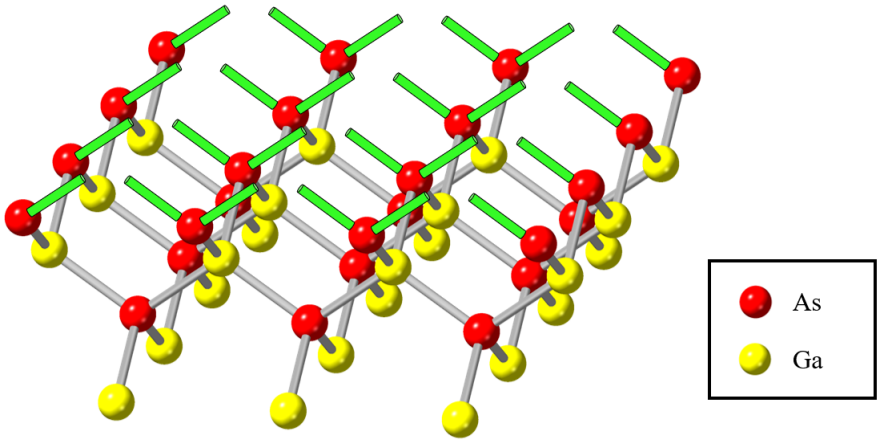

Figure 1.2. A 3D ball-and-stick model of a piece of GaAs crystal with no surface reconstructions. The red and yellow balls present As and Ga atoms, respectively. The grey sticks present the As-Ga covalent bonds. The green sticks present the dangling bonds from the surface arsenic atoms. The model also stands the same for InAs by replacing Ga with In atoms.

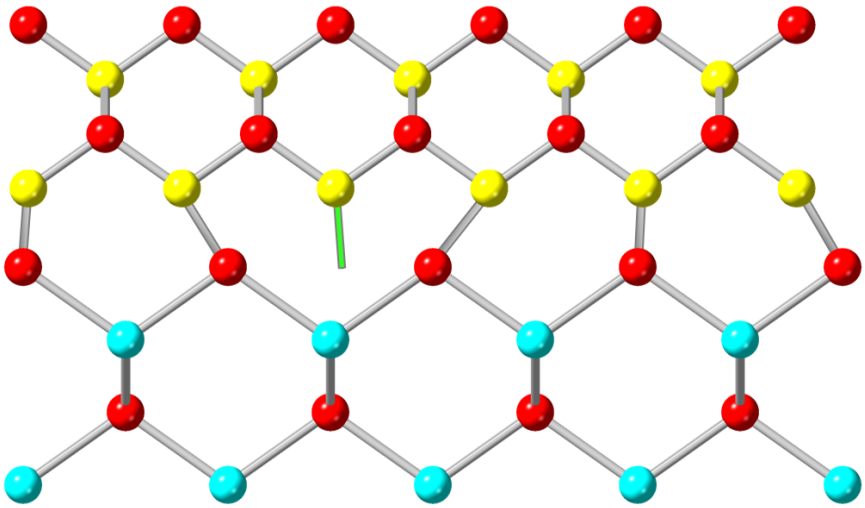

Figure 1.3. A schematic diagram of the ball-and-stick model of the epitaxial interface of two semiconductor layers with different lattice constants in cross-sectional view. The grey sticks present the covalent bonds. The green stick presents the dangling bond at the misfit dislocation.

Aluminum on GaAs(001)

Al/GaAs system has potential application in nanoelectronics and nanophotonics [48]–[50] However, one fact that also drew researchers' attention was that the lattice constant of bulk

GaAs is 5.6532 , which is approximately $\sqrt{2}$ times the lattice constant of bulk aluminum, 4.0495 . In mathematical expression, $a_{\mathrm{Al}\langle 100\rangle} \approx a_{\mathrm{GaAs}\langle 100\rangle}/\sqrt{2} = a_{\mathrm{GaAs}\langle 110\rangle}$. Given this fact, the epitaxial alignment Al(001)[100] ∥ GaAs(001)[1$\bar{1}$0] (which can be obtained by putting aluminum and GaAs in parallel and then rotating the aluminum in the plane of interface by 45°) leads to very small lattice mismatch ($< 1.3\%$) along each $\langle 100\rangle$ direction in the epitaxial interface. This small lattice mismatch configuration is exactly the configuration that maximizes the number of coincident lattice sites. To take the directional dangling bonds on the GaAs surface into consideration, one can subtract the first atomic layer as well as the dangling bonds (the top layer of red atoms and the green sticks in the 3D model of GaAs presented in Figure 1.2) and put the first aluminum layer on top of them. The resulting configuration is shown in Figure 1.4. One can see that half of the aluminum atoms are chemisorbed by the dangling bonds. However, the disconnected dangling bonds can raise the energy of the interface so it is not obvious that this configuration has the lowest energy. It is noteworthy that a similar method was used to analyze the Al-GaAs interface structure in Reference [38].

Experimentally, the "small mismatch" epitaxial orientation Al(001) [100] ∥ GaAs(001)[1$\bar{1}$0] was not the first orientation observed. The first observation was given by Ludeke et al. in 1973 [40]. In their growth experiments, the substrate temperature varied from 50°C to 500°C and the growth rate varied from 0.001 nm/s to 0.1 nm/s. In-situ high-energy electron diffraction (HEED) was used to characterize the deposition. The $c(2 \times 8)$ GaAs surface reconstruction was observed before the aluminum deposition. The epitaxial orientation of Al(110)[$\bar{1}$10] ∥ GaAs(001)[1$\bar{1}$0] was the only alignment that was observed. Ludeke et al. suggested that the 45° rotated orientation, Al(001)[100] ∥ GaAs(001)[1$\bar{1}$0], might not be energetically favorable because of the unmatched aluminum atom on the interface.

A later work by Cho et al. in 1978 was an example of the observation of Al(001)[100] ∥ GaAs(001)[1$\bar{1}$0] [51]. In their work, a deposition rate of 0.06 nm/s was used. The surface reconstruction of the GaAs surface was also $c(2 \times 8)$. The main difference from Ludeke et al.'s work was that the substrate was cooled down to room temperature for aluminum deposition. TEM and XRD experiments were used to characterize the aluminum layer and

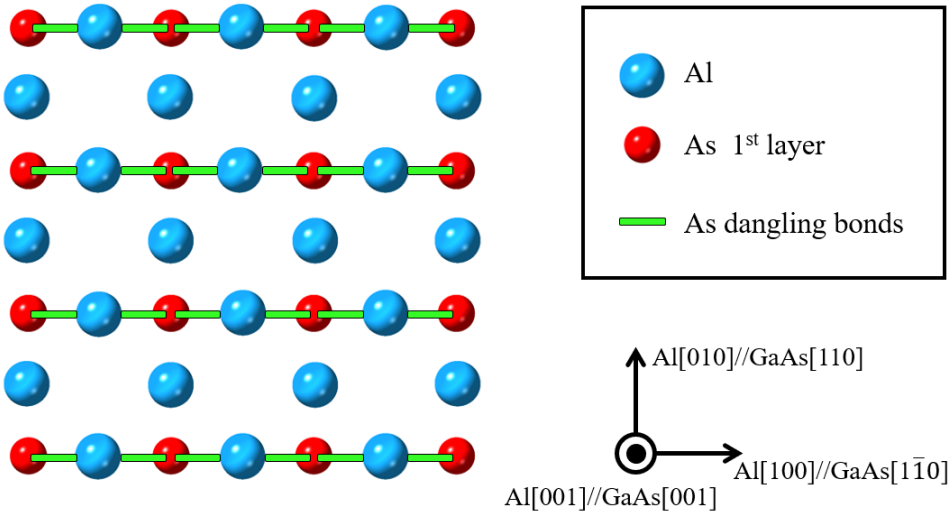

Figure 1.4. The top-down view of the epitaxial interface in alignment Al(001)[100] ‖ GaAs(001)[1$\bar{1}$0]. The blue and red balls present Al and As atoms, respectively. The green sticks present the dangling bonds from the surface arsenic atoms. Because of the small mismatch, a large number of aluminum atoms are connected to the dangling bonds.

all experimental results confirmed the alignment.

In 1981, Petroff et al. reported the observation of both alignments mentioned above [36]. The aluminum deposition was done at a substrate temperature less than 80°C. Arsenic-rich $c(2 \times 8)$ surface was the surface reconstruction on which aluminum was deposited. The growth rate was the varied parameter. In their result, it was shown that the low growth rate (< 0.013 nm/s) led to Al(110)[$\bar{1}$10] ‖ GaAs(001)[1$\bar{1}$0] alignment, while the high growth rate (> 0.033 nm/s) led to Al(001)[100] ‖ GaAs(001)[1$\bar{1}$0] alignment. Petroff et al. analyzed the reason for the different alignments. They concluded that the atomic steps were the reason of the formation of the Al(110) orientation since the height of the GaAs(001) surface steps matched the height of the Al(110) layer. A possible atomic configuration is shown in Figure 1.5 (readers can find the original figure in Reference [36]). It was noteworthy that the deposition was also performed on Ga-rich (4×6) surface which does not contain a large density of surface steps. All deposition on this type of surface showed (001) oriented aluminum film. So

Petroff et al. claimed that it was evidence that (110) deposition was favored by surface steps.

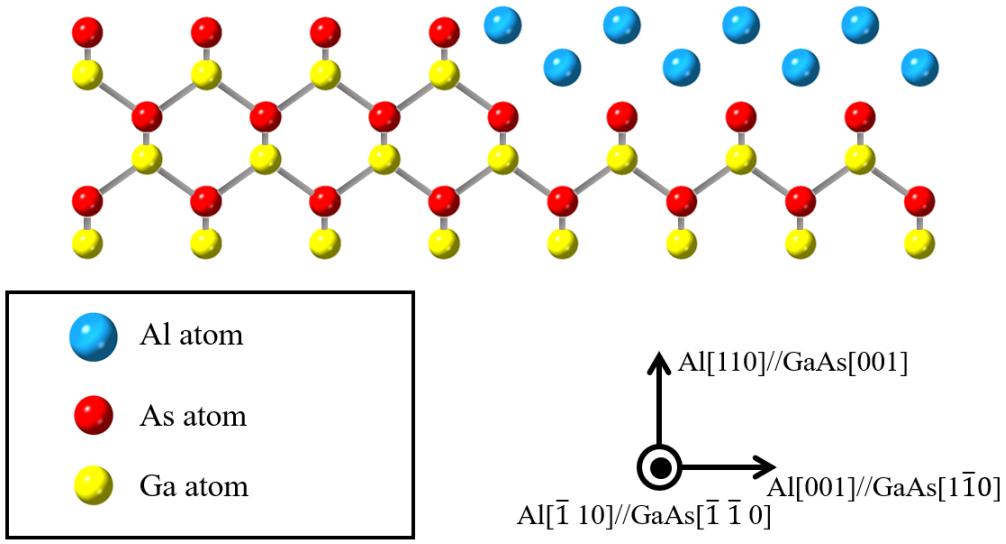

Figure 1.5. A schematic diagram in a cross-sectional view to show the possible atomic configuration of the aluminum layer formed near a surface step of GaAs. The epitaxial orientation of Al(001)[100] ∥ GaAs(001)[1$\bar{1}$0] is formed in this configuration.

Comparing all work mentioned above, one can conclude that high substrate temperature and/or low deposition rate causes (110) oriented aluminum growth, while low substrate temperature and/or high deposition rate causes (001) oriented aluminum growth. This was also supported by a much later work by Lin et al. in 2013 [39]. In this work, aluminum was deposited on GaAs(001) surface at a temperature of 0°C with a growth rate of 0.05 nm/s. The XRD characterization suggested that the resulted aluminum film was (001) oriented. The substrate temperature and the growth rate effect the surface diffusion of adatoms. High substrate temperature and/or low growth rate makes adatoms more mobile on the surface. Therefore, a hypothesis can be made. The (110) aluminum is formed because the adatoms are mobile enough to reach the surface steps and the aluminum film starts to form from there. The nucleation on the surface steps are more energetically favored to be (110) oriented because of the low mismatch of the layer heights. Low substrate temperature and/or

high growth rate makes adatoms less mobile. Instead of travelling to a surface step to form nucleation, the adatoms see more "local" surface where they landed. In this case a nucleation with (001) orientation is more energetically favorable.

Information about step densities on the GaAs surface upon which aluminum was deposited was not provided by Petroff et al. to permit comparisons of adatom diffusion lengths. However, the argument that (110) oriented aluminum grains were associated with surface steps was also discussed in a later work by Kiely et al [38]. In Reference [38], aluminum deposited on the GaAs surface that was initially cleaned in-situ by Ar+ beams showed more continuity. They claimed it was because the cleaned surface was heavily stepped so there were more nucleation centers for the island growth and hence coalescence of islands to form a continuous film occurred much sooner.

The above discussion showed the complicity of the formation of different epitaxial alignments between Al and GaAs. The epitaxial alignment is not determined by the lattice mismatch or the number of coincident lattice sites alone. In each case, the energetically favored aluminum nucleation can be different and consequently the aluminum film with different epitaxial orientation can be formed.

It is also noteworthy that almost all aluminum depositions mentioned in this thesis were done at substrate temperatures much lower than 0°C with a growth rate of about 0.07 nm/s.

Aluminum on InAs(001)

Aluminum deposition on InAs has a much shorter history compared to aluminum on GaAs. It has been mentioned in Section 1.1 that P. Krogstrup et al.'s work in 2015 studied the growth of Al-InAs nanowire system and provided a solution to the soft gap problem [19], [20]. It is suggested in Reference [19] that the formation of the uniform aluminum epitaxial orientation is a critical factor in the good morphology of the aluminum film and low disorder of the entire material system. Like the factor $\sqrt{2}$ relationship between aluminum and GaAs, there is a similar relationship between aluminum and InAs, which is $3a_{\mathrm{Al}\langle 100\rangle} \approx 2a_{\mathrm{InAs}\langle 100\rangle}$. Therefore, the parallel epitaxial alignment of Al(001)[110] ∥ InAs(001)[110] makes three alu-

minum interfacial units coincide with two InAs interfacial units and makes a very small mismatch ($< 0.3\%$) in both $\langle 110 \rangle$ directions on the interface. This is also known as "domain matching" [52], where a 2×2 domain of the InAs and a 3×3 domain of the Al match perfectly. Note this is also the configuration that maximizes the number of coincident lattice sites. The configuration can be visualized by lying the first layer of aluminum atoms on the top layer of As atoms and their dangling bonds (one can also refer to Figure 1.2 for InAs). Figure 1.6 shows the configuration. Although the number of coincident lattice sites is maximized, there are actually very few aluminum atoms connected to the dangling bonds of the As atoms, thus this epitaxial alignment is not considered energetically favored.

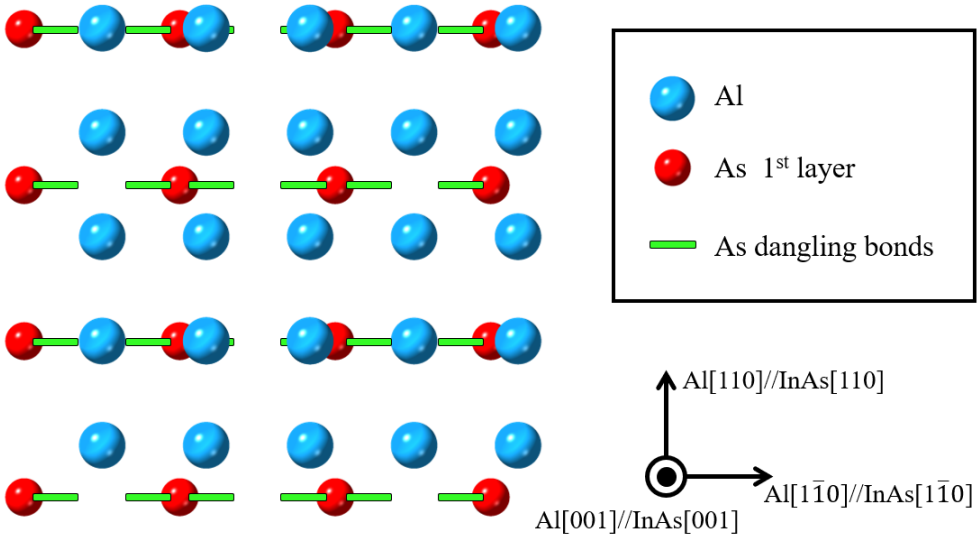

Figure 1.6. The top-down view of the Al-InAs interface with epitaxial orientation Al(001)[1$\bar{1}$0] ∥ InAs(001)[1$\bar{1}$0]. The blue and red balls present Al and As atoms on each side of the epitaxial interface, respectively. The green sticks present the dangling bonds from the surface arsenic atoms.

In an aluminum deposition experiment in Reference [19], two types of films were observed when deposition was performed on a $(1\bar{1}00)_{\mathrm{WZ}}$ facet of an InAs nanowire along $[0001]_{\mathrm{WZ}}$ direction. Here the subscription "WZ" stands for wurtzite, which idenifies the lattice structure of the InAs nanowire. If the aluminum film was thin (< 20 nm), the aluminum was grown along (111) orientation with crystal alignment Al(111)[11$\bar{2}$] ∥ InAs(1$\bar{1}$00)[0001]. Thicker

aluminum growth would lead to $(11\bar{2})$ growth orientation with alignment Al$(11\bar{2})[111]$ ‖ InAs$(1\bar{1}00)[0001]$. In addition, when aluminum was deposited on a zinc blende (111) facet of an InAs nanowire, only (111) growth orientation of aluminum was observed (parallel orientation).

Note among these three types of aluminum deposition, both Al$(11\bar{2})[111]$ ‖ InAs$(1\bar{1}00)[0001]$ and Al$(111)[11\bar{2}]$ ‖ InAs$(111)[11\bar{2}]$ have very low "domain mismatch" on the interface ($<$ 0.3%) because of the 2/3 ratio of the lattice constants. On the other hand, Al$(111)[11\bar{2}]$ ‖ InAs$(1\bar{1}00)[0001]$ does not hold the same property. It was mentioned in Reference [19] that in the direction along Al$[11\bar{2}]$ and InAs[0001], a 7/5 domain matching was needed to get a mismatch of 0.5% but there will be a significant amount of unmatched aluminum atoms. However, the aluminum film with Al$(111)[11\bar{2}]$ ‖ InAs$(1\bar{1}00)[0001]$ showed better morphology comparing to the one with $(11\bar{2})$ orientation.

Aluminum with (111) growth orientation was not only observed in nanowire systems. Research by Shabani et al. in 2016 performed aluminum deposition on a two-dimensional InAs heterostructure that revealed aluminum layers with a (111) growth orientation [23]. (In their work, the surface that aluminum was deposited onto was $In_{0.8}Ga_{0.2}As$ which was the top barrier of an InAs quantum well, but it is still considered in the section of Al on InAs since the surface is closer to InAs in both lattice constant and atomic species.) Their epitaxial alignment can be presented as Al$(111)[1\bar{1}0]$ ‖ InAs$(001)[1\bar{1}0]$. A model of this alignment is presented in Figure 1.7. Instead of drawing all As dangling bonds, only aluminum atoms that are close to being connected to dangling bonds are marked out by green triangles (Here the term "close to being connected" is defined such that the bond has to be elongated less than 10% to connect to an Al atom.). There are in total 12 out of 24 As dangling bonds connected to aluminum atoms comparing to 8 out of 24 in Figure 1.6. From a lattice mismatch perspective, the direction along Al$[1\bar{1}0]$ and InAs$[1\bar{1}0]$ has low mismatch because of the formation of the 2/3 proportion, while in the direction along Al$[11\bar{2}]$ and InAs[110] the lattice mismatch is as high as 18%.

Given the high mismatch, the observation of (111) growth orientation implied Al orientation is controlled by a variable other than lattice mismatch. Both Krogstrup et al. and Shabani et al. suggested that grain growth progression after a complete aluminum layer has

formed was important in controlling epitaxial alignment, and the low surface energy of the (111) aluminum layer was the driving force of the formation of that alignment [19], [23]. The grain growth stage, which happens after separated aluminum islands meet and form a complete film, includes a process where higher energy grains are consumed by lower energy grains. The surface energy was claimed to have the largest contribution to the total energy of the grains when they were thin (This was expressed in equation (9) in Supplementary Information in Reference [19]). Since the surface energy density of (111) is the lowest among all aluminum surfaces [53], the grains with (111) growth orientation expand by consuming other grains and finally unified the epitaxial alignment of the entire aluminum film.

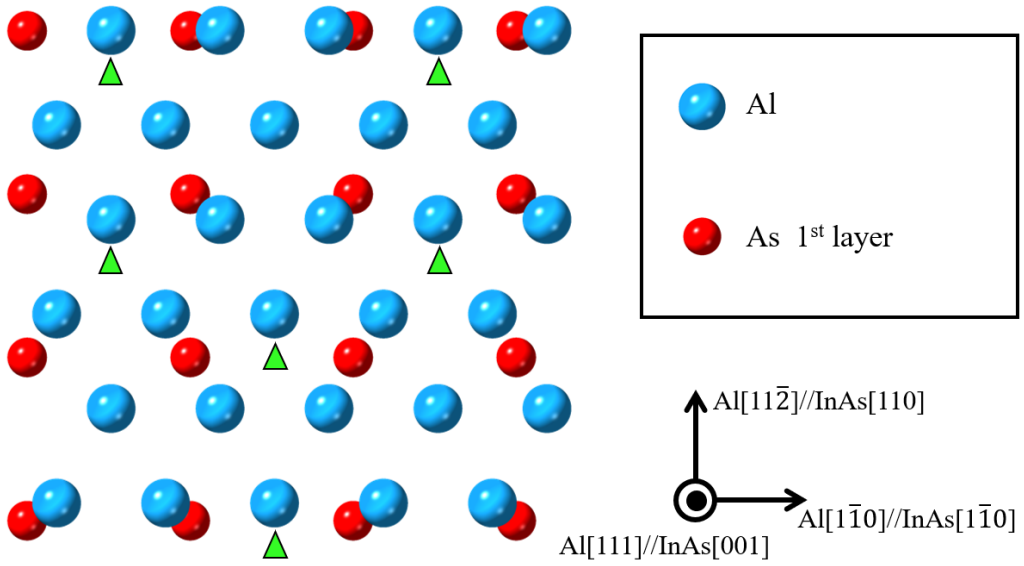

Figure 1.7. A top-down view of the Al-InAs interface with epitaxial orientation Al(111)[1$\bar{1}$0] ∥ InAs(001)[1$\bar{1}$0]. The blue and red balls represent the aluminum and arsenic atoms on each side of the epitaxial interface. The green triangle marked the aluminum atoms that are close enough to be connected by the As dangling bonds.

Although the discussion above can explain the formation of (111) aluminum film in both one-dimensional and two-dimensional cases, there are still major deficiencies in the discussion. First and foremost, the discussion ignored the effect of the energy of the epitaxial

interface. Secondly, the epitaxial alignment of the separated aluminum islands was not discussed. They were assumed to have a random distribution of orientations. However, it was a doubtful statement. The difference in the total energy of the islands was able to affect their chemical potential and thus the island growth stage should have energetic preferences. Therefore, it was hard to specify that the grain growth stage was the major stage to decide the formation of (111) films. In other words, if all the aluminum islands were already (111) islands before the complete film formed, a grain growth stage would not be necessary. Lastly, direct evidence of grain growth was not observed in the aluminum films with (111) growth orientation. There are technical difficulties to monitor the growth process in real-time, but a grain growth stage that contains a massive transformation of grains is doubtful to be perfect and make no defects in the final aluminum film.

The deficiencies in the grain growth explanation of the growth orientation formation, especially the neglect of the interfacial energy, actually predicted no possibilities of forming thin aluminum films with growth orientation other than (111). However, later works by Sarney et al. observed aluminum films with (110) growth orientation [41], [42]. The epitaxial alignment was Al(110)[001] $\parallel$ InAs(001)[1$\bar{1}$0]. This alignment was also observed in other works on aluminum deposition on semiconductors like GaSb and InSb [42], [43]. It was clear that surface energy was not the only driving force in the formation of the aluminum films with this epitaxial alignment. Figure 1.8 depicts the coincidence lattice model of the epitaxial alignment. The green triangles are also used to mark the aluminum atoms that are close to being connected to dangling bonds. There are 12 out of 24 As dangling bonds connected to aluminum atoms, which is the same amount in the model in Figure 1.7. The atomic density of the (110) aluminum layer ($\sqrt{2}/a^2$) is less than a (111) aluminum layer ($4/\sqrt{3}a^2$), which on the other hand makes the total number of unmatched aluminum atoms smaller and could lead to lower interfacial energy. However, this is a qualitative analysis of the interfacial energy. Better analysis requires imaging of the real structure of the epitaxial interface. This is where characterization tools like transmission electron microscopy (TEM) are applied in this thesis.

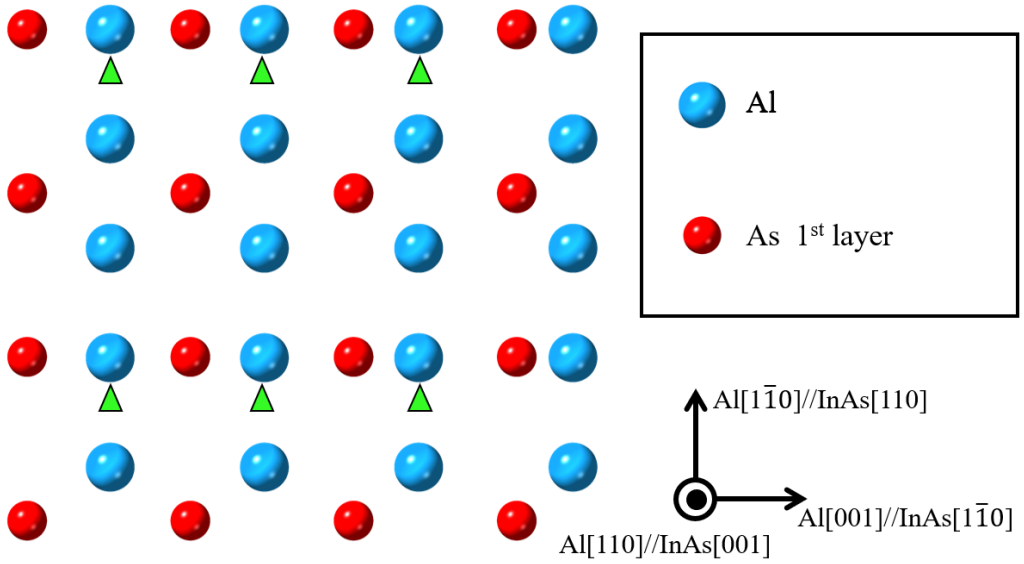

Figure 1.8. A lattice coincidence model of epitaxial alignment Al(110)[001] || InAs(001)[1$\bar{1}$0]. The blue and red balls represent the aluminum and arsenic atoms on each side of the epitaxial interface. The green triangle marked the aluminum atoms that are close to being connected by the As dangling bonds.

1.2.3 Growth modes of thin-film deposition

One other main difference between homoepitaxial and heteroepitaxial growth is that in the heteroepitaxial growth, the chemical potential of the deposited crystal depends on its thickness. The dependence is because of the difference in bonding with the substrate [54].

Consider a small 2-dimensional island of the deposited crystal that only contains the first monolayer. Removing an atom from this island requires work to break both the lateral bonds with the surrounding atoms in the deposited crystal and the vertical bonds with the underlying substrate. On the contrary, removing an atom from the surface of an infinitely large piece of the deposited crystal requires work to break identical bonds within the deposited crystal. If the work required to break the bond to the substrate is greater than the work to break a bond within the deposited crystal, the chemical potential of this small 2D island on the substrate is lower than the chemical potential of an infinite large deposited crystal. Now consider the chemical potential of the second monolayer of the deposited crystal. Since the substrate has a lower effect on it than on the first monolayer, the second monolayer has

a chemical potential closer to an infinite large crystal. Since strain energy is built up with thickness, however, the chemical potential can also vary from monolayer to monolayer due to the strain energy [55], [56]. Adding the contribution together and plotting the chemical potential as a function of the layer number normally leads to three types of dependence, shown in Figure 1.9 [54]. The three types of dependence correspond to one of three growth modes: (i) Frank-van der Merwe mode or layer-by-layer mode (Figure 1.10(a)), (ii) Volmer-Weber mode or island growth mode (Figure 1.10(b)) and (iii) Stranski-Krastanov mode or layer-by-layer followed by 3D island mode (Figure 1.10(c)).

The first definition of the three growth modes was given by Bauer in 1958 according to the difference in surface energies [57], which is equivalent with the classification given here in terms of the chemical potential difference [54].

Volmer-Weber (V-W) mode takes place when the relationship between the chemical potential and layer number $\mu(n)$ satisfies $\frac{d\mu}{dn} < 0$. This happens when the bond between the deposited atoms is stronger than the bond between the deposited atom and the substrate atoms. Since $\mu(1) > \mu(2), \mu(2) > \mu(3), ...$, the formation of the second layer takes place before the completion of the first one, and then the formation of the third layer takes place before the completion of the second one, ... This leads to the formation of 3D islands.

Frank-van der Merwe (F-M) mode takes place in the opposite condition $\frac{d\mu}{dn} > 0$. This happens when the bond between the deposited atom and the substrate atoms is stronger and the mismatch between the two crystals is small. In this case, $\mu(1) < \mu(2), \mu(2) < \mu(3), ...$, hence each layer completes before the next layer starts to form.

Stranski-Krastanov (S-K) mode describes the case in which $\frac{d\mu}{dn} > 0$ is satisfied at the beginning but the sign changes its direction after several monolayers. This happens when the bond between the deposited atom and the substrate atoms is stronger but there is a large mismatch. The film is grown in layer-by-layer mode at first but 3D islands start to form after several layers.

To gain a better understanding of the growth mechanism, it is important to analyze which growth mode the deposition takes under different growth conditions. It is noteworthy

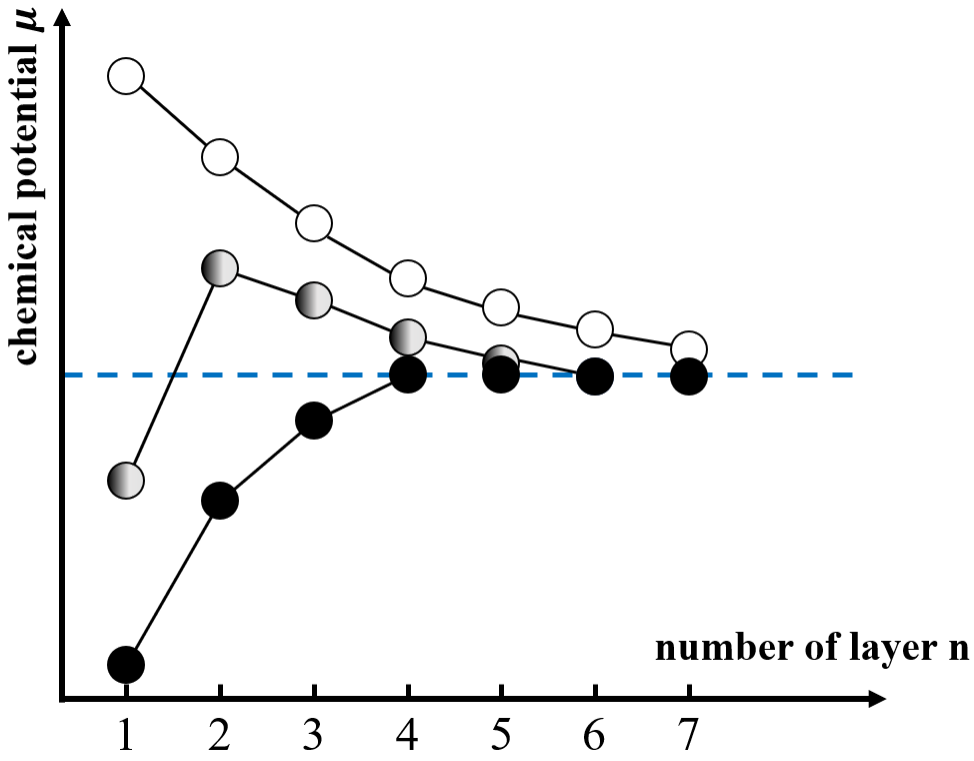

Figure 1.9. A schematic presentation of the chemical potential as a function of the layer number. Unfilled circles present the chemical potential decreases when the number of the layer goes up, which leads to Volmer-Weber growth mode. Solid black circles present the chemical potential increases when the number of the layer goes up, which leads to Frank-van der Merwe growth mode. Shadow grey circles present the chemical potential increases and then decreases when the number of the layer goes up, which leads to Stranski-Krastanov growth mode. The dashed line presents the chemical potential of an infinite large deposited crystal.

that the three growth mode that was predicted by the difference of the chemical potential of each layer determines the equilibrium morphology of the deposited crystal. However, in real growth, the process is usually far from equilibrium, in which growth conditions, such as substrate temperature and growth rate, affect the kinetics of the growth. A large amount of investigation was done on material systems with different nature of interfacial bonding, including deposition of metals on metals [58]–[61], deposition of metals on semiconductors [30]–[32], [62]–[65] and deposition of semiconductors on semiconductors [66]–[70]. Reference [54] reviewed the experimental results and summarized the main tendencies in how growth

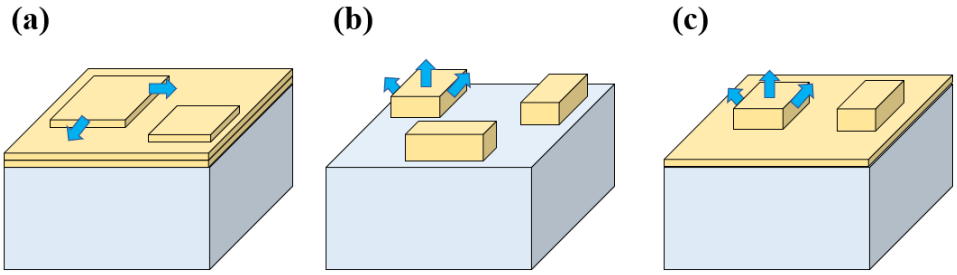

Figure 1.10. The three growth modes when deposited crystal (yellow) is grown on the substrate (blue). (a) Frank-van der Merwe mode or layer-by-layer mode and (b) Volmer-Weber mode or island growth mode and (c) Stranski-Krastanov mode or layer-by-layer followed by 3D island mode.

conditions determined the growth modes as follows:

1. When the bonding in the deposited crystal is stronger than the bonding between the deposited atoms and the substrate, the formation and the growth of isolated 3D islands are more favored than the formation of monolayers.

2. When the deposition is done at a high substrate temperature, the growth of 3D islands (V-W or S-K mode) is more favored. The relative height of the 3D islands increases when the temperature increases.

3. Layer-like growth is more favored when the deposition rate is high. The growth looks more 2D when the deposition rate goes higher.

4. The lattice mismatch is also important. The larger the mismach, the greater is the tendency towards 3D island-like growth.

In the context of aluminum deposition, the discussion can be pictured in Figure 1.11. To compare the chemical potential of the first and second monolayer of the deposit aluminum crystal, one should compare the work done in removing one aluminum atom from the side of the first monolayer and the work done in removing one aluminum atom from the side of the second monolayer [54].

Each work includes the energy cost of breaking the side bonds and the vertical bonds.

Given the same crystal orientation of the two monolayers, the side bonds should be the same. However, the vertical bonds are not the same. For layer 1, the aluminum atom is bonded by the dangling bonds of the arsenic atoms, while for layer 2, the aluminum atom is bonded by metallic bonding with the underlying aluminum atoms. The comparison is now reduced to the comparison of the Al-As bonding and the Al-Al bonding.

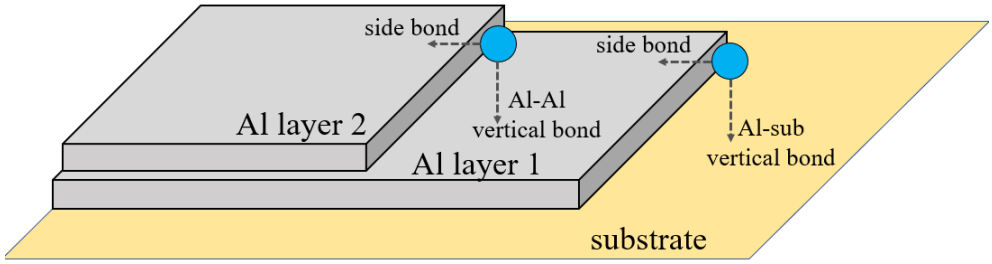

Figure 1.11. To compare the chemical potential of the aluminum monolayers, the work done in removing one aluminum atom from the side of each monolayer should be considered. The work and be divided into two parts, the energy cost to break the side bonds (with aluminum) and the energy cost to break the vertical bonds (with substrate for the first monolayer and with aluminum for the second monolayer.)

Some clarification should be made in the discussion above. The discussion dismissed the strain effect. For the second monolayer of aluminum, the discussion also dismissed the interaction from the substrate so the chemical potential of the second (and above) monolayer is equal to the bulk value.

Moreover, the Al-Al metallic bonding is not bonds between single aluminum atoms. However, to get a qualitative understanding, one can use the nearest neighbor approximation to describe the Al-Al bonding, in which each aluminum atom is considered making one bond with each nearest aluminum atom (12 in total). Given this approximation, the bond dissociation energy of Al-Al can be obtained by considering the sublimation of solid aluminum. The sublimation energy of 1 mole of aluminum is equal to the energy required to break every Al-Al bond in the 1 mole of aluminum. One aluminum atom makes bonds with its 12 nearest

aluminum atoms. Also, keep in mind that one Al-Al bond is shared by two atoms. Thus, the sublimation energy of 1 mole of aluminum is equal to $12/2 = 6$ times the dissociation energy of 1 mole Al-Al bonds. The sublimation energy of aluminum is 330 kJ·mol^{-1} [25]. As a result, the dissociation energy of the Al-Al bond is 55 kJ·mol^{-1}.

Obtaining the bond dissociation energy of Al-As bonds is not straight forward. Based on the bond structure of AlAs crystal, the energy required to turn 1 mole of solid AlAs into atomic aluminum and atomic arsenic is equal to 4 times the bond dissociation energy of 1 mole of Al-As bonds. It can be written as:

$$E_{\text{Al-As}} = \frac{1}{4}(H_{\text{Al(g)}} + H_{\text{As(g)}} - H_{\text{AlAs(s)}}). \tag{1.1}$$

Given the sublimation energy $\Delta H_{\text{sub}} = H_{\text{g}} - H_{\text{s}}$, the equation 1.1 can be written as:

$$E_{\text{Al-As}} = \frac{1}{4}(\Delta H_{\text{sub,Al}} + \Delta H_{\text{sub,As}} + H_{\text{Al(s)}} + H_{\text{As(s)}} - H_{\text{AlAs(s)}}). \tag{1.2}$$

On the other hand, the standard formation enthalpy of solid AlAs can be written as:

$$\Delta H_{\text{AlAs}} = H_{\text{AlAs(s)}} - H_{\text{Al(s)}} - H_{\text{As(s)}}. \tag{1.3}$$

As a result,

$$E_{\text{Al-As}} = \frac{1}{4}(\Delta H_{\text{sub,Al}} + \Delta H_{\text{sub,As}} - \Delta H_{\text{AlAs}}). \tag{1.4}$$

Given $\Delta H_{\text{sub,Al}}$ = 330 kJ·mol^{-1}, $\Delta H_{\text{sub,As}}$ = 302 kJ·mol^{-1} [25], and ΔH_{AlAs} = -62 kJ·mol^{-1} [71], the bond dissociation energy of Al-As can be calculated as 173.5 kJ·mol^{-1}. Note the ΔH values above are valid at 25 ^{o}C. The calculation did not consider the enthalpy change at different temperatures. However, since the deposition temperature in this thesis is -80 ^{o}C to -40^{o}C, the values at 25^{o}C are reasonable approximations.

One can see the bond dissociation energy of Al-As is much larger than the bond dissociation energy of Al-Al. However, it is not yet enough to conclude that Al-substrate interaction is stronger since the numbers above present only the energy of a single bond. One also needs to consider the number of bonds that are dissociated. This is where epitaxial orientation

and the interface configuration come again into the discussion. In nearest neighbor approximation, the number of Al-Al bonds contained in the vertical Al-Al bonding varies according to the crystal orientation. For instance, the vertical bonding contains 3 Al-Al bonds for (111) orientation and contains 5 Al-Al bonding for (110) orientation (shown in Figure 1.12). Also, only a fraction of the aluminum atoms are connected to the dangling bonds in the semiconductor (see Figure 1.7 and Figure 1.8). The interaction between the substrate and an aluminum atom that is connected by the dangling bonds is much stronger than the interaction between the substrate and an aluminum atom that is not chemisorbed into a covalent bond. Therefore, from a statistical perspective, the "effective" interaction energy of Al-As is much smaller than the calculated value and also depends on the interface configuration. The experimental result in Section 3.3 shows that there are differences between the growth modes of the Al(111) layer and Al(110) layer, which is an example of this effect. Additionally, other conditions such as the lattice mismatch, substrate temperature, and growth rate also make contributions to the actual growth mode of the aluminum film.

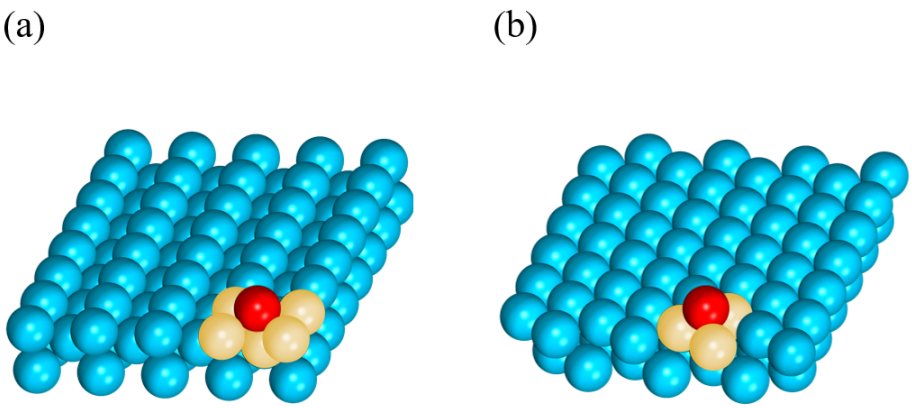

Figure 1.12. The number of Al-Al bonds contained in the vertical bonding when an aluminum atom (red) sits on an aluminum surface (blue) with (110) orientation (a) and (111) orientation (b). The atoms lighted up by yellow color represents the nearest neighbor of the red atom. For (110) there are 5 and for (111) there are 3.

1.2.4 A summary of this section

This section started from the discussion about two major characteristics that distinguished heteroepitaxy from homoepitaxy: the epitaxial alignment and different growth modes. Established understanding and experimental results in the research field of heteroepitaxy that are not solely focused on aluminum deposition on semiconductors are reviewed. More detailed discussion was also given to Al-GaAs(001) and Al-InAs(001) material systems. One main challenge in the discussion was to determine the mechanism of formation of different epitaxial alignments. This is also a major topic that will be discussed in this thesis.

Based on the information reviewed in this section, a complete understanding of the Al deposition process should contain the following information:

1. At the beginning of growth, the energetically favored configuration of the nucleus should be analyzed based on the atomic registry and bonding process with the surface atoms. However, it is a very hard task because the calculation of the energy of a nucleus requires consideration of the interaction between the aluminum atoms and surface atoms, and the interaction between each aluminum atom in the nucleation site, which is a many-body problem. The real semiconductor surface that aluminum is deposited on is always reconstructed. Surface structures like dimers can affect the interaction with the aluminum atoms. Simple models can be discussed to understand specific experimental results. But a general discussion will contain a lot of simulation work, which is beyond the scope of this thesis.

2. During the growth of separated aluminum islands, the energy of different islands should be compared since it reveals the energetic preference of the island formation, which can lead to the explanation of epitaxial alignment formation. Instead of calculating interaction energy between atoms, one can compare the surface energy (which includes the top surface and the side surfaces of an island), interfacial energy on the Al/semiconductor epitaxial interface, and strain energy. In the mathematical expression, the total energy of an

aluminum island writes

$$E = E_{\text{top surface}} + E_{\text{side surface}} + E_{\text{interface}} + E_{\text{strain}}. \tag{1.5}$$

In this expression, the interfacial term and strain term can be analyzed more precisely if one can observe the structural characteristics of the aluminum layer. A good example will be given in Section 3.2 and 3.3. The surface orientation, interfacial atom arrangement, and the residual strain in the aluminum layer were revealed by TEM and XRD experiments, which helped to track back the energetic properties in the growth of islands.

The growth mode in which the islands grow also needs to be analyzed to see the process of film formation. Although the growth is not able to be monitored in real-time, structural characterization (grain boundaries et al.) will show the marks of the growth process and help the analysis.

3. The analysis of the grain growth stage needs to provide evidence of crystal reconstruction during the growth (if there is any). Defects such as twinning defects and small misoriented grains in the aluminum layer should be searched. Relative rotation between surface domains will also be analyzed. As will be shown in Chapter 3, it was found that the Al(111) films contained smaller grains and there were rotations between grains, which could be produced by grain growth. On the other hand, the (110) oriented aluminum films we grew remained single crystal in a relatively large area, which showed a low possibility that the layer went through massive crystal transformation.

2. EXPERIMENTAL METHODS

2.1 Aluminum Layer Growth

2.1.1 Introduction to molecular beam epitaxy (MBE)

Molecular beam epitaxy (MBE) is a non-equilibrium crystal growth technique. The technique was developed in the late 1960s at Bell Telephone Laboratories by J. R. Arthur and A. Y. Cho [35], [72]–[74]. Today, MBE is widely used for semiconductor growth with near-perfect surface morphology, near-perfect control of thickness, as well as layer chemical compositions and doping levels for the fabrication of advanced semiconductor devices [75], thus, this technique is considered as a fundamental tool in nanotechnology.

MBE takes place in high vacuum (HV) or ultra-high vacuum (UHV) ($10^{-8} - 10^{-12}$ Torr) environment. Working in such a high vacuum environment is one fundamental advantage of the technique. Because of the very low pressure in the MBE chamber, the atoms can travel with a very long mean-free-path, which implies that the atoms can reach the growth wafer directly without reacting with each other.

Another advantage of the MBE technique is the low and controllable deposition rate. In this work, the deposition rate is typically 0.5-1.0 monolayer per second (ML/s) for semiconductor growth and 0.07 nm/s (about 0.25 ML/s) for aluminum. Comparing to other deposition techniques like sputtering, a low deposition rate allows the atoms to land onto the growth surface with a low concentration, which gives each atom more time to find its own lowest energy state (similar discussion in Section 1.2.3). The low deposition rate needs a proportionally better vacuum to keep the same impurity level. This requirement is again satisfied by the UHV environment.

In this section, the MBE system used for our sample growth will be presented, and the growth process for the aluminum superconducting layer will be described.

2.1.2 MBE System setup for sample growth

We build up an MBE system that contains two reactor chambers for sample growth. The two chambers are connected with UHV buffer chambers that are used to transfer the sample between the two chambers. Figure 2.1 shows a picture of the system. Figure 2.1(a) was taken from the chamber side, which showed the main MBE chamber and the metallization chamber. Figure 2.1(b) was taken from the side of the transfer tube, which was distinguished by a long straight tube and several magnetic controlled transfer arms. The two MBE chambers will be discussed next.

Figure 2.2 shows a layout of the first (main) MBE chamber. This chamber is used for the growth of the semiconductor heterostructure and also has the ability to cool the substrate for deposition of the aluminum superconducting layer. Some components in this chamber are discussed below.

Effusion cells

Gallium, aluminum, indium, arsenic and antimony are used for the semiconductor heterostructure growth. Aluminum is also used for superconducting layer deposition. The source material is loaded into separate Knudsen effusion cells [76] and heated up to the temperatures in which slow evaporation occurs. The gas phase material then condenses and reacts on the growth wafer. In this process, the growth rates are controlled by the temperatures of the different cells. A shutter is assembled in front of each cell and the manipulation of the shutters controlled the growth of the heterostructures as well as the aluminum superconducting layer. For instance, the shutters of indium, gallium and arsenic cells are opened to grow an InGaAs layer. To finish the InGaAs layer and start growing InAlAs layer, one has to keep indium and arsenic shutter opened, shut the gallium shutter and open the aluminum shutter simultaneously.

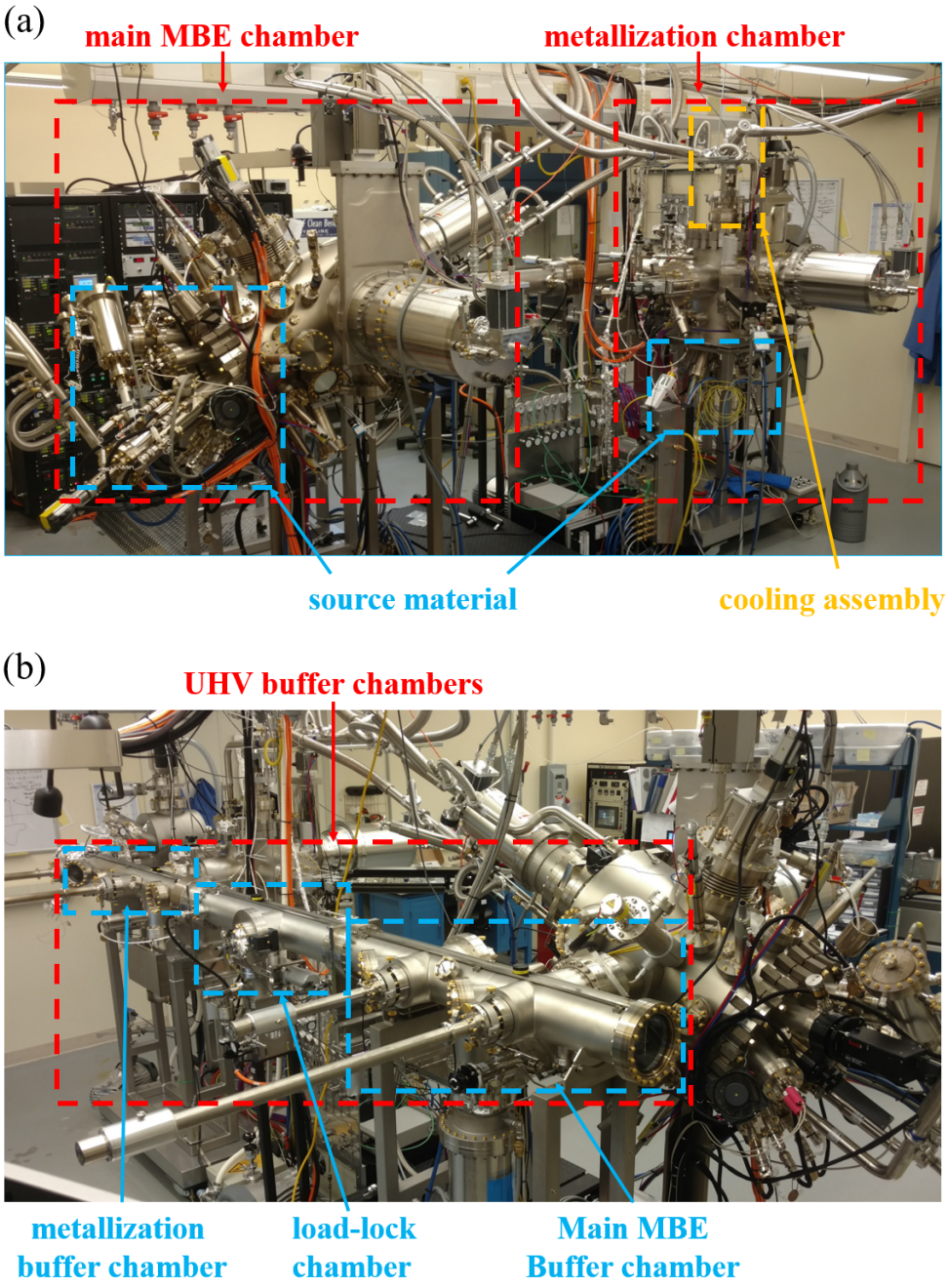

Figure 2.1. Pictures of the MBE system. Picture (a) and (b) are taken on different sides of the system. (a) emphasizes the two MBE chambers, the main MBE chamber on the left and the metallization chamber on the right. Picture (b) emphasizes the UHV buffer chambers that can be used to transfer samples between the two MBE chambers.

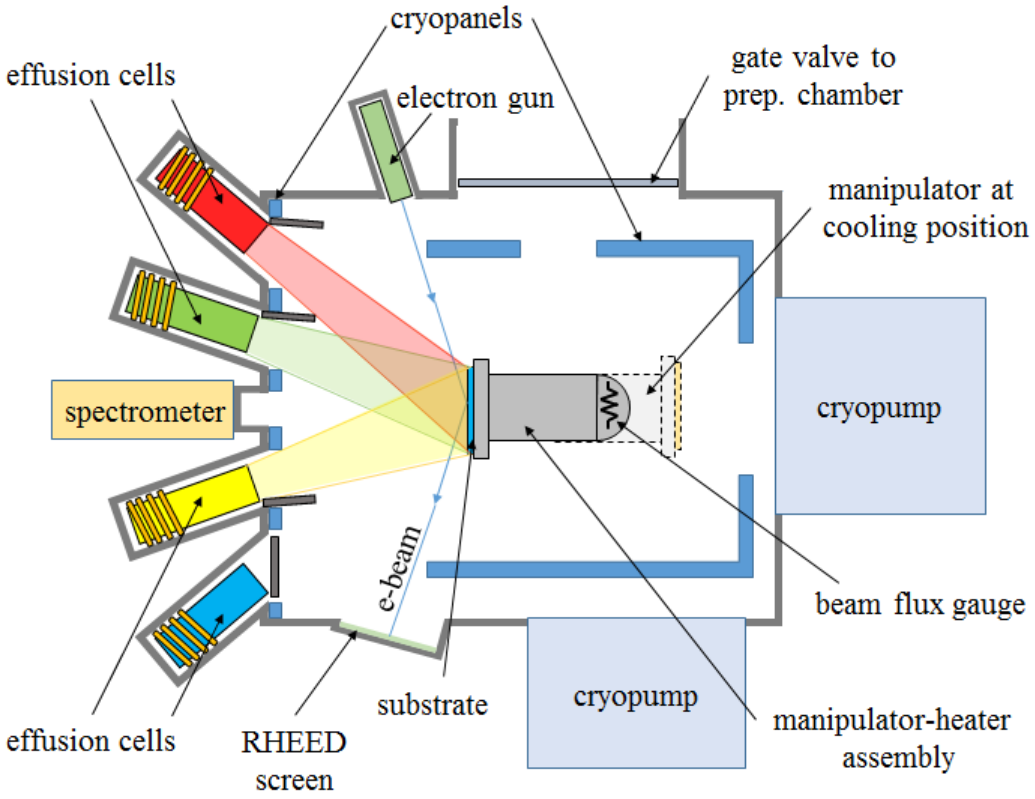

Figure 2.2. A diagram of the main MBE chamber. Important components of the system are marked in the diagram. This diagram mainly shows the status of the system during a growth, where the shutters of the red, green and yellow cell are opened to form a layer that contains the three material. The manipulator assembly drawn by dash lines also shows the cooling process, in which the substrate is facing to the cryopump and heat is absorbed through radiation.

Manipulator-heater assembly

The assembly contains the rotation mechanism, the substrate heater and the beam flux gauge. The rotation mechanism can be used to keep in-plane rotation of the substrate for uniformity of the growth. It can also rotate the whole assembly between the growth position (with substrate facing the cells) and beam flux measurement position (with substrate facing the cryopump).

The heater is made up of electric filaments that can heat up the substrate by radiation. It has the ability to heat the substrate up to about 850°C. The assembly contains a thermocouple close to but not in contact with the substrate. To have a more accurate measurement

of the substrate temperature, a k-Space BandiT system is attached to the chamber. The k-Space BandiT system provides measurements and analysis of the thermal radiation and reflection spectrum of the substrate so the accurate temperature can be obtained.

In the beam flux measurement position, an ion gauge is able to measure the beam equivalent pressure (BEP), which represents the number of atoms that land onto unit area of the substrate. The beam flux measurement gives a rough control of the growth rate and can be used as a reference when setting up the temperature for the effusion cells.

The beam flux measurement position is also the "cooling position" for the substrate cooling before aluminum deposition. During the cooling process, the heater and all effusion cells are idled to make sure no extra heat can be transferred to the substrate. The cryopump that has a very low temperature (10K-40K) is able to absorb heat from the substrate through radiation and cool down the substrate. This process can cool the substrate to about -40°C.

RHEED system

An in-situ reflection high-energy electron diffraction (RHEED) system is used to monitor the growth process. In the RHEED setup, the electron beam is incident on the substrate at a very shallow angle. Because of the wave-like property of electrons, the beam is diffracted by the atoms on the surface layer of the substrate and then the diffraction pattern is collected on a phosphorus screen. The diffraction pattern shows the reciprocal lattice information of the surface layer, which can be used to monitor the surface reconstruction of the sample during the growth.

Also, during layer-by-layer growth of a thin film, the intensities of each individual RHEED spot (usually more obvious on the specular reflection spot) fluctuate as each monolayer grows on the surface. The intensity goes to a maximum when an entire atomic layer forms. Therefore, measurement of the RHEED oscillation period can be used accurately measure growth rate.

The second (metallization) MBE chamber is mainly used for aluminum superconducting layer deposition. The aluminum source material is also loaded into an effusion cell. Other

setup, such as the manipulator-heater assembly and the RHEED system are also very similar to the main MBE chamber. The main difference between the two chambers is that the metallization chamber is attached with a cooling assembly (Figure 2.3). The main part of the cooling assembly is a cooler that is connected to a liquid nitrogen reservoir. During the cooling process, the substrate is rotated to the cooling position. The cooler is filled with liquid nitrogen and lowered to physically touch the substrate. The heat is transferred to the cooler through thermal conduction so the substrate is cooled down. The substrate can be cooled to about -75°C. The cooling process can be monitored by a type K thermocouple in contact with the back side of the wafer. An example of temperature vs. cooling time relationship can be found in Section 3.3.

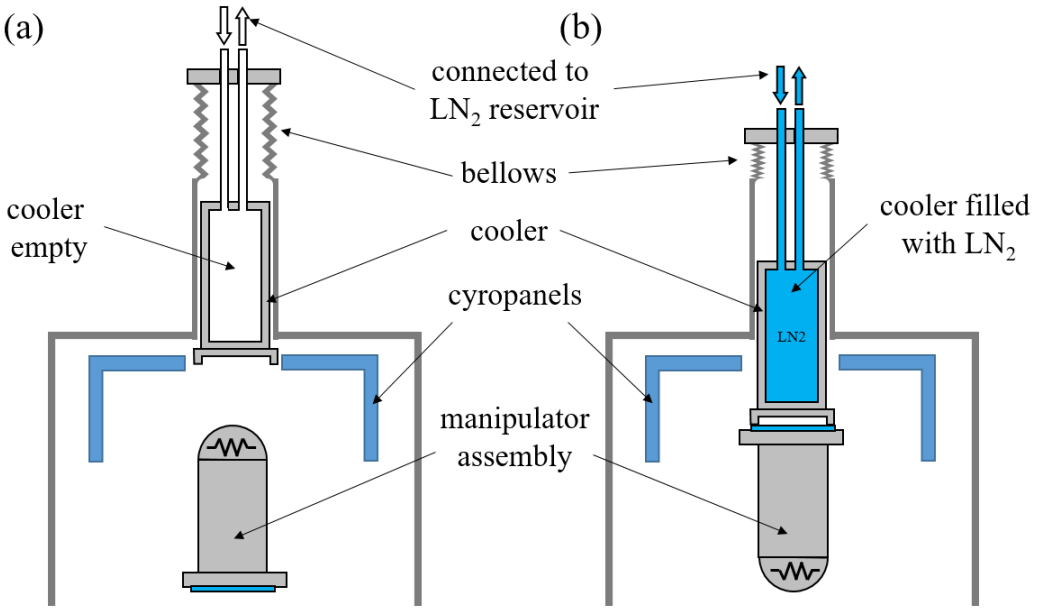

Figure 2.3. Cooling assembly in the metallization MBE chamber. (a) shows the status when cooling is not in progress. (b) shows the status when cooling is in progress. The substrate is rotated to the cooling position by manipulator. The cooler is filled with liquid nitrogen (LN_2) and lowered to make physical contact with the substrate holder.

2.1.3 MBE of the aluminum superconducting layer

In this work, the growth of the material includes two parts, the semiconductor growth and the aluminum growth. The semiconductor part of the material is typically an InAs quantum well structure grown on an InP(001) or a GaSb(001) substrate [22], [23], [77]. Other types of structures may also be grown for specific experimental reasons. A thin aluminum layer is then deposited on top of the semiconductor structure. Figure 2.4 presents a typical layer stacks of an InP based structure. Layer stack of other types of structures will be presented when needed. The epitaxy of the semiconductor heterostructures will not be described but reader can refer to [22], [23], [77] for more information.

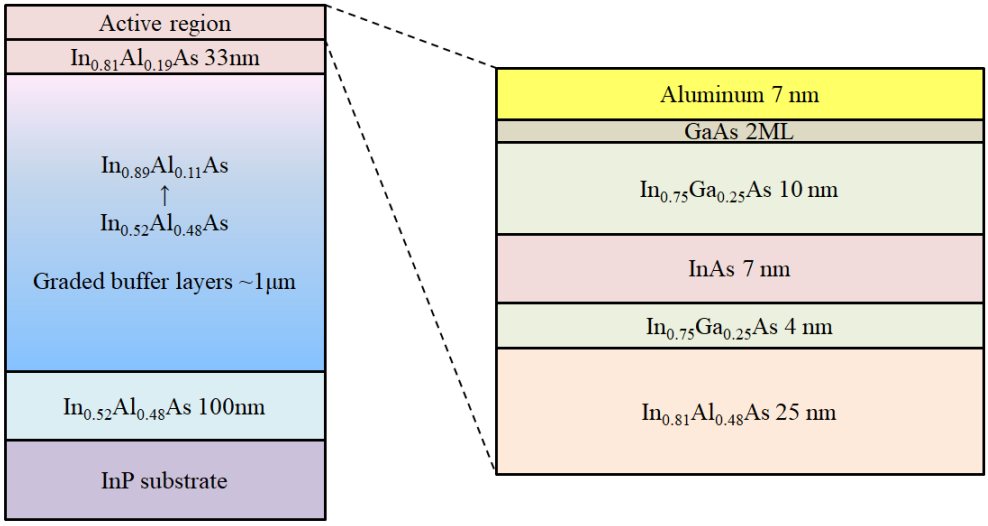

Figure 2.4. A typical layer stack of the Al-InAs quantum well heterostructure grown on an InP substrate. The left stack shows an overview of the structure. The right stack shows the layer structure in the active region.

After the growth of the semiconductor structure, the sample is cooled down in an As overpressure to 200°C. The surface reconstruction of GaAs layer is (3×2) which is the same for all growth. Note the normal surface reconstruction of bulk GaAs in As-rich condition is (2×4), c(2×8) or c(4×4) [78]. The (3×2) reconstruction implies that the two monolayers of GaAs is strained to the underlying layer. Then the sample needs to be cooled down for the aluminum layer deposition. After cooling, the aluminum cell is heated up for deposition.

In current experiments reported in this document, the deposition rate is 0.07 nm/s, which requires aluminum cell temperature 1070°C for the main MBE chamber, and 1170°C for the metallization chamber. Then the sample is rotated to the growth position for aluminum deposition. Some details of the operation are discussed below.

Aluminum cell stabilization

The aluminum cell temperature is raised initially from its idle temperature 775°C by a rate of 20°C/min. When the temperature is 20 °C below the desired temperature, the rate is decreased to 5°C/min. This gives more time for the aluminum cell to reach a stable temperature and protects the cell. Another aspect to consider is the transient (higher aluminum atomic beam flux when opening the shutter) caused by the shutter, which leads to non-uniform deposition rate and potentially bad morphology of the aluminum layer. To solve this problem, the aluminum shutter is opened for 2-3 minutes after the cell temperature is stabled, while the substrate remains in the cooling position.

Iterated deposition

When in the deposition position, the substrate surface is heated by the aluminum cell through radiation. To avoid excessive heating, aluminum deposition is divided into several stages. Take the growth of a 7 nm aluminum film for example. The total deposition time, 100 seconds, is divided into three stages. In the first stage, aluminum is deposited onto the sample for 33 seconds, followed by a 5-minute cooling period where the sample is rotated back to the cooling position. This process is then repeated twice, resulting in a total deposition time of 100 seconds.

Fast sample removal

After the deposition is done, the sample is transferred to the load-lock and then to the atmosphere environment quickly, normally less than 10 minutes. The reason to do this quickly is to oxide the aluminum layer at a lower-than-ambient temperature. The oxide layer on top can prevent the aluminum layer from reaching equilibrium state at room temperature (balling up) [19], which helps to improve surface morphology.

2.2 Transmission Electron Microscopy (TEM) characterization

The characterization of the aluminum film requires an understanding of its atomic structure. In order to obtain atomic-level information, Transmission electron microscopy (TEM) [79], [80] is used. Comparing to TEM, diffraction techniques such as X-ray diffraction are also very powerful in capturing atomic structure information. However, a diffraction technique probes only the statistical average of the material over a large region. It does not capture any local information. Different techniques should be chosen to address different questions. In this work, the local information of the aluminum film, such as the epitaxial orientation, the structure of the epitaxial interface, and the grain boundaries, is extremely important. Therefore, the TEM technique is used to characterize the local atomic framework in the film. This section is dedicated to an introduction to the TEM technique that is used in this work. A discussion about the interaction between the incident electron and the specimen is presented at first. After that, the imaging process of a transmission electron microscope will be discussed briefly. The sample preparation technique will be presented at last.

2.2.1 The electron-specimen interaction

In general, electrons are scattered by the electrons and nuclei in the specimen of the material through Coulomb interaction. Figure 2.5 presents different interaction modes between the incident electrons and the specimen. According to whether the incident electron loses

energy, one can classify the scattering process as elastic and inelastic scattering.

In elastic scattering, the electrons interact with the atoms in the specimen without los-

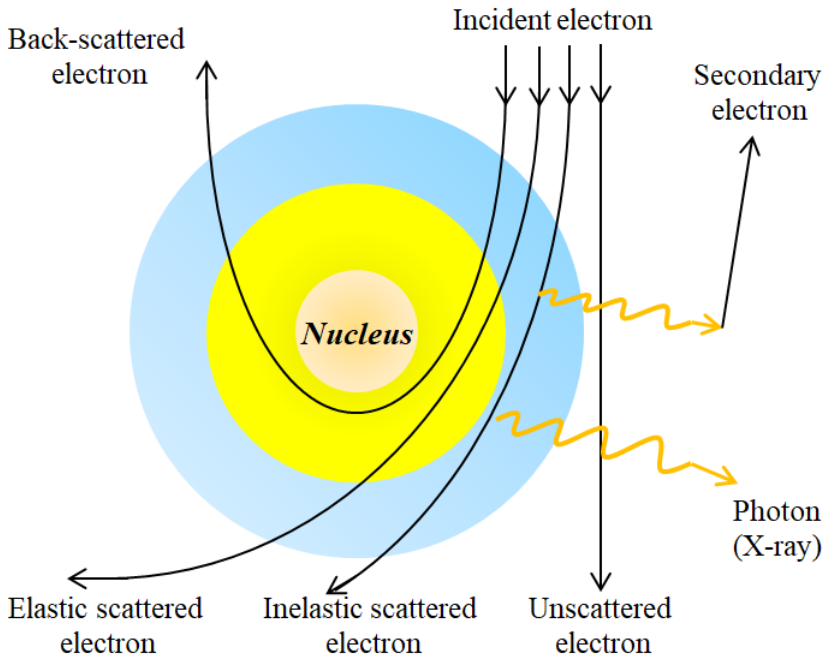

Figure 2.5. Electron scattering signals in electron microscopy. The incident (probe) electron beam interacts with the atoms by Coulomb interaction and create different types of scattering signals, that can be used in different EM modes.

ing energy. Depending on how close the incident electron is to the nucleus, the angle of the scattering varies. Some electrons travel through the specimen while others with extremely high scattering angles are scattered back to the same side with the incident electrons. The intensity of the signal of the back-scattered electrons (BSE) is highly related to the atomic number Z of the material, which can be used to form Z-contrast in scanning electron microscopy (SEM) technique [81]. The electron back-scattering diffraction (EBSD) technique also uses the back-scattered electrons to form diffraction patterns to reveal the crystallography of the material [82].

In inelastic scattering, the incident electrons lose part of their energy to the atoms in the specimen and increase the energy level of the atoms. The atoms then emit photons (mostly X-rays) when transiting back to their ground states. The signal of the emitted X-rays are

widely used in techniques such as Energy-dispersive X-ray spectroscopy (EDX) to detect the atomic species of the material [83]. The inelastic scattering process also generates secondary electrons (SE). The intensity of the SE is sensitive to the morphology of the specimen surface and can be used to detect the surface morphology in the SEM technique [81].

In TEM, the signal of the electrons that are transmitted through the specimen gets collected, including the unscattered and scattered electrons. High-angular scattered electrons can also be used to form Z-contrast, mainly used in scanning transmission electron microscopy (STEM) [84]. When an electron beam travels through a crystalline specimen, Bragg diffraction happens because the beam scattered by different atomic planes undergoes constructive interference at certain angles. The diffracted beams carry diffraction information from the specimen as well as phase change caused by different traveling distance in the specimen. In this work, these two types of information are the main signals in use. The phase change information is captured to perform high-resolution imaging (HRTEM) [85], [86]. The diffraction pattern (DP) is used to reveal the crystallography of the aluminum film as well as performing dark-field imaging (DFTEM) [87].

2.2.2 The TEM imaging

In this section, a fundamental picture of the TEM imaging is presented to explain the imaging process and the different imaging modes used in this work. In this picture, the specimen is illustrated by a broad parallel electron beam. Figure 2.6(a) shows the ray diagram of this case. The electron beam is created by a filament and accelerated by a high acceleration voltage. With an acceleration voltage U, the relativistic wavelength of the electron beam is written as:

$$\lambda = \frac{2\pi\hbar}{\sqrt{2m_0 \mathrm{e}U(1+\frac{\mathrm{e}U}{2m_0c^2})}} \tag{2.1}$$

where m_0 is the rest mass of the electron, e is the elementary charge, $\hbar$ is the Planck's constant and c is the speed of light in vacuum. A condenser lens system is placed between

the electron gun and the specimen to control the shape and intensity of the beam. The condenser lens system converges the electron beam to a parallel one.

The electron beam then interacts with the specimen creates diffracted beams. The diffracted beams leave the specimen with different diffraction angles determined by Bragg's law. As presented in Figure 2.6, the objective lens focuses these diffracted beams on the back focal plane and forms a diffraction pattern. The diffraction pattern is essential to revealing the crystallographic properties of the specimen.

The diffraction beams are then brought to interference on the intermediate image plane

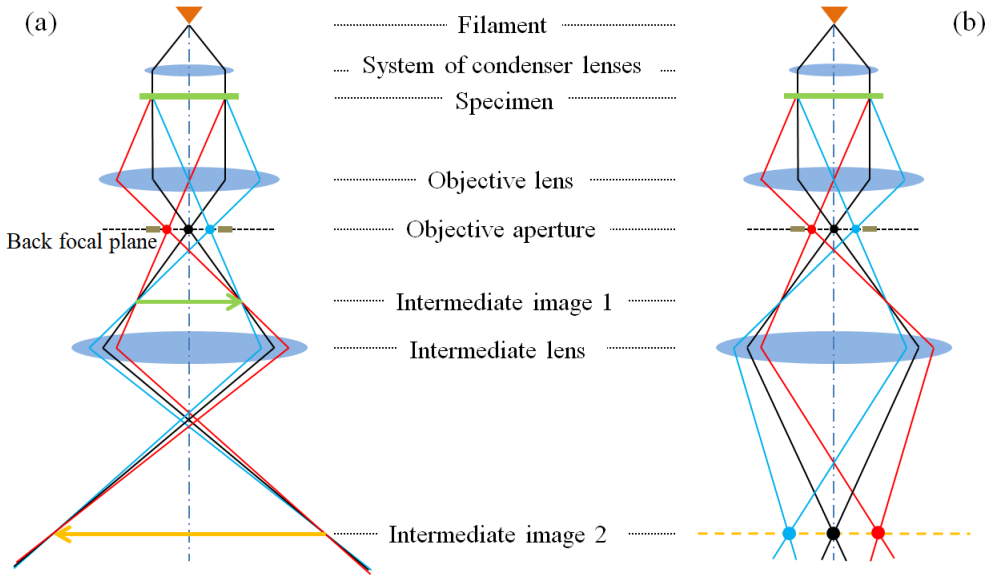

Figure 2.6. The TEM beam diagram when imaging a specimen using a parallel electron beam. (a) shows the imaging mode (b) shows the diffraction pattern mode. In both modes, parallel electron beam is formed by condenser lens system and illuminates the specimen. After diffraction, transmitted beam (black) and diffracted beams (red and blue) are generated. The beams are then focused to form a diffraction pattern on back focal plane of the objective lens and the diffraction pattern is recombined to form an intermediate image. The intensity of the intermediate lens can be tuned. In imaging mode (a), the object plane of the intermediate lens is tuned to the intermediate image 1 so an image of the specimen will form. In diffraction mode (b), the object plane of the intermediate lens is tuned to the diffraction pattern so an image of the diffraction patter will form. In both cases, there is also a projector lens (below the intermediate image 2) that transfers intermediate image 2 into a final image, which is not drawn in this diagram.

1 and the image is formed. There are also intermediate lenses in the electron optics that further transfer and enlarge the image into a final one. Also, by adjusting the intermediate lens, one can directly image the diffraction pattern (DP mode) on the back focal plane, as shown in Figure 2.6(b).

High-resolution TEM imaging

The diffraction beams experience phase changes that are determined by the structural properties of the specimen. The origin of the phase change can be illustrated by a simplified model, in which the incident electron beam contains individual electrons with the same phase. Assume the crystal potential in the specimen is $V(\mathbf{r})$. An electron that traverses the specimen at position $\mathbf{r_1}$ gains energy $eV(\mathbf{r_1})$ while traveling inside the specimen. As a result, its wavelength changes from λ to λ_1 inside the specimen. Another electron that traverses the specimen at a different position $\mathbf{r_2}$ gains energy $eV(\mathbf{r_2})$ while traveling inside the specimen. Its wavelength λ_2 inside the specimen is also different from λ_1. As a result, the electrons that traverse the specimen at different positions should have a phase shift that reflects the difference in wavelength. This explains why the phase changes of the diffraction beams carry the information of the structural properties of the specimen. When multiple diffraction beams are brought to interference on the image plane, the phase changes are translated into intensity contrast. This is the mechanism of high-resolution TEM imaging.

It is necessary to talk about the resolution limit of the TEM. Although the electron wavelength is a limiting factor of the resolution, one cannot conclude that the smaller the wavelength the higher the resolution. The wavelength is not the only limiting factor of the resolution. In this work, two TEM systems were mainly used to perform high-resolution imaging, a Thermo Fisher Talos TEM operated at 200kV and a Thermo Fisher Themis-Z Double Corrected TEM operated at 300kV. The electron wavelength in the two systems is 2.5 pm and 2 pm, respectively. However, the resolution of the two systems is about 100 pm and 65 pm, which are nearly two orders of magnitude higher.

An important limiting factor of the resolution is the effect of aberrations of the electro-

magnetic lenses. An aberration is a non-ideal imaging characteristic that deviates the image from the real object. The lens aberrations cannot be corrected by simply adding another compensating lens. A series of corrector lenses must be introduced. Electromagnetic lens aberration correction has been developed in later years and has introduced important break throughs in for TEM [88]–[91]. At present, the highest resolution obtained by HRTEM technique is around 50 pm [91]. Readers can refer to Reference [92] for a review of this topic.

Dark-field TEM

With an objective aperture on the back focal plane of the objective lens, one is able to select only one (or several, depends on the size and shape of the aperture) reflection to form the image and block other reflections (including the unscattered beam), shown in Figure 2.7. This is called the dark field mode of TEM. In this mode, one is able to light up only the part of the specimen that satisfies Bragg's law. The most direct application of dark-field imaging is to extract the grains with a specific epitaxial orientation from the grains with all kinds of orientations. Figure 2.8 shows an example of analysis for the grain orientation in an aluminum film. In this example, the grains with (111) out-of-plane orientation are illuminated by selecting the corresponding reflection and covering others. Grains with other orientations are all dark.

In this thesis, the DFTEM imaging technique is mainly used in the plan view imaging of the aluminum film. The typical thickness of the TEM sample by our preparation technique (as discussed in the next section) is around 100 nm. Since the thickness of the aluminum layer is only 5 to 10 nm, a large portion in the thickness of the plan view sample is the semiconductor layers. In this case, normal TEM imaging is not able to distinguish the aluminum layer from the coverage of the semiconductor layers. However, since the diffraction pattern of aluminum and semiconductor are different, the reflections are separated in the back focal plane. By selecting only the aluminum reflections with the aperture and covering

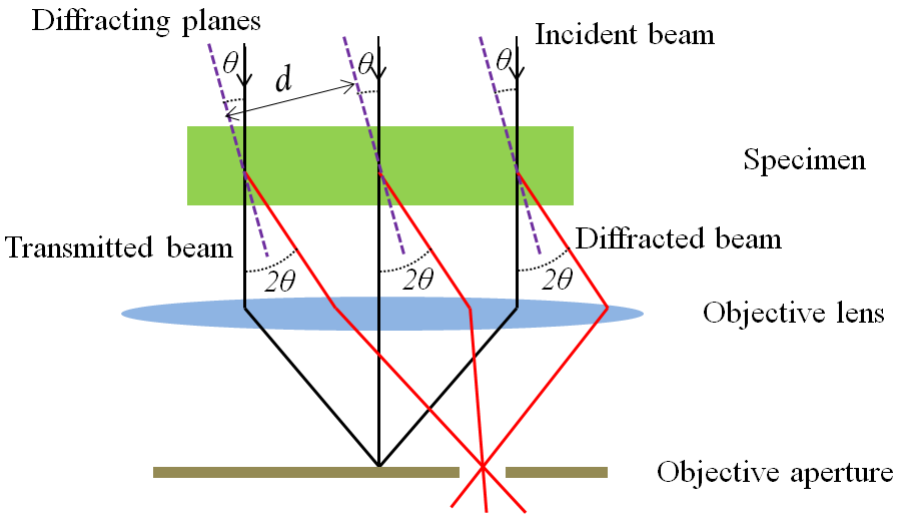

Figure 2.7. Diffraction pattern and dark-field imaging in TEM. After interacting with the specimen, the diffraction beams are directed to specific angles that satisfy Bragg's law. The transmitted beam (black) and diffracted beams (red) are then focused to form reflection spots in the diffraction pattern. In dark-field imaging, an objective aperture is used to allow only certain diffracted beams to form image and block other beams by selecting certain reflections in the diffraction pattern.

the semiconductor reflections, the aluminum layer can be observed.

2.2.3 TEM Sample Preparation

Electron transparency is one of the most important requirements for a TEM sample. For most low magnification analysis, 100 nm is thin enough to be transparent, while for HRTEM imaging, the sample needs to be thinner than 50 nm [93]. Other aspects such as flatness and uniformity are also essential. One of the biggest challenges in TEM is to make a good sample.

There are many ways to prepare a sample for TEM. The method one should choose has to be related to the type of material and the information to be obtained. One major consideration to the sample prep. method is that such a technique must not affect crystal and chemical information to be obtained with TEM. In this work, both traditional mechanical

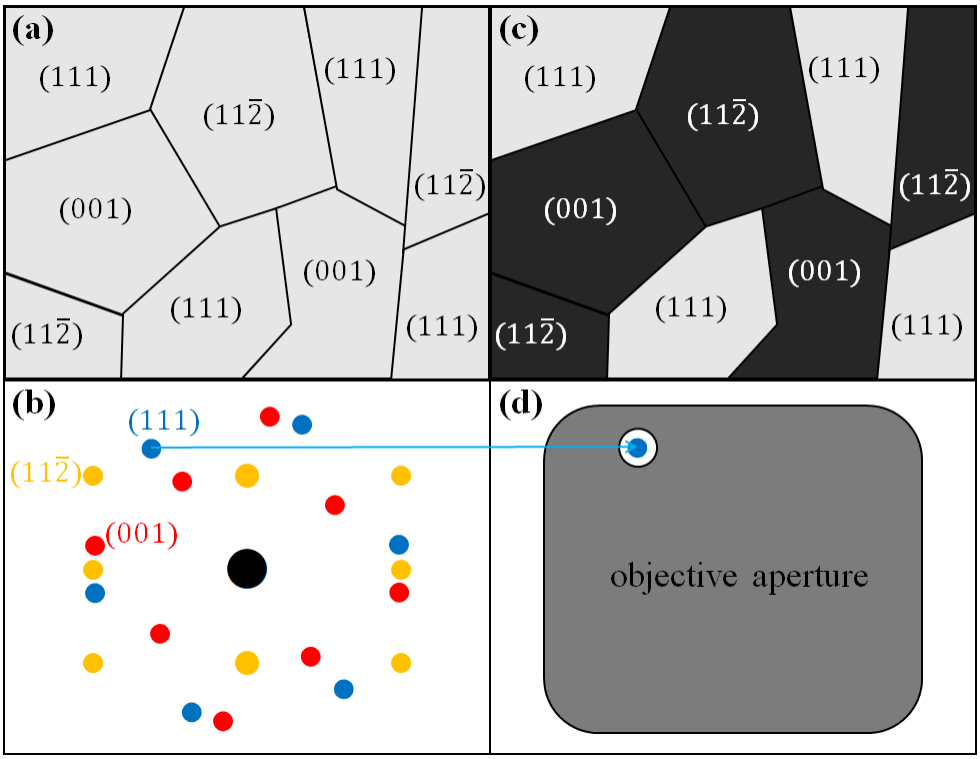

Figure 2.8. An example of grain orientation analysis using dark field TEM. (a) shows a TEM image (diagrammatic sketch) of an area of aluminum crystal that contains grains. (b) shows diffraction pattern of this area, which contains diffraction pattern of aluminum crystal with out-of-plane orientation (111) (marked by blue), (001) (marked by red) and (11$\bar{2}$) (marked by yellow). By looking at (a) and (b), one cannot map out the grains with the orientations. By selecting one of the (111) reflection using an aperture, shown in (d), the grains with (111) orientation is lightened up with other grains dark, shown in (c).

polishing and focused ion beam (FIB) [94] were developed to prepare TEM samples of the aluminum film. For InP-based samples, FIB is a good method. However, for GaSb based samples it was noticed that Ga^+ ion beam can damage the aluminum layer by mixing the aluminum layer with the semiconductor layer below. Therefore the traditional mechanical polishing technique was used, in which a Precise-Ion-Polishing Sytem (PIPS) was used with ion beam energy as low as 250 eV. Both techniques are briefly described as follows.

Traditional ion-milling technique

The traditional ion-milling technique needs a pre-polishing step preformed with a mechanical polisher before the usage of a low energy ion beam milling (PIPS) process. Figure 2.9 shows a general step-by-step schematics of the process to prepare a cross-section sample of the aluminum/semiconductor heterostructure with the ion milling method. In the first step, two pieces of the sample with 2 mm $\times$ 3 mm in dimension are glued together, with the aluminum layer inside, in order to make a "sandwich", as shown in Figure 2.9(a). Then the sandwich is thinned down to 30-50 μm with a mechanical polisher, as shown in Figure 2.9(b). In the next step, a dimpler is used to further thin down the specimen to 5-15 μm, as shown in Figure 2.9(c). The curvature of the sample's surface is caused by the Cu wheel of the dimpler during the grinding process. The final step is to mill the sample with the Precision-Ion-Polishing system (PIPS). Figure 2.9(d) shows a sketch of the ion-milling process. In the preparation for cross-section samples, two Ga^+ ion beams are used to thin the sample from the two sides, respectively. Also, the sample holder usually makes physical contact with a liquid nitrogen dewar, in order to protect the sample from heating up by the ion beams. After this process, a small hole will be created at the center of the sample, on the line of the glue. The thin area that is electron-transparent is around the hole created, as shown in Figure 2.9(e).

Focused Ion Beam Technique

Compared to traditional ion-milling, FIB is a more advanced technique that gives a better control of the milling parameters (milling region, sample thickness and beam angle). It is also more efficiency. A normal in-situ lift-out FIB process doesn't require any mechanical polishing steps so it shortens the total time cost of the process. A FIB instrument consists of two ion beam columns (electron and ion). The SEM beam is mainly used for imaging the specimen's surface during the whole process. The ion beam (Ga^+) is at an angle of 52° related to the SEM beam. A sample holder can be manipulated to adjust the incident angle of both beams (shown in Figure 2.10) to proceed milling with different purpose.

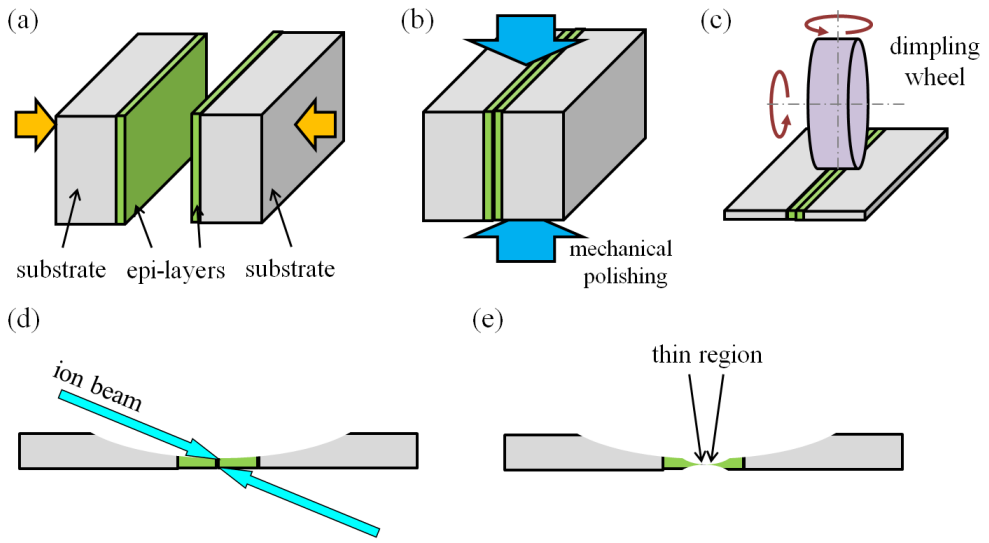

Figure 2.9. Traditional ion-milling technique of cross-sectional TEM sample preparation. (a) Cut and glue the sample with grown layer inside. (b) Mechanical polishing the sample to 30-50 nm. (c) Use dimpling wheel to grind the center of the sample. (d) Mill the sample with ion beam until a hole appears at the center. (e) Final status of the sample. The thin region is at the edge of the hole.

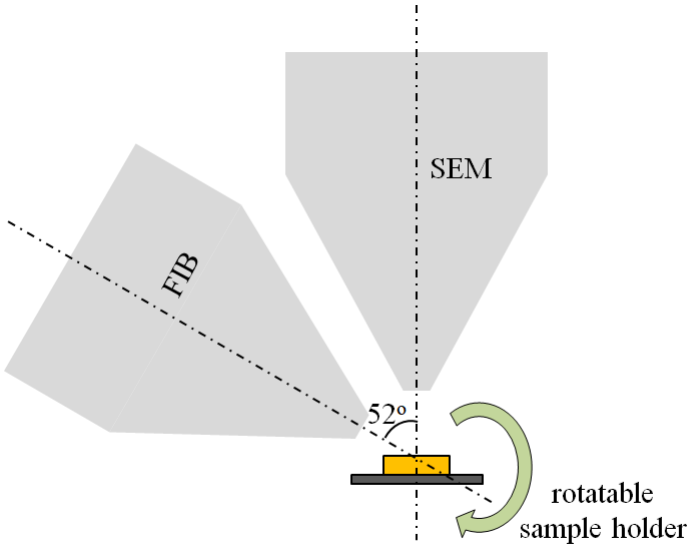

Figure 2.10. A normal FIB system contains SEM and FIB columns that are separated by 52°. A sample holder can be manipulated to adjust the incident angle of each beam onto the sample.

Figure 2.11 shows a normal in-situ lift-out process to prepare a cross-section TEM sample. At the beginning of the process, a bulk sample is loaded into the FIB chamber. In the FIB chamber, a Pt protection layer is deposited onto the interested area (Figure 2.11(a)). By milling away the material at the front and back side with focused ion beam, a thin lamella is created (Figure 2.11(b) and (c)). At the end of this process, the connections between the lamella and the bulk sample on the bottom and two sides of the lamella are milled away so the lamella is removed. Then the lamella is lifted out by a manipulator tip and attached onto the TEM sample grid by Pt deposition (Figure 2.11(d)). After that, finer thinning is performed on the lamella to thin the sample to a required thickness.

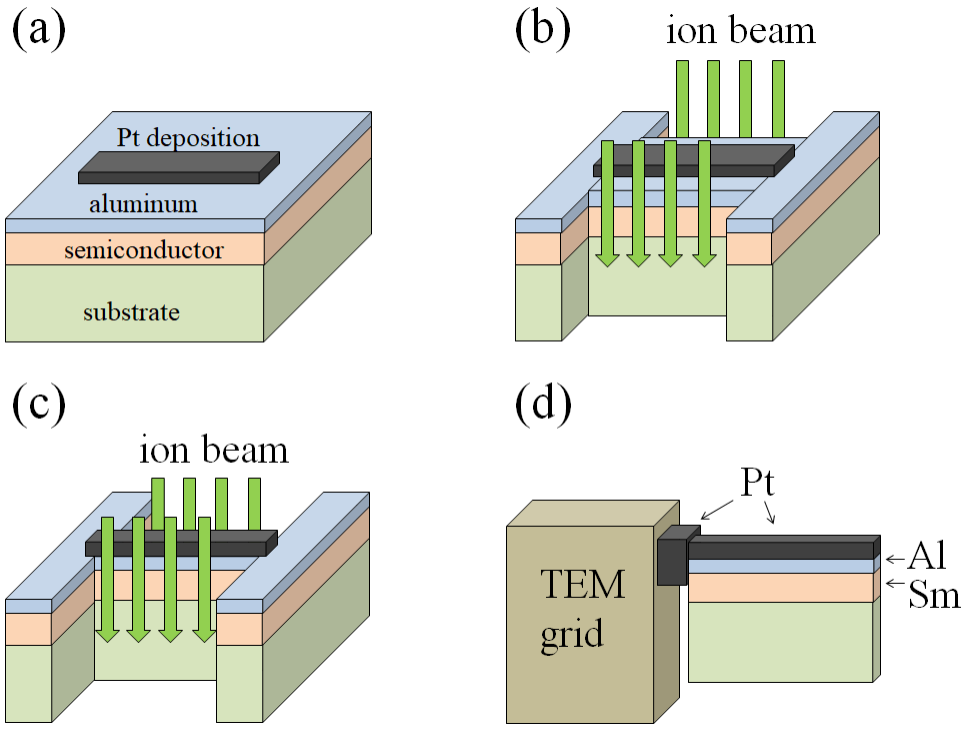

Figure 2.11. A schematic diagram of in-situ lift-out FIB process for cross-section sample preparation. (a) A Pt layer is deposited to protect the sample. (b) and (c) A lamella is made from the bulk sample by milling down the material in front of and on the back side of the lamella. (d) The lamella is removed from the bulk sample and attached to the TEM sample grid for further thinning.

The normal in-situ lift-out process does not apply in the preparation of a plan view sample. Instead, H-bar FIB process is developed to do the job. In H-bar FIB process, a small piece of the sample is cut and attached to the TEM half-grid with the aluminum side facing to the grid. Then the sample is mechanically milled from the substrate side until the remaining thickness is 10 to 20 μm. The sample is then put into the FIB for finer thinning. Figure 2.12 shows a sample after mechanical polishing is milled under focused ion beam. The process is named after the shape of the sample and the grid. One advantage of this process is that it prevents the sample from being exposed to ion beam for too long.

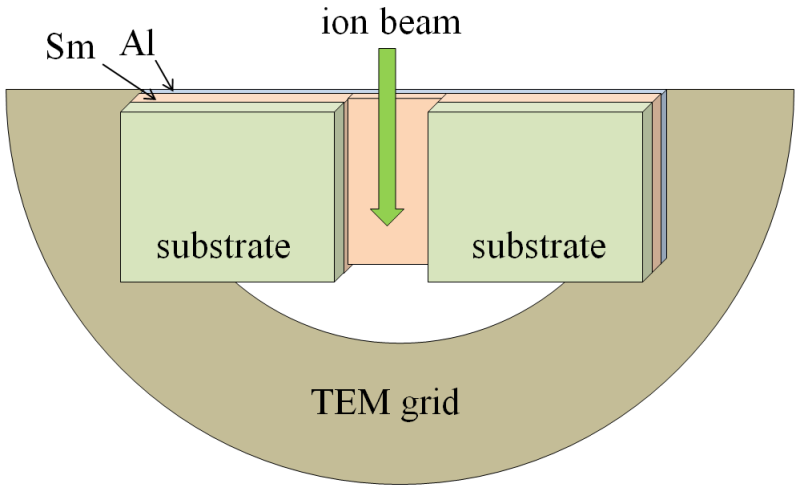

Figure 2.12. In H-bar FIB process, a sample that is already mechanically thinned down is being milled under focused ion beam. The sample was attached to the TEM half-grid with the aluminum side facing to the grid and milled down to 10-20 μm from the substrate side and then put into the FIB chamber for finer thinning.

Note the final plan view sample always contains a significant amount of the semiconductor layer on the back side of aluminum (In Figure 2.12 it is presented by the thin pink layer behind the blue aluminum layer). The beam can be tilted to create a wedge of the sample so the proportion of the aluminum improves near the tip of the wedge. However, DFTEM techique is always needed to observe the aluminum layer.

2.3 X-ray Diffraction (XRD) characterization

2.3.1 Principle of XRD characterization

X-ray diffraction (XRD) is also a powerful technique for characterizing crystalline materials. Unlike TEM, XRD characterization is nondestructive and doesn't need sample preparation. As a result, XRD is sometimes more efficient and has a shorter loop of feedback between the growth and characterization. Also, XRD gives an average measurement on the entire detected region while TEM characterize the crystal properties more locally. So sometimes it is important to combine the two technique to have a complete understanding of the sample.

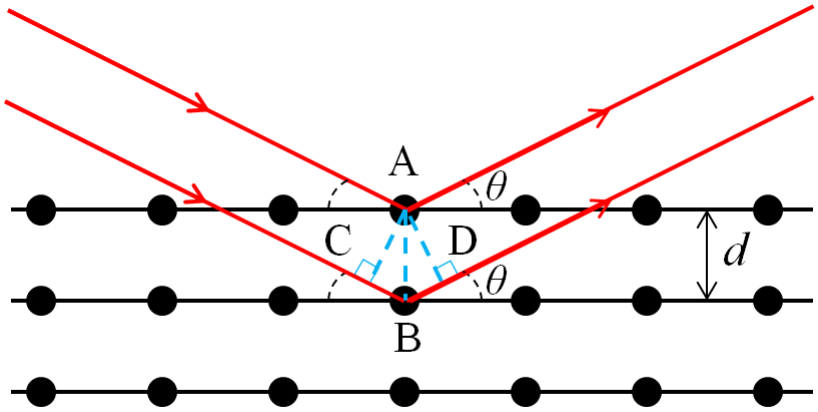

Figure 2.13. Bragg's Law of X-ray Diffraction. The X-ray beam that is reflected by a set of atomic planes in the sample shows constructive interference only if the wave path difference is equal to an integer times the wavelength. In this diagram, the wave path difference is $BC + BD = 2d\sin\theta$. So Bragg's law takes form $n\lambda = 2d\sin\theta$.

The principle of XRD simply follows the Bragg's law. Figure 2.13 shows a short derivation of it. Consider crystal to be a set of arrays of atoms. The incident X-ray beam as electromagnetic wave can be elastically scattered by the atoms (actually scattered by the electrons in the atoms). And then the wave scattered by different atoms will interfere with each other.

In certain directions, the interference shows constructive interference peak. Similar with the discussion in 2.2.1, the Bragg's law takes exactly the same form:

$$2d\sin\theta = n\lambda \tag{2.2}$$

Contrary to TEM, where diffracted electron beams are converged by the objective aperture so that the reflections can be seen on the screen, in the use of XRD the X-ray detector scans the intensity of diffracted X-ray beam in certain measurement geometry. The peak angle θ implies a set of atomic planes with spacing d. The key to XRD analysis is to choose certain scan geometry for different applications. The next section will discuss two types of scan geometry used in the aluminum characterization in this thesis, the $\theta - 2\theta$ scan and the $\phi-$scan.

Note both TEM and XRD technique are capable to characterize the normal orientation of the aluminum. However, different aspects are emphasized. In TEM imaging, it is possible to see how atoms arrange in a very detailed length scale. By XRD analysis, one can see an statistical result of the sample in a much larger scale. For instance, the distribution of epitaxial orientations can be obtained. Residual strain of the aluminum layer can also be obtained by looking at how the lattice spacing d is different from on bulk value (as shown in Chapter 3).

2.3.2 Application of XRD in sample characterization

One obvious application in this thesis is to determine the growth orientation of the aluminum layer. By symmetrically scanning the incident and diffracted X-ray beam, one is able to obtain the lattice spacing of aluminum along the surface normal direction and therefore obtain the growth orientation (Figure 2.14). This is called the symmetric $\theta - 2\theta$ scan since the scan is performed by rotating the sample by angle θ and rotating the diffraction beam detector by angle 2θ simultaneously.

Besides the scan geometry used to characterize the aluminum layer, this thesis also used reciprocal space mapping (RSM) technique to measure the in-plane lattice parameter of the

surface of the semiconductor on which the aluminum layer was deposited on. Readers can see Reference [95] as a review of the principle and applications of the RSM technique. The following discussion focuses on how this technique is applied to measure the semiconductor lattice parameter on the surface.

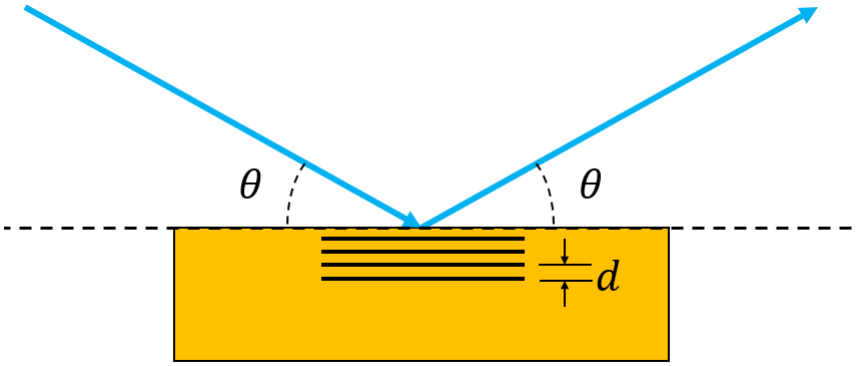

Figure 2.14. XRD symmetric $\theta - 2\theta$ scan configuration to obtain the growth orientation. By symmetrically scanning both incident and diffracted beam, the intensity peak angle θ reveals the lattice spacing d along the growth direction.

Figure 2.15 showed a typical RSM data collected on a sample with the layer stack in Figure 2.4 using the (224) reflection. In this RSM, one can see that the intensive red peak which showed the reflection of the InP substrate. The substrate peak was followed by a near continuous yellow and green area that showed the graded buffer layer grown on top of the substrate. In most part of this graded buffer area, the peaks developed in such a way that the scattering vector in both in-plane (q_x) and normal (q_z) direction decrease, which translated as the lattice parameter of both directions increase. This agreed with the design of the graded buffer layer. Note the in-plane lattice parameter stopped increasing at the end of the graded buffer layer and only the normal lattice parameter still increased. This also matched the graded buffer layer design which produced dislocation free "peudo-substrate" to let active region grow on it. From then on to the surface of the semiconductor, the in-plane lattice parameter had little change. To evaluate the in-plane lattice constant on top of the semiconductor, the value of q_x where the in-plane scattering vector stopped decreasing was

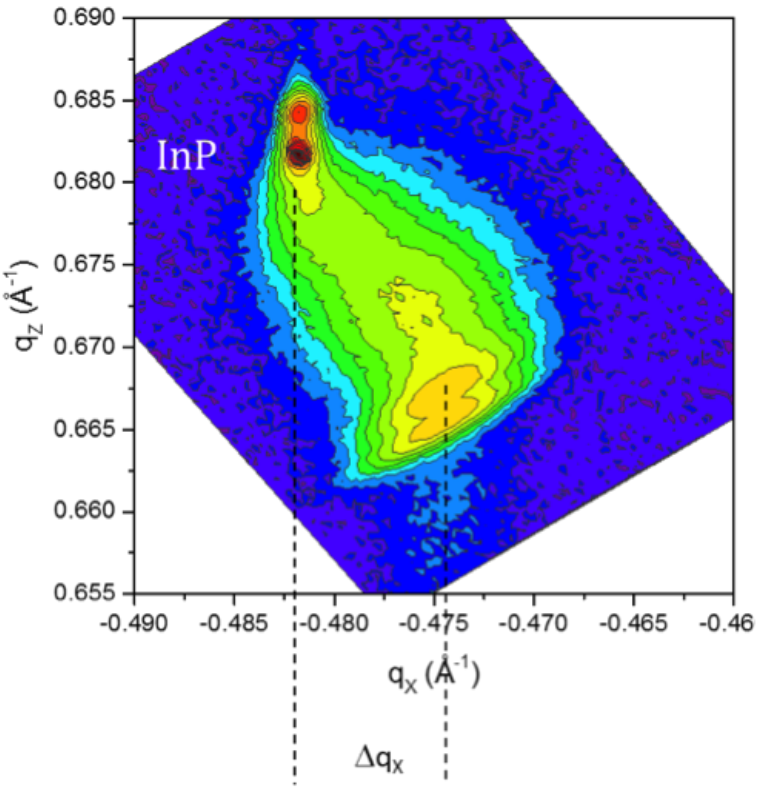

Figure 2.15. A typical reciprocal space map collected on a sample with layer stack Figure 2.4 using (224) reflection. q_x and q_z represent the scattering vector in the in-plane and normal direction, respectively.

extracted from the data. The lattice parameter is: $a_{\text{surf}} = 8^{0.5}/q_{x,\text{surf}}$.

In Chapter 3, the above measurement is applied to the samples in this thesis to show the dependence of the aluminum orientation on the semiconductor surface lattice parameter.

3. GROWTH ORIENTATION OF THE ALUMINUM FILMS

This chapter will be dedicated to study the growth orientation of the aluminum film. Although the concept was introduced in Chapter 1, it is necessary to repeat the definition here to have a clear discussion. The growth orientation is the crystallographic orientation of the aluminum film that is parallel to the surface normal direction of the sample, i.e., the direction of the sample growth. For instance, in the notation of epitaxial orientation "Al(111)[1$\bar{1}$0] || InAs(001)[1$\bar{1}$0]", the growth orientation of the aluminum film is (111). An aluminum film can either have a pure growth orientation if there is one single growth orientation for all parts of the film, or have a mixed growth orientation if there are multiple growth orientations for different parts of the film. In this chapter, the growth orientation of the aluminum film on different samples are examined in order to study important factors the growth orientation depends on.

3.1 Sample growth

The samples used to study the growth orientation is presented in this part. For convenient discussion, the semiconductor heterostructure is described as a combination of substrates, buffer layers, top layers and capping layers, depicted in Figure 3.1. An example of the heterostructure has already been shown in Figure 2.4, in which the substrate was InP(001), the buffer layers were a series of $In_xAl_{1-x}As$ graded buffer layers, the top layers were an InAs quantum well structure and the capping layer contained two monolayers of GaAs. In this study, seven samples were grown using the MBE system discussed in Chapter 2. The samples are numbered as S1 - S7. To be clear, Table 3.1 lists the important information of the samples. Among them, Sample S1 - S4 are representative of complete device structures used in MZM transport experiments and sample S5 - S7 are designed to study how Al behaves when deposited onto a surface with different lattice parameters (S6 and S7) and different surface termination (S5).

For samples S1 - S3, InAs quantum wells were grown on semi-insulating InP substrates. $In_xAl_{1-x}As$ step graded buffer layers (GBL) grown at 380^oC were used to accommodate the

lattice mismatch between the InP substrate and the quantum well region[21]–[23], [96], [97]. For S1 and S2, along the length of the GBL the indium content was graded from 52% to 89%, followed by an inverse grade back to an indium content of 81%. For S3, the indium content was graded from 52% to 84%, followed by an inverse grade back to an indium content of 81%. The GBLs were designed so that the quantum well region, $In_{0.75}Ga_{0.25}As$(10nm)/InAs(7nm)/ $In_{0.75}Ga_{0.25}As$(4nm) (from top to bottom), was coherently strained. The difference in the design of the GBLs permitted a study of how the aluminum layer behaves as a function of semiconductor lattice parameter. These particular semiconductor heterostructures were capped by 2 monolayers of GaAs to serve as an Al etch stop during processing; this layer was identical for S1 - S4.

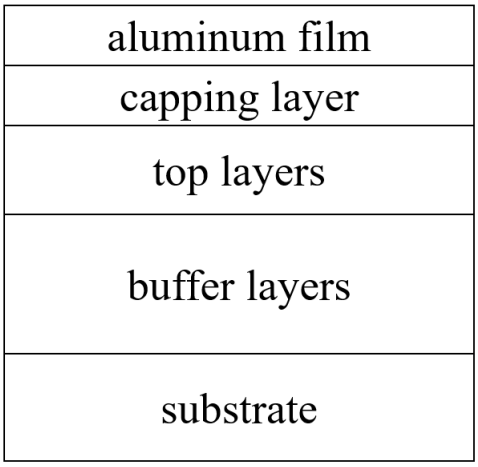

Figure 3.1. A sample can be described from bottom to top as: the substrate, the buffer layers, the top layers, a capping layer and the deposited aluminum film.

S4 was grown with a heterostructure design allowing further increase of the surface lattice parameter. To do so, the InAs quantum well was grown on an insulating buffer of $Al_{0.8}Ga_{0.2}As_{0.07}Sb_{0.93}$ lattice-matched to GaSb (6.096 [25]) [77], [98]. The S4 quantum well region, $In_{0.9}Al_{0.1}As$ (10nm)/InAs (7nm)/$Al_{0.8}Ga_{0.2}Sb$ (7nm), was designed to be coherently strained to the buffer layer to minimize dislocations. As a result, the surface lattice parameter was close to the value of GaSb. S5 has the same buffer layer design as S4 but with only the InAs (7nm) layer on top of the buffer layer. Comparison of S4 and S5 showed

Table 3.1. Identification and details for samples S1 - S7. Indices to the right of the substrate material are the lattice planes nominally parallel to the surface. In some cases, intermediate layers lie between the substrate and top semiconductor layers. GBL stands for graded buffer layer. For S1 - S4, the top layer is the top barrier of an InAs quantum well.

Sample	Substrate	Buffer Layers	Top Layer	GaAs(2ML)
S1	InP(001)	GBL $In_{0.52}Al_{0.48}As$ to $In_{0.89}Al_{0.11}As$	$In_{0.75}Ga_{0.25}As$	Yes
S2	InP(001)	GBL $In_{0.52}Al_{0.48}As$ to $In_{0.89}Al_{0.11}As$	$In_{0.75}Ga_{0.25}As$	Yes
S3	InP(001)	GBL $In_{0.52}Al_{0.48}As$ to $In_{0.84}Al_{0.16}As$	$In_{0.75}Ga_{0.25}As$	Yes
S4	GaSb(001)	$Al_{0.8}Ga_{0.2}As_{0.07}As_{0.93}$	$In_{0.9}Al_{0.1}As$	Yes
S5	GaSb(001)	$Al_{0.8}Ga_{0.2}As_{0.07}As_{0.93}$	InAs	No
S6	InP(001)	N/A	$In_{0.52}Al_{0.48}As$	No
S7	InAs(001)	N/A	InAs	No

whether the GaAs capping layer was able to affect the aluminum orientation and thus build a connection to S6 and S7 without the GaAs cap.

Samples S6 and S7 were grown to further study the effect on the aluminum layer when growing with other surface lattice parameters. S6 was grown on an InP (001) substrate with a single $In_{0.52}Al_{0.48}As$ buffer layer lattice matched to InP (5.869 [25]). S7 was grown on an InAs (001) substrate with an InAs buffer layer so the surface lattice parameter matches InAs (6.059 [25]).

After semiconductor growth, samples were cooled down before the aluminum deposition to prevent de-wetting and make layerlike growth [19], [54]. In all cases the substrate was cooled to at least - 40^{o}C. Both cooling procedures discussed in Chapter 2 were used. 7 nm thick Al films were deposited at a rate of 0.7 $/s$, measured by the in-situ Quartz Crystal Microbalance (QCM) for all samples.

3.2 Characterization of growth orientation

In this section, two sample, S1 and S4, were characterized using HRTEM technique to show how the characterization process was performed. Figure 3.2(a) shows a high-resolution cross-sectional TEM image of the aluminum layer in sample S1. The cross-section in the image was cut along the {110} direction of the semiconductor. The imaging was performed

using a Thermo Fisher Thalos TEM system operated at 200 kV. In this image, the sample was tilted by monitoring the semiconductor diffraction pattern such that the electron beam is along {110} direction of the semiconductor. The fast Fourier transformation (FFT) focusing on the aluminum layer is shown in Figure 3.2 (b). The FFT pattern matches the simulation of diffraction patterns of a face center cubic (FCC) crystal shown in Figure 3.2 (c). One can tell the direction of growth is well aligned with the [111] direction of the FCC simulation.

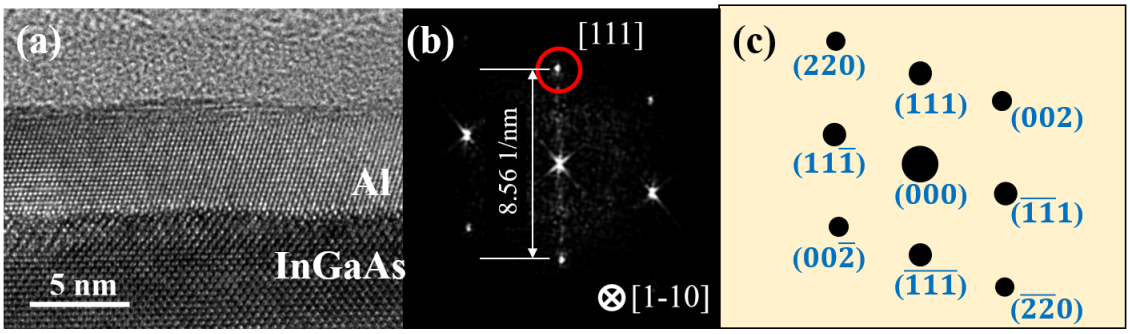

Figure 3.2. An HRTEM image of aluminum layer with (111) orientation in sample S1. (a) is an HRTEM image of the aluminum layer. (b) is an FFT of the aluminum layer in figure (a) (InGaAs layer is not included in FFT). The HRTEM image and the FFT pattern were calibrated with the scale bar in the HRTEM image. The distance between the [111] and $[\bar{1}\bar{1}\bar{1}]$ spots in (b) is measured by image processing software. (c) is a simulation of diffraction pattern of FCC crystal in $[1\bar{1}0]$ zone-axis.

Also, the distance between the [111] and $[\bar{1}\bar{1}\bar{1}]$ spots was measured by the image processing software. To be specific, the scale of the pixels was first calibrated by the 5-nm scale bar in the HRTEM image. And then the distance was measured by counting the number of pixels. The lattice spacing between the [111] atomic planes can be calculated as:

$$d_{[111]} = \frac{2}{8.56\ 1/\text{nm}} = 0.2336\text{nm}, \tag{3.1}$$

which is agreed with the lattice spacing of aluminum on [111] direction:

$$d_{\mathrm{Al}[111]} = \frac{a_{\mathrm{Al}}}{\sqrt{1^2+1^2+1^2}} = \frac{0.4049\mathrm{nm}}{\sqrt{3}} = 0.2336\mathrm{nm}. \tag{3.2}$$

With this analysis, one can also tell the growth orientation of the aluminum layer shown in Figure 3.2 (a) is (111).

On the other hand, Figure 3.3(a) shows an example of a high-resolution cross-sectional TEM image of the aluminum layer in sample S4. The cross-section in the image was also cut along the {110} direction of the semiconductor. The imaging was performed using a Thermo Fisher Thalos TEM operated at 200 kV. The conclusion of (110) orientation can be drawn by comparing the FFT pattern Figure 3.3(b) and the simulation diffraction pattern in Figure 3.3(c).

The distance between the [220] and [$\overline{2}\overline{2}$0] spots was also measured by the image processing software. The lattice spacing between the [220] atomic planes can be calculated as:

$$d_{[220]} = \frac{2}{14.0\ 1/\mathrm{nm}} = 0.1429\mathrm{nm}, \tag{3.3}$$

which is agreed with the lattice spacing of aluminum on [220] direction:

$$d_{\mathrm{Al}[220]} = \frac{a_{\mathrm{Al}}}{\sqrt{2^2+2^2+0^2}} = \frac{0.4049\mathrm{nm}}{\sqrt{8}} = 0.1431\mathrm{nm}. \tag{3.4}$$

It is noteworthy that for both sample S1 and S4, the analysis above was not only focused in a small area as shown in Figure 3.2 and Figure 3.3, but was confirmed in a wide sample area. This confirms that both sample S1 and sample S4 have a pure growth orientation, (111) and (110), respectively. The same analysis based on HRTEM technique was performed on all the samples shown in Table 3.1 to determine the growth orientation of the aluminum films. For sample S1, S3 and S6, the growth orientation was found to be pure (111), while S4, S5 and S7 showed a pure (110) growth orientation. Sample S2 showed a mixed growth orientation that contained both (111) and (110).

It is noteworthy that (110) normal orientation of aluminum was found in both S4 and S5,

even though they are terminated with different atomic species, GaAs and InAs respectively.

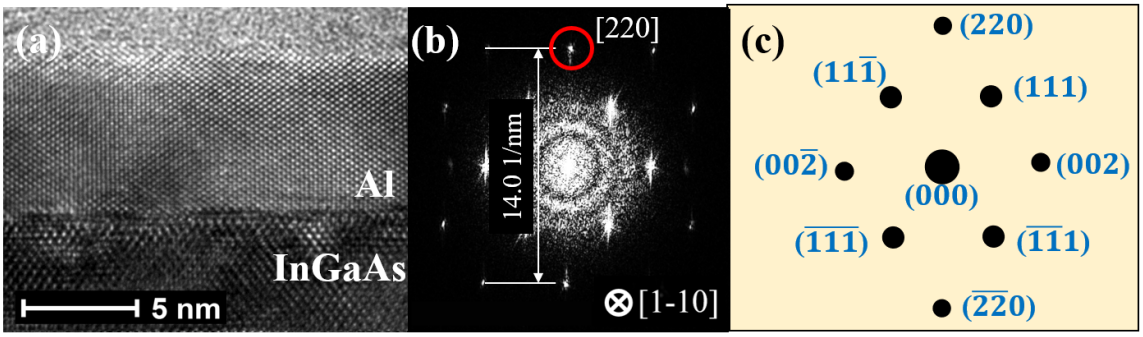

Figure 3.3. An HRTEM image of aluminum layer with (110) orientation in sample S4. (a) is an HRTEM image of the aluminum layer. (b) is an FFT of the aluminum layer in figure (a) (InGaAs layer is not included in FFT). The HRTEM image and the FFT pattern were calibrated with the scale bar in the HRTEM image. The distance between the [220] and [$\bar{2}\bar{2}$0] spots in (b) is measured by image processing software. (c) is a simulation of diffraction pattern of FCC crystal in [1$\bar{1}$0] zone-axis.

3.3 Dependence of growth orientation of aluminum films

3.3.1 Lattice parameter of semiconductor

To have a better understanding of the growth mechanism, a direct question is to ask what controlled the formation of different growth orientations. The problem is multi-dimensional. However, as one can see in the last section, a direct hint is that (111) aluminum film was mostly observed in heterostructures with an InP (smaller lattice constant) substrate, while (110) aluminum film was mostly observed in heterostructures with a GaSb (larger lattice constant) substrate. Based on this reason, the lattice parameter on top of the semiconductor heterostructure was measured on all samples in Table 3.1 and put together with their aluminum growth orientations to show dependence. The lattice parameters of the semiconductor heterostructures were measured by reciprocal space mapping (RSM) (Section 2.3.2).

Table 3.2. The relationship between normal orientation of aluminum layers and in-plane lattice parameter on the semiconductor surface. Surface lattice parameters are extracted from measured RSM data.

Sample	Surface lattice parameter (Å)	Al normal orientation
S6	5.87 ± 0.01	(111)
S3	5.94 ± 0.01	(111)
S1	5.98 ± 0.01	(111)
S2	5.98 ± 0.01	(110)&(111)
S7	6.06 ± 0.01	(110)
S4	6.10 ± 0.01	(110)
S5	6.10 ± 0.01	(110)

Table 3.2 contains a summary of the growth orientations and semiconductor top lattice parameters for all samples. The table exhibits a clear transition in Al growth orientation from (111) to (110) as the semiconductor top lattice parameter increases. Sample S2 that showed a mixed growth orientation is considered to be at the boundary of the transition.

A previous study showed Al taking a (110) normal orientation when deposited onto $In_{0.9}Al_{0.1}Sb$ (001) surfaces (lattice parameter 6.42), which supports the transition observed here [43]. To understand what parameter is driving the transformation from one orientation to another, further measurement of the residual strain of the aluminum layers were done.

3.3.2 Residual strain in aluminum layer

Sample S3, S5, S6 and S7 were chosen as representatives of different aluminum normal orientations to perform X-ray experiments to determine the relationship of the normal orientation and the residual strain in the aluminum layer.

In the experiments, the residual strain in the direction normal to the semiconductor surface is determined using symmetric $\theta - 2\theta$ scans discussed in Section 2.3.2. Figure 3.4(a) shows a symmetric scan of the (111) reflection of S3, which reveals a well-developped peak. The vertical dashed line through the peak at $q_z = 2.6874\ ^{-1}$ in Figure 3.4(a) represents the position of a strain-free Al (111) peak. A peak shift toward lower q_z in the figure indicates the presence of a tensile strain normal to the interface. On the other hand, Figure 3.4(b)

shows a symmetric scan of the (220) reflection of the Al layer from S5. A compressive normal strain is manifested by a peak shift to higher qz relative to the strain-free position at $q_z = 4.3886\ ^{-1}$. In summary, Samples S6 which exhibit the same normal orientation (111) as S3, all exhibit normal tensile strain. Sample S5 and S7, which exhibit the same normal orientation (110), all exhibit normal compressive strain.

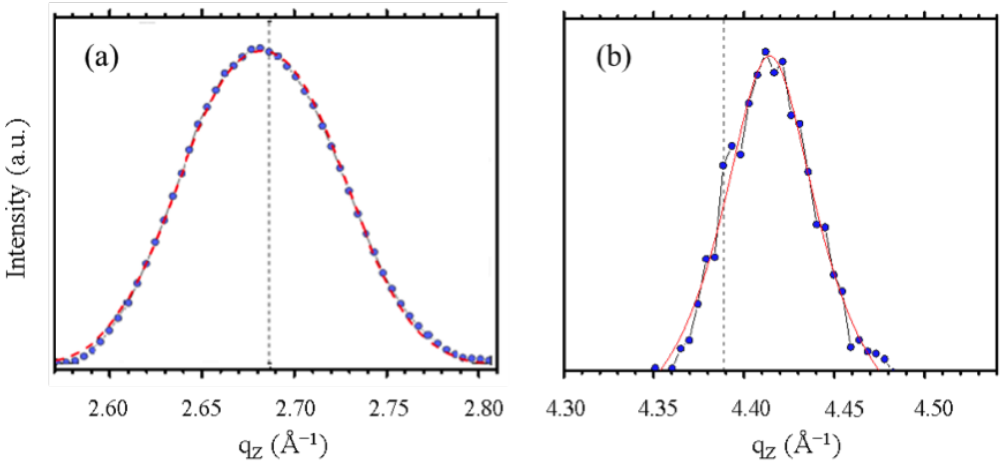

Figure 3.4. $\theta - 2\theta$ scan of (a) Al(111) reflection from sample S3 and, (b) Al(220) reflection from S5. Dashed vertical lines are peak positions for a strain-free Al (111) peak ($q_Z = 2.687\ ^{-1}$) in (a) and strain-free Al (220) peak ($q_Z = 4.388\ ^{-1}$) in (b). Red lines are fits to experimental data using a PseudoVoigt function. Shifts toward lower q_z indicate a normal tensile strain; Shifts toward higher q_z indicate a normal compressive strain.

Table 3.3 summarizes information collected from S3, S5, S6 and S7. This data includes in-plane lattice parameters, calculated from RSM data, for the topmost semiconductor layer, measured normal strains, and normal orientations. Assuming that Al layers are in a state of biaxial stress and that the in-plane strain components (ε_{xx}, ε_{yy}) in the Al metal are equivalent, the average in-plane strains are calculated from normal strain values, ε_{zz}, using the relation:

$$\varepsilon_{xx} = -(C_{11}/2C_{12})\varepsilon_{zz} \tag{3.5}$$

Values for in-plane strains in all samples obtained from Eq.3.5 and elastic constants, $C_{11} = 10.73 \times 10^{10}$ N/m^2 and $C_{12} = 6.08 \times 10^{10}$ N/m^2 [99], are listed in Table 3.3. Noteworthy from Table 3.3 is the change in strain state between (111) Al (in-plane compression) and (110) Al (in-plane tension) orientations that coincides with the transition of normal orientations.

Table 3.3. In-plane lattice parameters extracted from X-ray RSM, normal strain in aluminum layer, ε_{zz}, measured with symmetric X-ray scans, and in-plane Al strain, ε_{xx}, deduced from normal strains.

Sample	Sm Latt. Param. (Å)	Al strain, ε_{zz}	Al strain, ε_{xx}	Al growth orientation
S3	5.95 ± 0.01	0.0029 ±0.0003	-0.0025	(111)
S6	5.87 ± 0.01	0.0033 ± 0.0003	-0.0029	(111)
S5	6.10 ± 0.01	-0.0015 ± 0.0003	0.0013	(110)
S7	6.06 ± 0.01	-0.0058 ± 0.0003	0.0052	(110)

3.3.3 Discussion

To understand the reason of the lattice parameter dependence of the growth orientation, Figure 3.5 illustrates an isolated Al island growing on a semiconductor surface. According to the discussion in Section 1.2.4, four energy density terms describe the thermodynamic state of the island. γ_{int} represents the energy density of the interface between the semiconductor and aluminum, and γ_{surf} represents the energy density of the top surface of the Al grain. The side facets (sf) of the grain have a generic energy density denoted by γ_{sf} (which becomes the grain boundary energy after coalescence). The energy resulting from each of these terms is area dependent. A fourth energy density, σ_{str}, is from strain within the grain and its energy is volume dependent.

Multiplying each energy density by area or volume and summing terms gives a total energy expression,

$$E_{\text{tot}} = \gamma_{\text{surf}} A_{\text{surf}} + \gamma_{\text{int}} A_{\text{int}} + \gamma_{\text{sf}} A_{\text{sf}} + \sigma_{\text{str}} V_{\text{st}}. \tag{3.6}$$

Equation 3.6 does not imply Al growth is an equilibrium process, but the equation provides a means of incorporating parameters that are lattice-parameter dependent into this

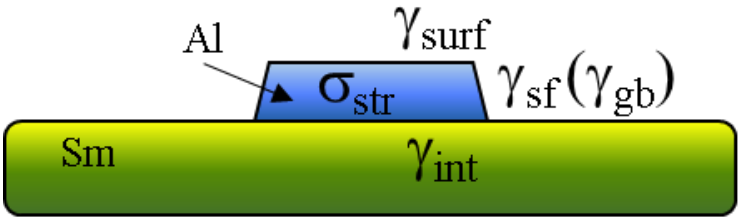

Figure 3.5. A schematic illustration of a growing Al island on a semiconductor (Sm) surface. The figure identifies four energy density terms: Surface (γ_{surf}), interfacial (γ_{int}), side facet (γ_{sf}), and strain (σ_{str}).

analysis. Specifically, strain energy and interfacial energy depend on lattice parameter. Before detailed discussion on the lattice parameter dependence of strain and interfacial energy, the effect of other terms in equation 3.6 can be considered. The shape of the island, or nucleus, in Fig 3.5 is significant. Measurements of grain size in both Al(111) and Al(110) (the measurements is be presented in Chapter 4) show that Al grain diameters are five times greater than layer thickness. A large diameter-to-thickness ratio suggests the true nucleus shape has a flat surface, as depicted in the figure, rather than a lenticular shape. The top surface is assumed to be a high-symmetry, low-energy plane, and this assumption plays a role in the analysis to follow.

The surface energy density term in Eq 3.6 is constant. It is widely accepted that in face-centered cubic (FCC) metals, (111) lattice planes have the lowest surface energy compared to all other planes. For FCC aluminum, reported surface energy density values are 0.044 eV/Å^2 for (111) and 0.057 eV/Å^2 for (110) planes [53]. These values imply that (111) normal orientation would always be favored over (110) in the absence of other counterbalancing factors.

Other process parameters, such as growth rate and growth temperature, may cause the boundary between (111) and (110) orientated aluminum to shift in lattice parameter by altering kinetic processes, but they themselves do not depend on lattice parameter and are not considered further.

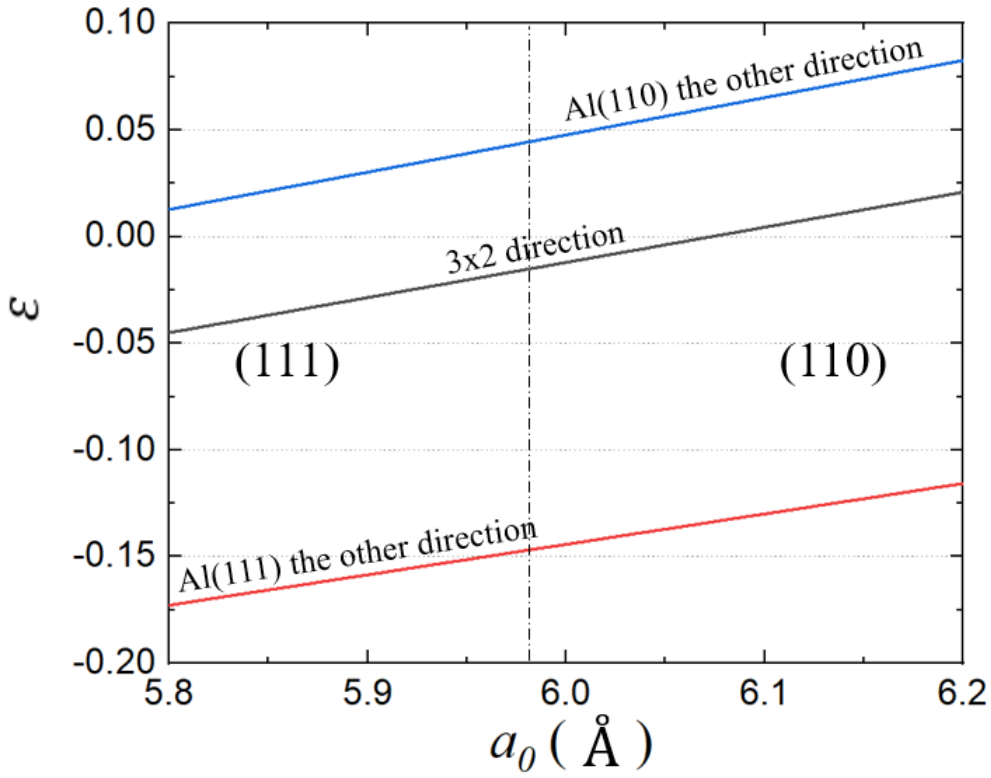

Figure 3.6. The lattice parameter dependence of lattice mismatch between semiconductor and Al(111) and Al(110) films. The black line plots the lattice mismatch on the 3×2 direction (for Al(111) the direction is Al[1$\bar{1}$0] ‖ Sm[1$\bar{1}$0], while for Al(110) the direction is Al[1$\bar{1}$0] ‖ Sm[110]). The blue line plots the mismatch in other direction of Al(111). The red line plots the mismatch in other direction of Al(110).

Figure 3.6 plots the lattice parameter dependence of the lattice mismatch values between semiconductor surface and aluminum film in different orientations. Although there is preferred growth orientations (in most cases, either (111) or (110)) for each semiconductor surface lattice parameter a_0, this plot calculates the lattice mismatch of both (111) and (110) for each a_0. For both Al(111) and Al(110) orientations observed, there is a 3×2 "domain matching" direction (see Section 1.2), on which the length of 3 aluminum surface units equals

to the length of 2 semiconductor surface units. For Al(111) it is Al[$1\bar{1}0$] ∥ Sm[$1\bar{1}0$]. The lattice mismatch between aluminum and semiconductor in this direction is:

$$\begin{aligned}\varepsilon_{3\times2(111)} &= \frac{2a_{\mathrm{Sm}[1\bar{1}0]}/3 - a_{\mathrm{Al}[1\bar{1}0]}}{a_{\mathrm{Al}[1\bar{1}0]}} \\ &= \frac{\sqrt{2}a_0/3 - 2.863\ \text{Å}}{2.863\ \text{Å}}.\end{aligned} \tag{3.7}$$

For Al(110) it is Al[$1\bar{1}0$] ∥ Sm[110]. The lattice mismatch between aluminum and semiconductor in this direction is:

$$\begin{aligned}\varepsilon_{3\times2(110)} &= \frac{2a_{\mathrm{Sm}[110]}/3 - a_{\mathrm{Al}[1\bar{1}0]}}{a_{\mathrm{Al}[1\bar{1}0]}} \\ &= \frac{\sqrt{2}a_0/3 - 2.863\ \text{Å}}{2.863\ \text{Å}}.\end{aligned} \tag{3.8}$$

Therefore, the lattice mismatch in the 3×2 direction of Al(111) and lattice mismatch in the 3×2 direction of Al(110) are equal. The black line in Figure 3.6 plots the lattice mismatch in these directions. The blue and red line plot the lattice mismatch in the other direction that is not 3×2, for Al(111) and Al(110), respectively. To be specific, the red line plots the lattice mismatch between Al(111) and semiconductor in the direction Al[$11\bar{2}$] ∥ Sm[110], expressed as:

$$\begin{aligned}\varepsilon_{(111)} &= \frac{a_{\mathrm{Sm}[110]} - a_{\mathrm{Al}[11\bar{2}]}}{a_{\mathrm{Al}[11\bar{2}]}} \\ &= \frac{a_0/\sqrt{2} - 4.958\ \text{Å}}{4.958\ \text{Å}}.\end{aligned} \tag{3.9}$$

The blue line plots the lattice mismatch between Al(110) and semiconductor in the direction Al[001] ∥ Sm[$1\bar{1}0$], expressed as:

$$\begin{aligned}\varepsilon_{(110)} &= \frac{a_{\mathrm{Sm}[1\bar{1}0]} - a_{\mathrm{Al}[001]}}{a_{\mathrm{Al}[001]}} \\ &= \frac{a_0/\sqrt{2} - 4.050\ \text{Å}}{4.050\ \text{Å}}.\end{aligned} \tag{3.10}$$

For both Al(111) and Al(110), the direction that is not 3×2 leads to higher mismatch. It is noteworthy that for Al(111) the mismatch is compressive (aluminum needs to be compressed to match the semiconductor) while for Al(110) the mismatch is tensile (aluminum needs to be stretched to match the semiconductor). This explains the change in strain state between Al(111) and Al(110) films.

However, the values of the residual strain in Table 3.3 are much smaller than the calculated lattice mismatch. This suggests that the aluminum films are not coherently strained on the semiconductor. The strain energy can be calculated using the following equation [19], [100]:

$$\begin{aligned} E_{\text{str}} &= \sigma_{\text{str}} V_{\text{st}} \\ &= \frac{S}{(1-\nu)}(\varepsilon_1^2 + \varepsilon_2^2 + 2\nu\varepsilon_1\varepsilon_2) h A_{\text{surf}}, \end{aligned} \tag{3.11}$$

where $S = 25.5$ GPa is the shear modulus and $\nu = 0.32$ is the Poisson ratio of aluminum [25], ε_1 and ε_2 are the residual strain in two perpendicular directions, and h is the thickness of the aluminum film. Given $h = 10$ nm and taken in the maximum residual strain values in Table 3.3, $\varepsilon_1 = \varepsilon_2 = 0.5\%$, this equation can be calculated as $E_{\text{str}}/A_{\text{surf}} = 0.0016$ eV/Å^2. This result is much smaller than the surface energy densities, 0.044 eV/Å^2 and 0.057 eV/Å^2.

The cost of low residual strain in the aluminum films is the interfacial energy caused by unregistered atoms on the interface. Figure 3.7 presents two cross-sectional images of a semiconductor/Al interface: Figure 3.7(a) for (110) and Figure 3.7b for (111). For each image, the zone-axis is along the 3×2 direction (for Al(111) it is Sm[1$\bar{1}$0] and for Al(110) it is Sm[110]) so the interface in the image shows the direction that is not 3×2. Green lines in the figure identify traces of (1$\bar{1}$1) planes in the semiconductor lattice. Red lines coincide with traces of (11$\bar{1}$) planes in aluminum. In Figure 3.7(a), there is continuity of the {111} planes across the semiconductor/superconductor interface. This registry at the interface indicates the interfacial energy is low. A different situation appears in Figure 3.7(b), where there is a mismatch in lattice registry. Some lattice planes in Al (red lines) terminate at the interface and form dislocations, which increase the energy of the Al-Sm interface.

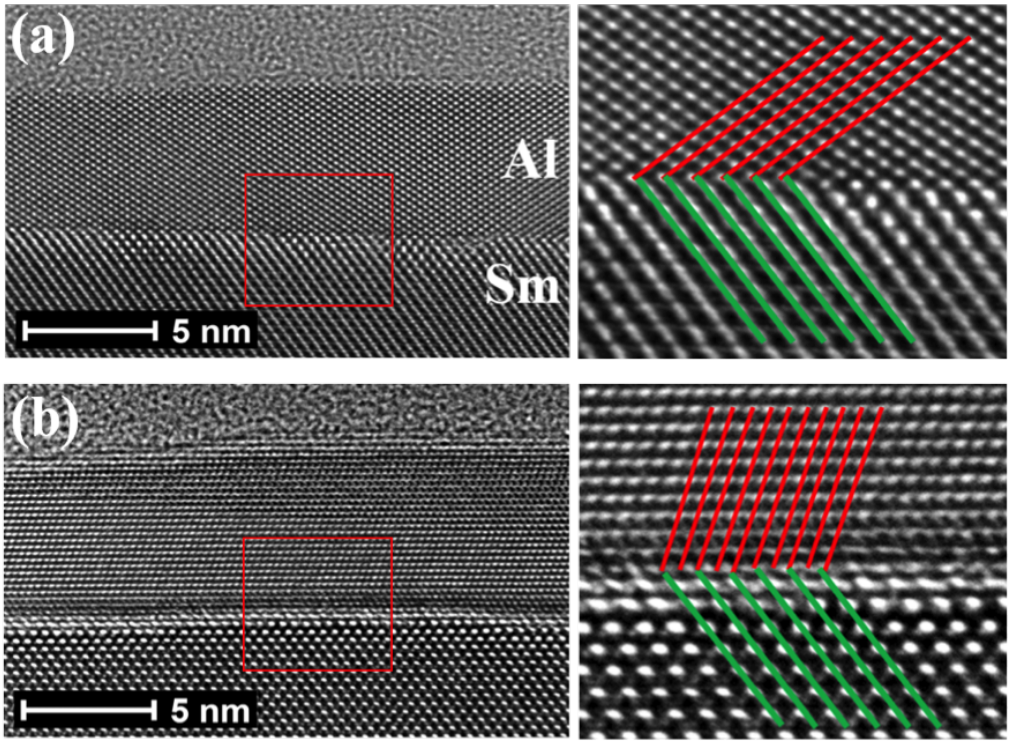

Figure 3.7. Cross-sectional HRTEM images of Al/Sm interfaces having Al normal orientations of (a) (110) and (b) (111) both from S2. The interface area in the red boxes are enlarged to show the details of atom registry. Green lines highlight traces of $(1\bar{1}1)$ planes in the semiconductor. Red lines highlight traces of $(11\bar{1})$ planes in aluminum. In (a), there is one-to-one registry of semiconductor and Al planes. In (b), not all red lines continue into the semiconductor along green traces. This mismatch produces lattice planes that terminate at the interface, increasing the interfacial energy.

The existence of these unregistered atoms provides an estimation of the difference in the interfacial energy between (111) and (110) films. Consider an aluminum surface with surface energy density γ_{surf} and a semiconductor (001) surface with surface energy density γ_{sub}. γ_{surf} is mainly contributed by the unfilled positions of neighboring atoms. Consider only the nearest neighbor. For Al(111) surface, each atom on the surface has 3 unfilled neighboring positions. For Al(110) surface, each atom in the first layer has 5 unfilled neighboring positions and each atom in the second layer has 1 unfilled neighboring position (shown in Figure 3.8). For semiconductor, γ_{sub} is mainly contributed by the dangling bonds on the surface. Now, putting these two surfaces together to make an Al/Sm interface causes a decreasing of the

total energy. The density of the decreased energy is denoted as γ_{d}, which is contributed by the atomic registry that fills the unfilled neighboring positions of Al atoms and satisfies the dangling bonds of Sm atoms. Obviously, the interfacial energy, γ_{int} can be calculated as [54]:

$$\gamma_{\mathrm{int}} = \gamma_{\mathrm{surf}} + \gamma_{\mathrm{sub}} - \gamma_{\mathrm{d}}. \tag{3.12}$$

Based on the atomic registry condition observed, assume all dangling bonds of Sm atoms are satisfied. For Al(111)/Sm interface, only half of the surface Al atoms are in good registry condition. Therefore, the interfacial energy can be estimated as

$$\gamma_{\mathrm{int}(111)} = \frac{1}{2}\gamma_{\mathrm{surf}(111)} = 0.022 \text{ eV/Å}^2. \tag{3.13}$$

For Al(110)/Sm interface, all Al atoms at the first layer above the interface are in good registry condition. Therefore, the interfacial energy is contributed by the 1 unfilled neighboring position of the Al atoms in the second layer above the interface, which is estimated as

$$\gamma_{\mathrm{int}(110)} = \frac{1}{1+5}\gamma_{\mathrm{surf}(110)} = 0.010 \text{ eV/Å}^2. \tag{3.14}$$

Given the estimation above, in equation 3.6, the sum of the surface energy term and the interfacial energy term is calculated as

$$\begin{aligned}(E_{\mathrm{surf}} + E_{\mathrm{int}})_{(111)} &= \gamma_{\mathrm{surf}}A_{\mathrm{surf}} + \gamma_{\mathrm{int}}A_{\mathrm{int}} \\ &= (\gamma_{\mathrm{surf}} + \gamma_{\mathrm{int}})_{(111)}A_{\mathrm{surf}} \\ &= 0.066 \text{ eV/Å}^2 \cdot A_{\mathrm{surf}}.\end{aligned} \tag{3.15}$$

and

$$\begin{aligned}(E_{\mathrm{surf}} + E_{\mathrm{int}})_{(110)} &= \gamma_{\mathrm{surf}}A_{\mathrm{surf}} + \gamma_{\mathrm{int}}A_{\mathrm{int}} \\ &= (\gamma_{\mathrm{surf}} + \gamma_{\mathrm{int}})_{(110)}A_{\mathrm{surf}} \\ &= 0.067 \text{ eV/Å}^2 \cdot A_{\mathrm{surf}}.\end{aligned} \tag{3.16}$$

The second the step of the two calculations above dismissed the difference between the area of top surface and interface.

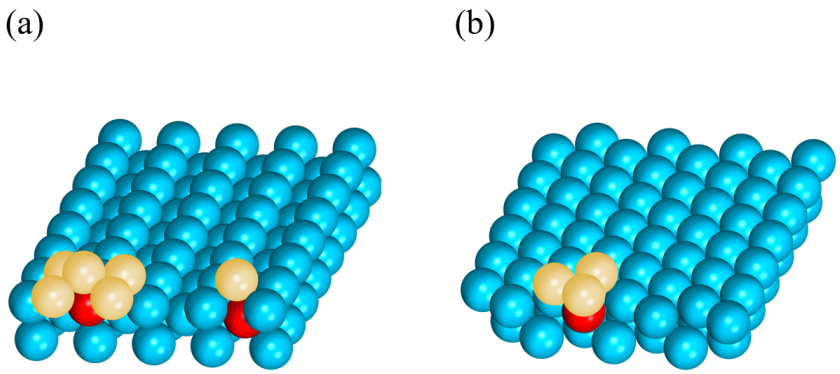

Figure 3.8. The unfilled nearest neighboring positions of Al atoms on Al(110) (a) and Al(111) (b) surface. For each atom in the first layer of Al(110) surface (the red atom on the left-hand side of (a)), there are 5 unfilled neighboring positions (marked by light yellow). For each atom in the second layer of Al(110) surface (the red atom on the right-hand side of (a)), there is 1 unfilled neighboring position (marked by light yellow). For each atom in the first layer of Al(111) surface (the red atom in (b)), there are 3 nearest neighboring positions (marked by light yellow).

Although equation 3.15 and 3.16 are just estimations, they indicate how close the energy terms of (111) and (110) are. A small perturbation can change the preference of growth orientation from one to another. The perturbation in strain energy term and interfacial energy term caused by the change of lattice parameter can be the reason of transition. Precise calculations of the energy terms in equation 3.6 is an interesting research topic in future theoretical works, but it is beyond the scope of this thesis.

4. GRAIN PROPERTIES OF THE ALUMINUM FILMS

In Chapter 3, the growth orientation of the aluminum films was studied. The experimental results showed that most aluminum films grown in this thesis have one unique growth orientation, either (111) or (110). The growth orientation of the aluminum films strongly depends on the lattice parameter of the semiconductor surface on which the aluminum film is deposited. Films with (111) orientation grow on surface with lattice constant smaller than 5.98 , while films with (110) orientation grow on surface with lattice constant bigger than 5.98 . Only one sample was observed to have aluminum film with both (111) and (110) orientations. The semiconductor lattice constant of this sample is in between the range of the (111) and (110) samples.

This chapter is dedicated to the study of the in-plane orientation of the aluminum film. For aluminum films with unique growth orientations (either (111) or (110)), a follow-up question is whether the film is single-crystal. (We know that aluminum films with mixed growth orientations are not single-crystal.) If the film is not single-crystal, what is the average grain size of the grains? What is the in-plane orientation of each grain? These are questions that remain to be answered. The orientation and size of the grains can be related to the interaction across the epitaxial interface and the mechanism of aluminum growth.

If the aluminum film has a unique growth orientation but does not have a unique in-plane orientation, the film is called to have a "textural" orientation [101], [102]. If the aluminum film has both a unique growth orientation and a unique in-plane orientations, in some context, the growth is called "epitaxy" [102]. In this chapter, the grain properties and in-plane orientations of the grains for (111) and (110) aluminum films are discussed. One will see the (111) films have a more "textural" orientation. Although not randomly distributed, in-plane rotation between grains can be observed. On the other hand, the (110) films are less textural, in which little in-plane rotation can be observed.

4.1 Grain properties of Al(111)

4.1.1 Cross-sectional TEM imaging and twin grains

Cross-sectional TEM imaging of Al(111)

One way to directly see the grain properties of the film is through cross-sectional imaging. In Chapter 3, Figure 3.2 showed a high-resolution TEM image of the aluminum film in sample S1 to explain the characterization of (111) growth orientation. During the experiment, an image with lower magnification was also taken to analyze further in a larger area (Figure 4.1(a)).

In the image, the aluminum film is divided into 4 grains by three grain boundaries, numbered as 1, 2, and 3 in Figure 4.1(a). The grains are labelled as A, B, C, and D. Figure 4.1(b) and (c) show higher magnification images around grain boundary 1 and 2, 3, respectively. The FFT patterns of the four grains are presented in Figure 4.1(d). To be clear, some of these "grains" may actually belong to one large grain since this is a cross-section sample. Here they are treated as four different grains.

The FFT patterns are able to tell the in-plane crystal alignment. Note area A, B, and D are able to show images with atomic resolution and well-defined FFT patterns because the specific crystallographic directions of the aluminum crystal is well aligned with the incident electron beam (called "on zone-axis" or "on-axis"). The zone-axis of the images can be directed calculated from the indices in the FFT patterns. For grain A, the aluminum crystallographic direction pointing into the page can be calculated as $[002] \times [111] = [\bar{2}20]$. For grain B and D, it is $[111] \times [002] = [2\bar{2}0]$. The sign of the vector product follows the right-hand rule. (Here the calculation depends on how the signs of the indices are defined. However, by defining the normal direction as [111], the calculated zone-axis has unique indices.) Grain C does not show either atomic resolution or a clear FFT pattern because the crystal is not exactly on-axis. Keep in mind that the sample was tilted so that the semiconductor $[1\bar{1}0]$ direction is aligned with the incident beam. So, the zone-axis of the whole image is also Sm$[1\bar{1}0]$. Therefore, for grain A, both Al$[\bar{1}10]$ and Sm$[1\bar{1}0]$ point into the page. So

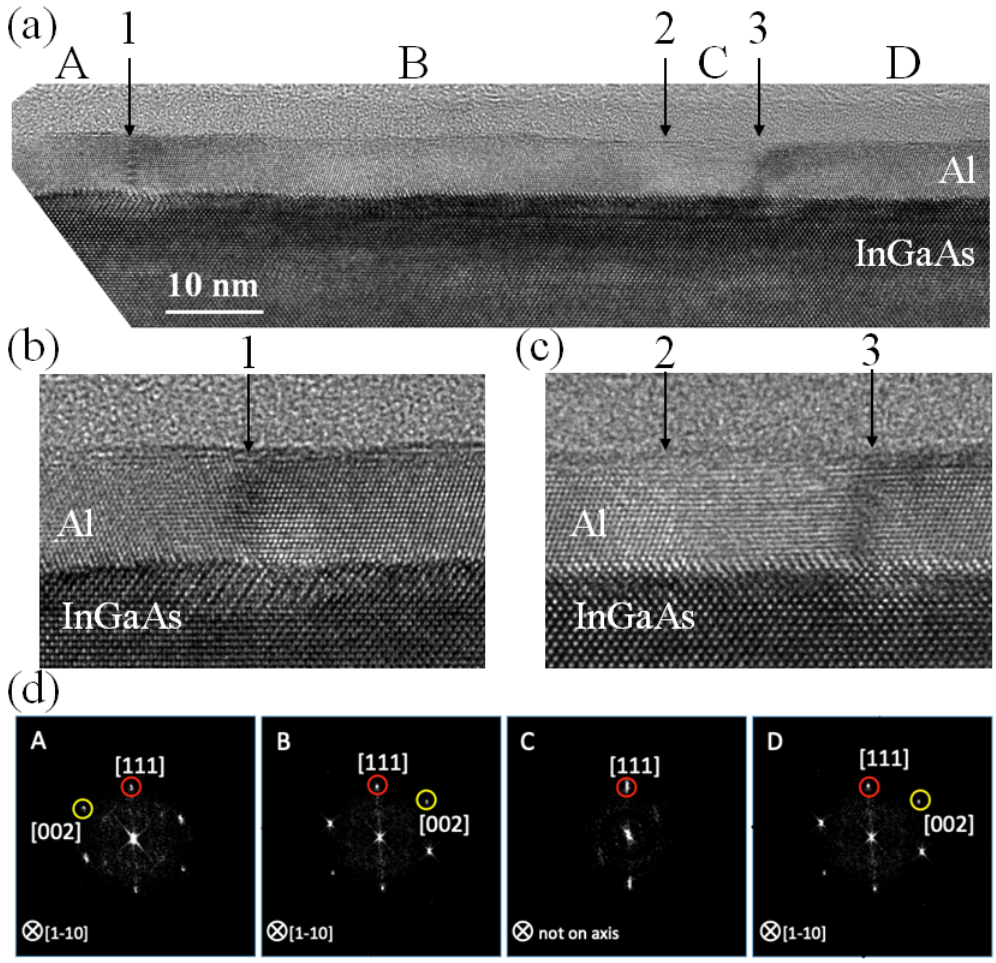

Figure 4.1. A grain boundary analysis based on HRTEM images in S1 with (111) growth orientation. (a) shows a cross-sectional HRTEM image of the sample in a 100 nm wide region. Three grain boundaries are characterized in the image, marked as 1, 2 and 3, which divide the region into four grains A, B, C and D. (b) shows a higher magnification image of grain boundary 1. (c) shows a higher magnification image of grain boundary 2 and 3 together. (d) shows the FFT of the four grains A, B, C and D, respectively. All FFTs show a same growth orientation (111). Among them, (d)-B and (d)-D are identical. 1 is a twin boundary since (d)-A and (d)-B are mirror reflections to each other. (d)-C doesn't show an on-axis pattern.

the crystal alignment is Al(111)[$\bar{1}$10] ∥ Sm(001)[1$\bar{1}$0]. For grain B and D, it is Al(111)[1$\bar{1}$0] ∥ Sm(001)[1$\bar{1}$0]. The orientation of grain C cannot be extracted using the information in the image.

Note there is only a "−" sign difference between the crystal alignment of A and B, D,

which indicates that grain A is 180° rotated from grain B and D. The boundary between A and B (the grain boundary 1 in Figure 4.1) is called a "twin boundary". The relationship between grain A and B can be told not only by the FFT patterns, but also directly by the image. Figure 4.2 draws the atomic arrangement near the boundary 1. The unit cell of the aluminum crystal on each side of the boundary is marked by black dashed lines. One can see the 180° rotation immediately from the orientation of the unit cells.

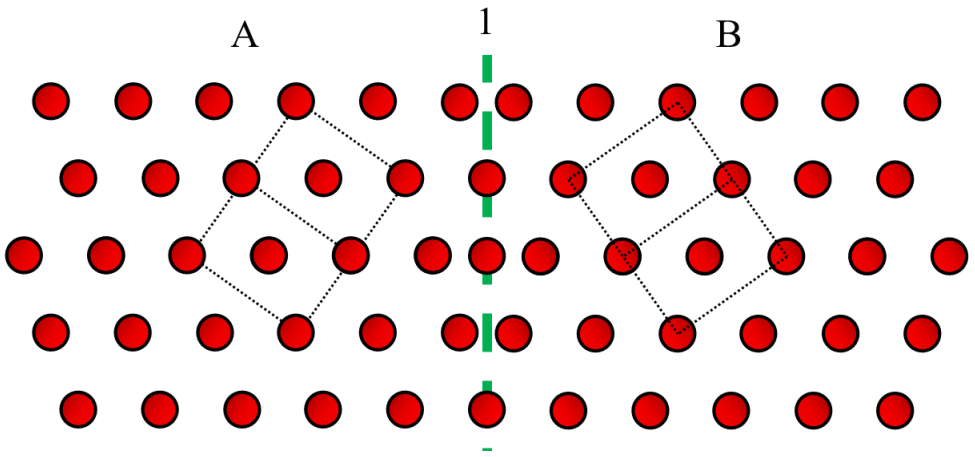

Figure 4.2. The atomic arrangement near the twin boundary 1 in Figure 4.1. The black dashed lines marked out the unit cell of the aluminum crystal on each side of the boundary.

Orientation degeneracy in Al(111) grains

The existence of grains that are 180° rotated from each other is commonly observed in the cross-sectional TEM imaging of all (111) aluminum films in this thesis, including the (111) grains in the aluminum film with mixed growth orientations.

One can also treat the two grains that are 180° rotated from each other as stacking difference, shown in Figure 4.3. The left-hand side of Figure 4.3 presents a single atomic layer of the aluminum crystal with (111) growth orientation. Only seven aluminum atoms are drawn here, which is enough to present the concept. There are two different ways to stack a second atomic layer of aluminum onto the first one: to sit atoms on positions like α-γ-ε...,

or to sit atoms on positions like β-δ-σ.... The resulting crystal becomes the two types on the right-hand side of Figure 4.3, which are 180° rotated from each other.

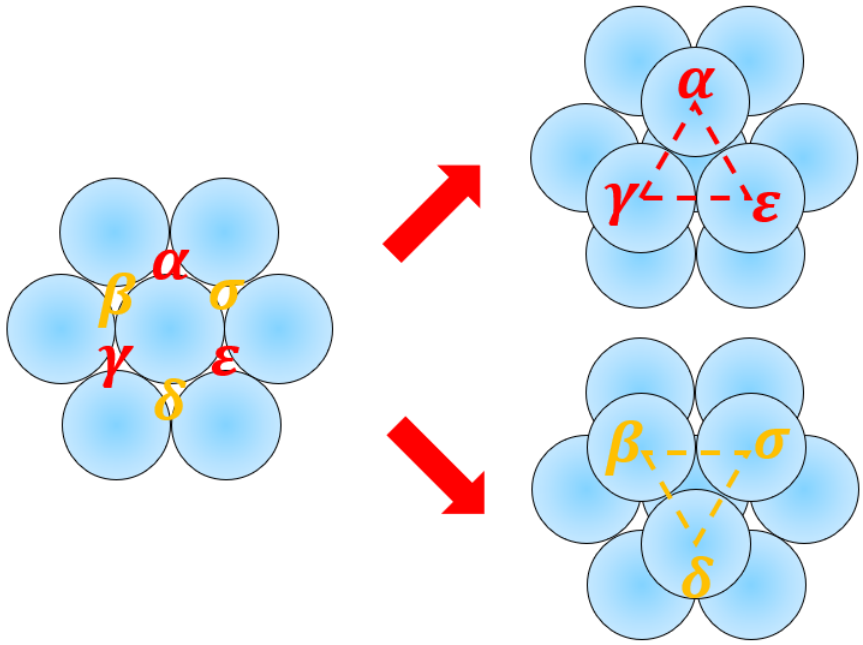

Figure 4.3. The 180° rotated Al(111) crystal can be treated as stacking difference. On one atomic layer of aluminum (111) crystal, there are two ways to stack a second atomic layer: stacking atoms on positions like α-γ-ε... or stacking atoms on positions like β-δ-σ.... The resulting aluminum crystals are 180° rotated from each other.

The interaction between the aluminum grains and the semiconductor surface can also be considered. In a first order approximation, the reconstruction of the semiconductor surface is not considered. In this case, the semiconductor surface has reflection symmetry. As a result, the epitaxial interface between the semiconductor and an Al(111) grain A is completely identical with the epitaxial interface between the semiconductor and the grain that is 180° rotated from A. The interfacial energy of the grains that are 180° rotated from each other should be identical. The two different epitaxial orientations, Al(111)$[1\bar{1}0]$ ∥ Sm(001)$[1\bar{1}0]$ (denoted as Y) and Al(111)$[\bar{1}10]$ ∥ Sm(001)$[1\bar{1}0]$ (denoted as Y'), share the same interfacial energy (energetically degenerated). This degeneracy causes the co-existence of the grains that take

Y and Y' orientations, which is an important source of the grain boundaries in Al(111) films.

The limits of cross-sectional TEM

This section characterized the grain properties of the Al(111) film by cross-sectional TEM imaging and showed the co-existence of 180° rotated grains. However, cross-sectional TEM has its limit on analyzing the grain properties. In order to get accurate crystallographic information, the crystal needs to be on-axis with respect to the electron beam. The analysis in this section does not mention the angle of rotation for grain C (Figure 4.1) because the crystal is not on-axis. Also, looking at Figure 4.1(b), one can notice that there are some focusing difference between grain A and B, and even between left and right part of grain A. This implies that A and B also have a low angle rotation from the on-axis orientation. Cross-sectional imaging is limited on extracting this kind of microstructural information. For an aluminum film with a particular growth orientation, plan view imaging might be one of the best technique to understand the crystal orientation, since a big portion of the film is on-axis (the electron beam is parallel to the growth orientation for the entire film). In section 4.1.2, a plan view TEM analysis of Al(111) film will be presented.

4.1.2 Plan view TEM imaging of Al(111)

As was discussed at the end of Section 4.1.1, one ideal way to characterize aluminum films is to perform plan view TEM imaging. However, the sample preparation for plan view imaging is complex. Since the thickness of the aluminum film is less than 10 nm, the film cannot stand alone unless the sample preparation process is extremely careful. Normally, there will be residual semiconductor layers under the aluminum film. As was discussed in Section 2.2, dark-field imaging is necessary to distinguish the aluminum film from the semiconductor layers. In this section, sample S3 introduced in Chapter 3 is used for the plan view analysis of aluminum film with only (111) growth orientation. The diffraction pattern

of the sample will be discussed first, followed by dark-field imaging.

Diffraction pattern

Figure 4.4 shows the diffraction pattern of the plan view sample. Some details about the orientation of the sample must be explained. During the sample preparation process, the direction of the wafer was noted so one can tell which direction is Sm[$1\bar{1}0$] and which direction is Sm[110] when the sample was put into the microscope. In the microscope, the sample was tilted according to the Kikuchi lines in the diffraction pattern of the semiconductor layers to find the correct zone axis [93].

Three types of reflections are observed in Figure 4.4. Reflections from the semiconductor crystallographic planes are well-defined round spots. Two of them are circled with yellow color and labeled according to the previously noted wafer orientation.

Reflections from the aluminum film are marked with red circles. They form a hexagonal pattern expected from an FCC crystal with $\langle 111 \rangle$ zone-axis. Note the diffraction pattern of aluminum crystal with Al(111)[$1\bar{1}0$] $\parallel$ Sm(001)[$1\bar{1}0$] (Y) orientation and Al(111)[$\bar{1}10$] $\parallel$ Sm(001)[$1\bar{1}0$] (Y') orientation are identical. The indices marked in Figure 4.4 is for Y orientation. For Y' orientation, a negative sign should be added.

The reflections of the aluminum crystal are spots distributed on short arcs. This implies the aluminum grains are not strictly oriented as Y or Y'. There can be low-angle in-plane rotations from Y and Y'. This is the most important microstructural information obtained from the plan view diffraction pattern, which was not possible to acquire by cross-sectional TEM. In Figure 4.4, the range of the rotation angle is measured (the angle marked by grey dashed lines) to be from -8° to 8°.

Reflections of the beam that were diffracted by both aluminum film and semiconductor layers are also observed in the diffraction pattern in Figure 4.4. The g-vector of these double-diffracted beams can be determined by Bragg's law. According to Bragg's law, when

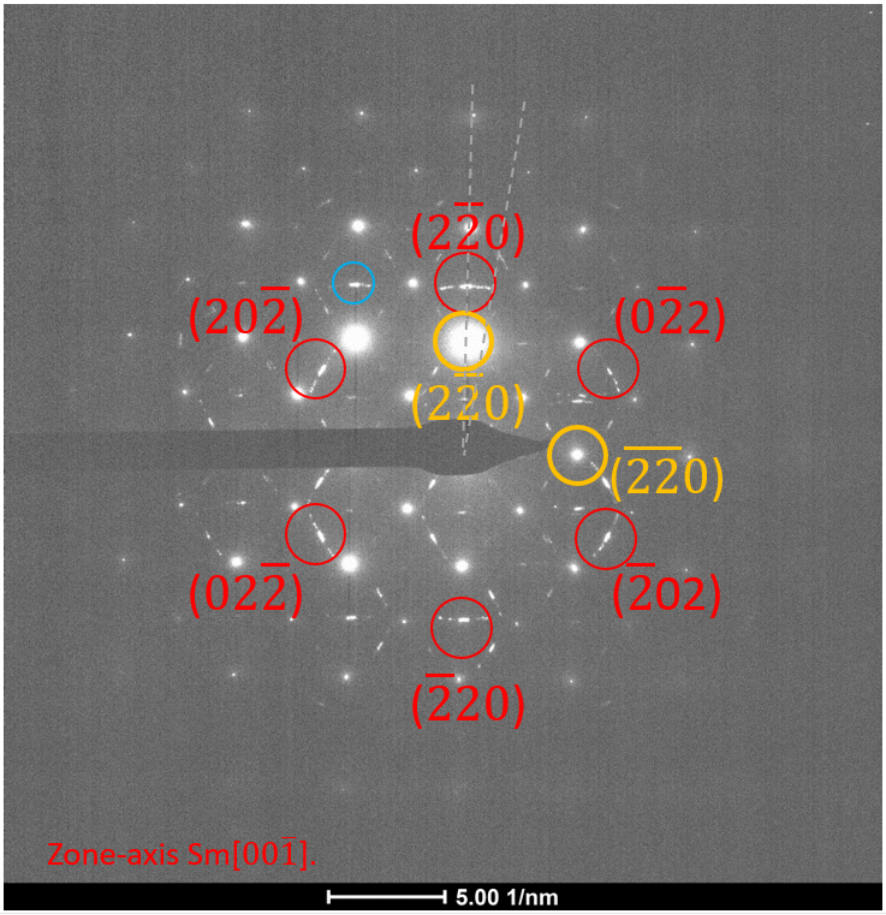

Figure 4.4. The diffraction pattern of a plan view sample of Al(111) film made in sample S3. The zone-axis is Sm[00$\bar{1}$]. The reflections of the aluminum film and semiconductor layers are marked out by red and orange circle, respectively. The blue circle marks a reflection of an electron beam first diffracted by aluminum film and then diffracted by semiconductor.

an incident electron beam with wave vector $\mathbf{k}_0$ is diffracted by a set of atomic planes in the crystal with a g-vector $\mathbf{g}_1$, the wave vector of the diffracted beam is

$$\mathbf{k}_1 = \mathbf{k}_0 + \mathbf{g}_1. \tag{4.1}$$

Then, if this diffracted beam is diffracted again by another set of atomic planes with a g-vector $\mathbf{g}_2$, the wave vector of the double-diffracted beam is

$$\mathbf{k}_2 = \mathbf{k}_1 + \mathbf{g}_2 = \mathbf{k}_0 + \mathbf{g}_1 + \mathbf{g}_2. \tag{4.2}$$

Therefore, the g-vector of the double-diffracted beam is the vector resultant of the two g-vectors that caused the diffraction, written as

$$\mathbf{g}_{\text{dd}} = \mathbf{g}_1 + \mathbf{g}_2. \tag{4.3}$$

The blue circle in Figure 4.4 marks an example of the double-diffracted beam. The marked beam was diffracted by Al($2\bar{2}0$) planes and Sm(220) planes. Figure 4.5 shows the geometric relationship between the g-vectors.

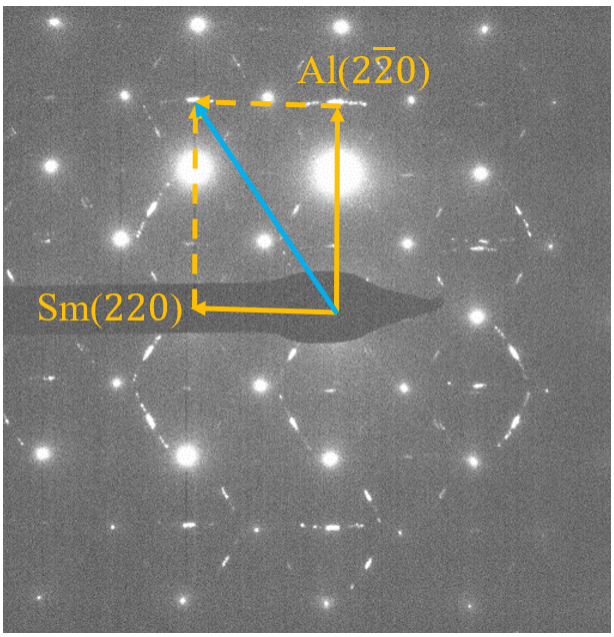

Figure 4.5. The g-vector of the double-diffraction beam marked by blue circle in Figure 4.4 is the vector resultant of the g-vectors of Al($2\bar{2}0$) and Sm(220).

Given equation 4.3, a double-diffracted reflection in the diffraction pattern can be treated as an aluminum reflection translated by a g-vector of the semiconductor. Therefore, consider the following operations. First extract the position of all semiconductor reflections (marked by red circles in Figure 4.6 (a)). And then, center the extracted pattern at a single-diffracted aluminum reflection, for example, Al($2\bar{2}0$). The new pattern is drawn by red circles in Figure 4.6 (b). After these operations, the new pattern marks out all reflections that are once

diffracted by Al($2\bar{2}0$) planes.

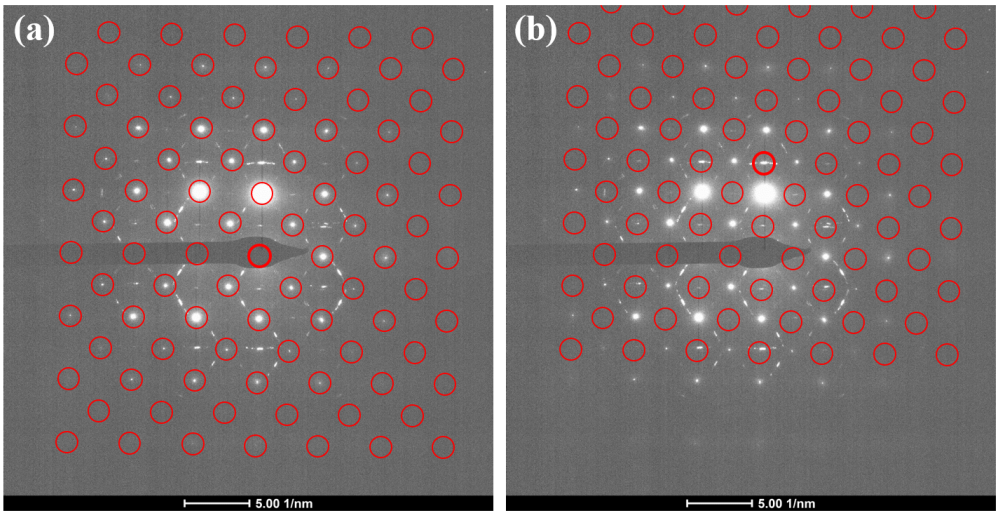

Figure 4.6. (a) red circles mark out the position of all semiconductor reflections. The position of the transmitted beam is marked with a thicker circle. (b) the pattern in (a) is centered at single-diffracted Al($2\bar{2}0$) reflection. The resulting pattern marks out all reflections that are diffracted by Al($2\bar{2}0$) and a set of planes in semiconductor layers.

The operations above are able to mark out all reflections in the diffraction pattern by centering the pattern in Figure 4.6 (a) at all six aluminum reflections. Different colors are used, shown in Figure 4.7. Although the pattern is very complex, there are two main characteristics. First, the semiconductor reflections are not in any circle with any color. Second, each circle is overlapped with one and only one circle with a certain color. Red circles are always overlapped with green circles. Orange circles are always overlapped with blue circles. Yellow circles are always overlapped with grey circles.

Each circle in Figure 4.7 indicates the position of a double-diffracted reflection in the diffraction pattern (the six thick circles indicate the positions of the single-diffracted aluminum reflections). The fact that each circle is overlapped with another circle implies that

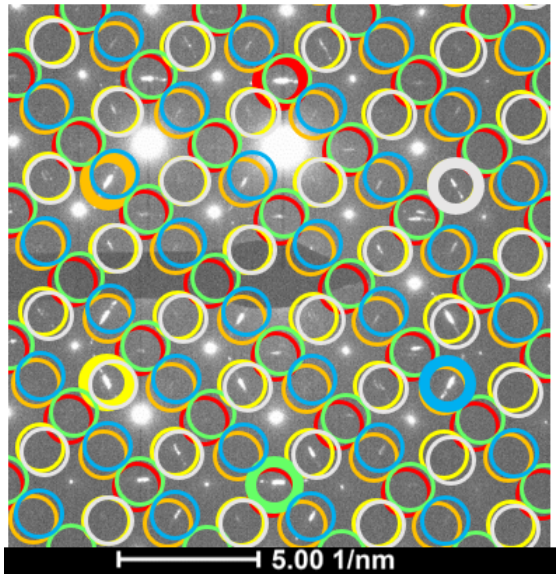

Figure 4.7. All double-diffracted reflections can be obtained by translating semiconductor DP with different Al g-vectors. This pattern is made by centering the pattern in Figure 4.6 (a) at all six aluminum reflections. Different colors are used to mark the pattern centered at different reflections. Red for the pattern centered at Al($2\bar{2}0$). Orange for the pattern centered at Al($20\bar{2}$). Yellow for the pattern centered at Al($02\bar{2}$). Green for the pattern centered at Al($\bar{2}20$). Blue for the pattern centered at Al($\bar{2}02$). Grey for the pattern centered at Al($0\bar{2}2$). Only the area near the center of the diffraction pattern image is shown.

for each reflection there is another reflection very close to it. For instance, consider the single-diffracted Al($2\bar{2}0$) reflection (the thick red circle). There is a green circle overlapping with it. The g-vector of the reflection represented by the green circle is denoted as $\mathbf{g}_{\mathrm{dd}}$. It is easy to obtain from the image that

$$\mathbf{g}_{\mathrm{dd}} = \mathbf{g}_{\mathrm{Al}(\bar{2}20)} + \mathbf{g}_{\mathrm{Sm}(6\bar{6}0)}. \tag{4.4}$$

To calculate the distance between this double-diffracted reflection to the Al($2\bar{2}0$) reflection, take the vector subtraction:

$$\begin{aligned}\Delta\mathbf{g} &= \mathbf{g}_{\mathrm{Al}(2\bar{2}0)} - \mathbf{g}_{\mathrm{dd}} \\ &= \mathbf{g}_{\mathrm{Al}(2\bar{2}0)} - \mathbf{g}_{\mathrm{Al}(\bar{2}20)} - \mathbf{g}_{\mathrm{Sm}(6\bar{6}0)} \\ &= \mathbf{g}_{\mathrm{Al}(4\bar{4}0)} - \mathbf{g}_{\mathrm{Sm}(6\bar{6}0)}.\end{aligned} \tag{4.5}$$

The magnitude of this difference is

$$\begin{aligned}|\Delta\mathbf{g}| &= (|\mathbf{g}_{\mathrm{Al}(4\bar{4}0)}|^2 + |\mathbf{g}_{\mathrm{Sm}(6\bar{6}0)}|^2 - 2|\mathbf{g}_{\mathrm{Al}(4\bar{4}0)}||\mathbf{g}_{\mathrm{Sm}(6\bar{6}0)}|\cos\theta)^{\frac{1}{2}} \\ &= \frac{(d^2_{\mathrm{Al}(4\bar{4}0)} + d^2_{\mathrm{Sm}(6\bar{6}0)} - 2d_{\mathrm{Al}(4\bar{4}0)}d_{\mathrm{Sm}(6\bar{6}0)}\cos\theta)^{\frac{1}{2}}}{d_{\mathrm{Al}(4\bar{4}0)}d_{\mathrm{Sm}(6\bar{6}0)}},\end{aligned} \tag{4.6}$$

where d with certain subscription refers to the lattice spacing in that certain direction and θ is the rotation angle between Al[$1\bar{1}0$] and Sm[$1\bar{1}0$] directions. In perfect Al(111)[$1\bar{1}0$] $\|$ Sm(001)[$1\bar{1}0$] (Y) orientation, $\theta = 0°$. Equation 4.6 is calculated as

$$\Delta\mathbf{g} = \frac{|d_{\mathrm{Al}(4\bar{4}0)} - d_{\mathrm{Sm}(6\bar{6}0)}|}{d_{\mathrm{Al}(4\bar{4}0)}d_{\mathrm{Sm}(6\bar{6}0)}}. \tag{4.7}$$

Given

$$\begin{aligned}d_{\mathrm{Al}(4\bar{4}0)} &= \frac{a_{\mathrm{Al}}}{\sqrt{4^2+4^2+0^2}} \\ &= \frac{0.40495\ \mathrm{nm}}{4\sqrt{2}} \\ &= 0.0716\ \mathrm{nm}\end{aligned} \tag{4.8}$$

and

$$\begin{aligned}d_{\mathrm{Sm}(6\bar{6}0)} &= \frac{a_{\mathrm{Sm}}}{\sqrt{6^2+6^2+0^2}} \\ &= \frac{0.598\ \mathrm{nm}}{6\sqrt{2}} \\ &= 0.0705\ \mathrm{nm},\end{aligned} \tag{4.9}$$

the difference is calculated as $|\Delta \mathbf{g}| = 0.218$ 1/nm.

Since the reflections are so close to each other, they will be both included in the objective aperture during dark-field imaging. As will be shown in the next part, the interference of these reflections can create Moire patterns.

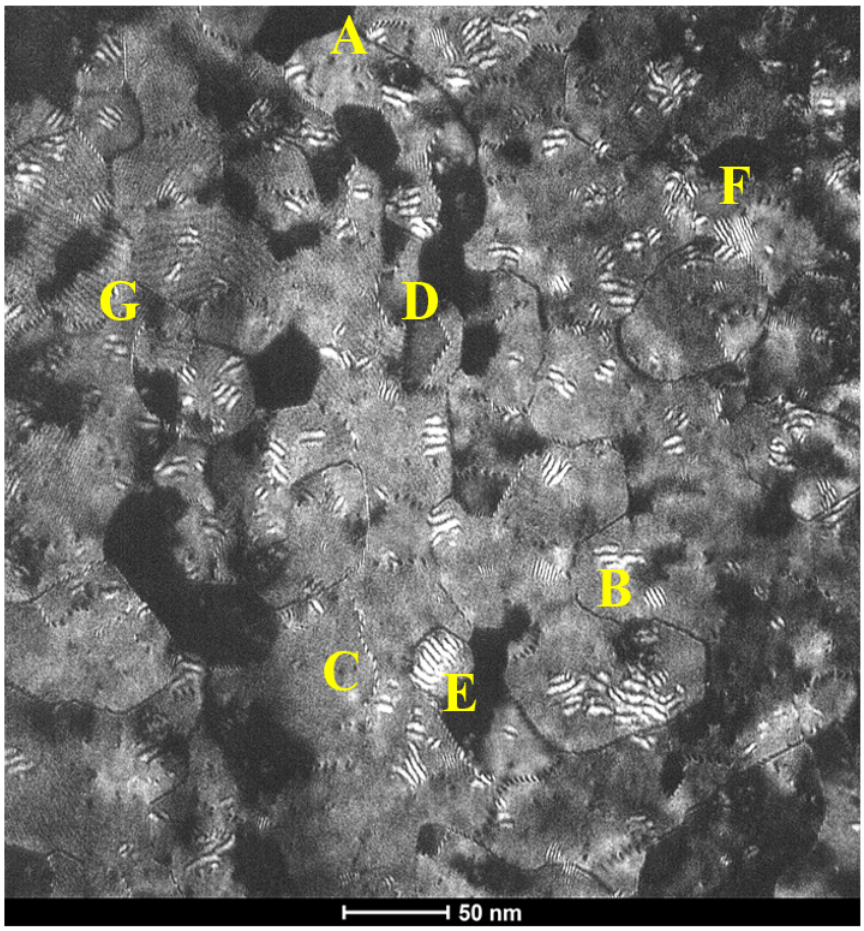

Figure 4.8. Dark-field TEM imaging of the plan view sample from S3. The aperture was used to pick up the Al($2\bar{2}0$) reflection in the diffraction pattern in Figure 4.4. Representative features are marked by letters A, B, ..., G and is enlarged in Figure 4.9.

Dark-field imaging

Figure 4.8 shows a dark-field TEM image of the plan view sample. To obtain this image, an objective aperture was put onto the diffraction pattern in Figure 4.4. The aperture allows

only the Al($2\bar{2}0$) spots to go through. Note the sizes of the apertures used in the microscope are not ideal to perform the imaging. The smallest aperture only covers about 90% of the arc. The larger apertures are so large that the surrounding semiconductor reflections cannot be excluded. Therefore, one has to use the smallest aperture compromising some reflections, hence some grains are shown with a dark contrast.

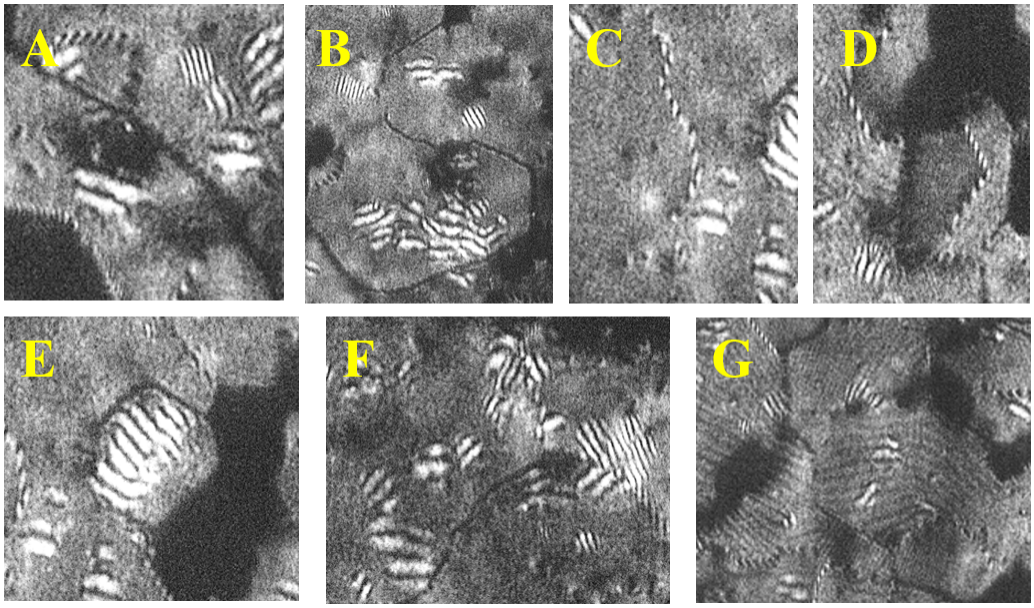

Figure 4.9. The representative features in Figure 4.8. A and B: the dark lines. C and D: the lines with bright fringes. E and F: areas with bright fringes. G: areas with darker fringes.

In Figure 4.8, one can distinguish four types of features. The representative features are marked by capitalized letters and enlarged in Figure 4.9.

Figure 4.9 A and B are representatives of the dark lines in the image. The image is mainly illuminated by the electron beams diffracted by the Al($2\bar{2}0$) planes. The appearance of dark lines implies missing order of planes on the line. Therefore, the interpretation of the dark lines is high angle grain boundaries, including the twin boundaries discussed in Section 4.1.1.

Figure 4.9 C and D are representatives of lines with fringes. The best interpretation of these lines is they are Moire fringes created by the overlapping of two grains that are rotated

from each other by a small angle. Generally, given the g-vectors of the two grains, $\mathbf{g}_1$ and $\mathbf{g}_2$, the wave vector of the Moire fringes created in the overlapping area of the two grains is calculated as [93]

$$\Delta\mathbf{g} = \mathbf{g}_1 - \mathbf{g}_2. \tag{4.10}$$

Therefore, the interval of the Moire fringes is

$$d_M = \frac{1}{|\mathbf{g}_1 - \mathbf{g}_2|}. \tag{4.11}$$

In this case, $\mathbf{g}_1$ and $\mathbf{g}_2$ are both g-vectors of Al($2\bar{2}0$) planes, just rotated by a small angle θ. The Equation 4.11 is rewritten as

$$d_M = \frac{1}{2|\mathbf{g}_{20\bar{2}}| \sin\frac{\theta}{2}} = \frac{d_{20\bar{2}}}{\theta}. \tag{4.12}$$

The last step is derived assuming θ is a small angle. Given $d_{20\bar{2}}$ =0.143 nm, the interval of the Moire frings in C and D (measured in the image process software) can be related to the relative rotation angle of the two grains . For C, the interval is 2.3 nm (3.6° rotation). For D, the interval is 1.6 nm (6.9° rotation). Based on the discussion above, the lines with fringes represent the low-angle rotation between the grains on two sides of the lines. Therefore, they are also grain boundaries.

Figure 4.9 E, F, and G are representatives of areas with fringes. The interval of E, F, and G are 3.5 nm, 2 nm, and 4 nm, respectively. One can interpretate this as Moire fringes created by two overlapped crystals. However, the overlapping of aluminum and semiconductor layers is better at explaining these fringes. Based on the discussion of the diffraction pattern Figure 4.4, the objective aperture put on Al($2\bar{2}0$) reflection also includes a double-diffracted reflection, diffracted by Al($\bar{2}20$) and Sm($6\bar{6}0$). The wave vector of the Moire fringes created by these two reflections is calculated in Equation 4.6. If the aluminum crystal has 0° rotation from the perfect alignment Y, the wave vector is calculated as $|\Delta\mathbf{g}|$ = 0.218 1/nm. Then the interval of the fringes takes $d_M = 1/|\Delta\mathbf{g}|$ = 4.59 nm. By rotating aluminum crystal by 0° to 8° from alignment Y, the interval decreases from 4.59 nm to 0.5 nm. This agrees with the value of the intervals measured above. It is also noteworthy that sometimes these Moire

fringes become darker or invisible. This is because the diffraction of Sm($6\bar{6}0$) is a high-order diffraction which has low intensity and sometimes difficult to see.

On the other hand, the overlapping of two relatively rotated aluminum crystals is not good at explaining these fringed areas. The existing observation does not provide any strong evidence of regions that contain two overlaying aluminum films with an in-plane rotation angle.

The grain size distribution can be extracted by looking at the boundaries. An average grain size can be obtained by the average-intercept method - drawing straight lines in the image and averaging their intercepts by the grain boundaries. Figure 4.10 presents the process of the average intercept method. The average grain size is 50 nm.

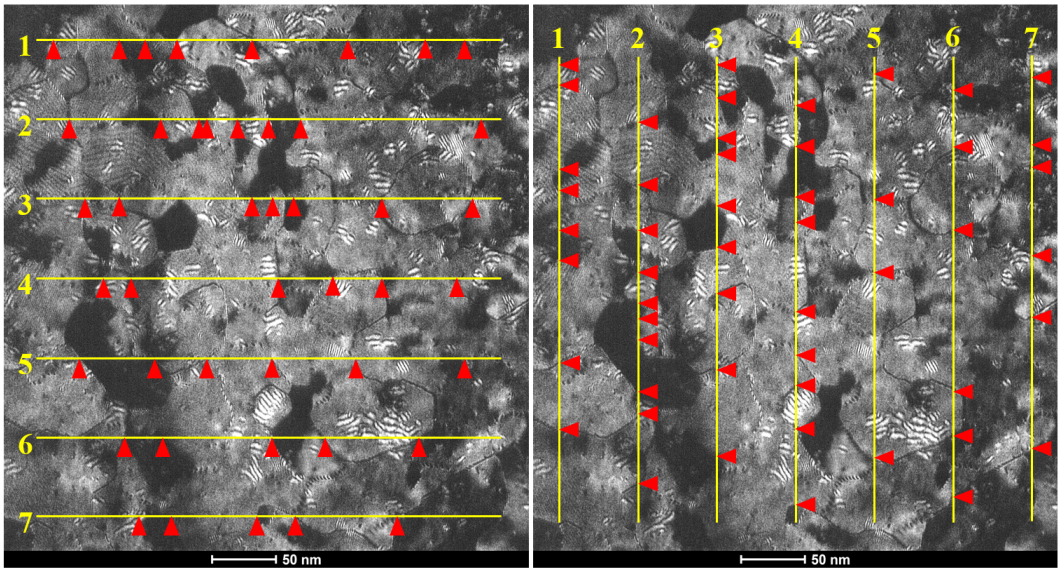

Figure 4.10. The average-intercept method to determine the average grain size in Al(111) film in S3. Fourteen 350-nm lines are drawn on the image. Seven of them are along Sm[110] (on the left) and seven of them are along Sm[$1\bar{1}0$] (on the right). The red triangles mark the intersections of the lines and the grain boundaries. In the left image, there are 45 intersections in the left picture, so the average intercept is 7×350/45=54 nm. In the right image, there are 52 intersections in the right picture, so the average intercept is 7×350/52=47 nm. The overall average grain size is 14×350/97= 50 nm.

4.2 Grain properties of Al(110)

In this section, the grain properties of aluminum film with unique (110) growth orientation is discussed using the same tool that was used to discuss the grain properties of Al(111) films.

4.2.1 Cross-sectional TEM imaging

In Chapter 3, Figure 3.3 showed a high-resolution TEM image of the aluminum film in sample S4 to explain how growth orientation (110) was characterized. The nearby area of Figure 3.3 was searched for evidence of grain boundaries. Although no image of the entire area was taken, Figure 4.11 shows an image that was made by putting two HRTEM images together. The area of the two images are next to each other and have a small overlap. The total width of the image is about 120 nm, similar to the width of Figure 4.1 (a).

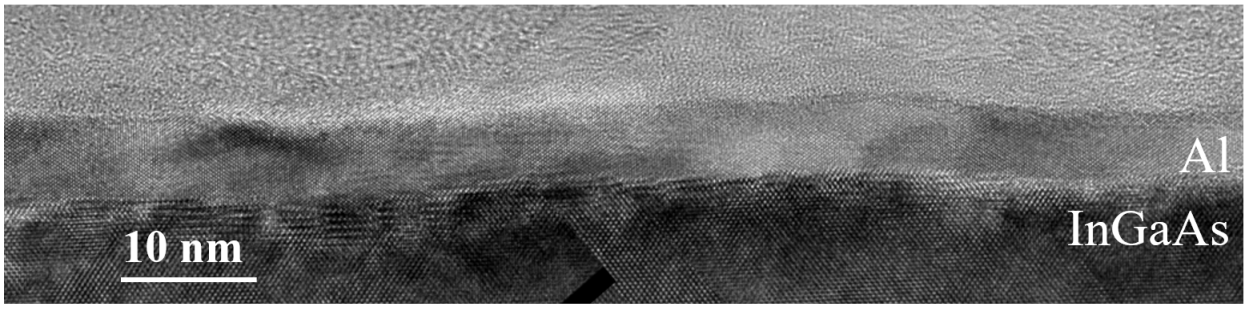

Figure 4.11. HRTEM image of the aluminum film in sample S4 with (110) growth orientation. This image is made by overlapping the images of two areas that are next to each other. The width of the image is about 120 nm. No grain boundaries are observed.

In Figure 4.11, although the underlying semiconductor layer has some contrast of disorder (could be caused by strain relaxation in the semiconductor layer), the aluminum film contains no grain boundary. Further searching in a wider area (200 nm - 300 nm) also showed no grain boundary. This observation indicates a major difference between Al(110) film and Al(111) film. Even though the Al(110) film may not be single-crystal, the density of grain

boundaries is much less than Al(111).

The diffraction pattern in Figure 3.3 can be used to obtain the crystal alignment, Al(111) [001] ∥ Sm(001)[1$\bar{1}$0] (denoted as "X"), which is the epitaxial orientation observed in the entire area of sample S4. Note unlike Y and Y' observed in Al(111), there is not an X' for X. The initial nucleus of an Al(111) grain can either be Y or Y', but the initial nucleus of an Al(110) grain is symmetric under 180° rotation (see Figure 4.12). This is a very important factor that keeps the density of grain boundaries in Al(110) low.

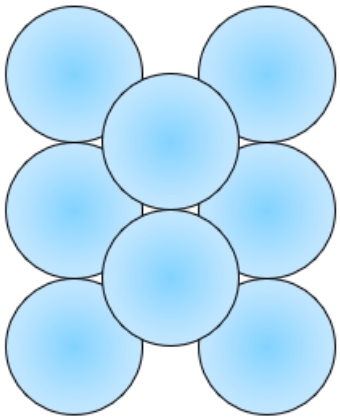

Figure 4.12. The configuration of two atomic layers of the Al(110) crystal. Al[110] direction points out of the page. Al[001] direction points to the right of the page. The crystal is symmetric under 180° rotation.

4.2.2 Plan view TEM imaging of Al(110) - Dark-field

Plan view TEM imaging is also used to study the grain distribution of the Al(110) films. The plan view sample presented in this section was made from sample S5 introduced in Chapter 3. The produced TEM sample contains not only areas with both aluminum film and semiconductor layer, but also a very thin area with aluminum film alone. In this section, dark-field imaging focused on the Al/Sm area is presented. In the next section, high-resolution TEM imaging focused only on the aluminum area will be presented.

Diffraction pattern

Figure 4.13 shows the diffraction pattern of the plan view sample from sample S5. Like the plan view sample of Al(111) from sample S2 in Section 4.1.2, here the direction of the sample was also noted to make sure they are distinguishable in the microscope. In the microscope, the sample was tilted according to the Kikuchi lines of the diffraction pattern of the semiconductor to find the correct zone-axis, in this case Sm[00$\bar{1}$].

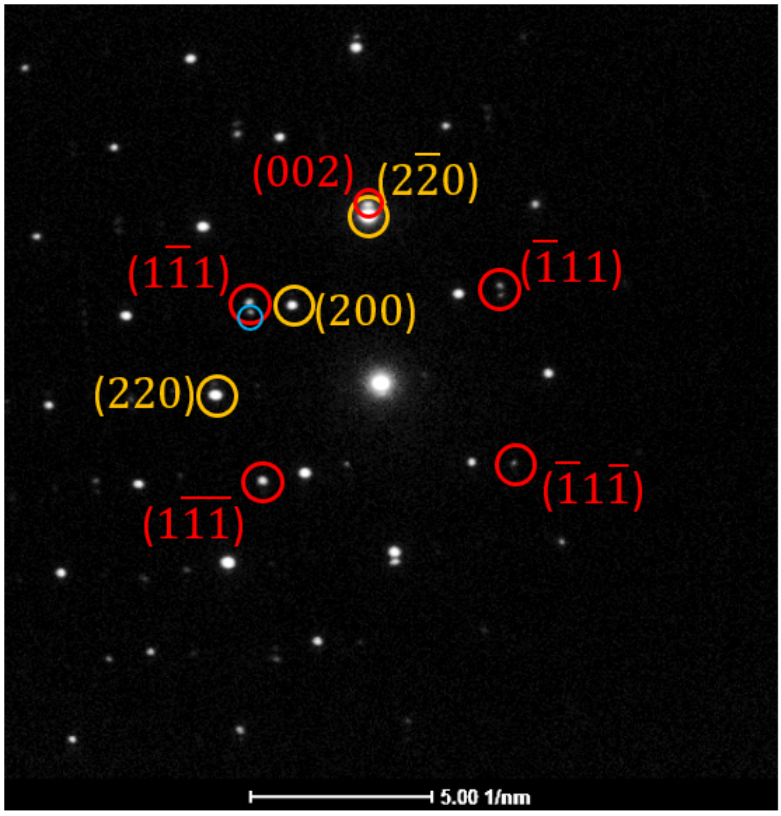

Figure 4.13. The diffraction pattern of a plan view sample of Al(110) film made in sample S5. The zone-axis is Sm[00$\bar{1}$]. The reflections of the aluminum film and semiconductor layers are marked out by red and orange circle, respectively. The blue circle marks the double-diffracted reflection diffracted by Al(1$\bar{1}\bar{1}$) and Sm($\bar{2}$20).

According to the note of sample directions, the reflections of the semiconductor layer are marked with theirs indices by orange circles. The most obvious aluminum reflections are the {111} reflections, marked in red. The diffraction pattern confirms that the epitaxial

orientation of the aluminum film is X: Al(111) [001] ‖ Sm(001)[1$\bar{1}$0]. The position of the Al(002) reflection is also marked. However, both Al{002} reflections are very close to the semiconductor reflections.

One major difference between the reflections of Al(110) film and the reflections of Al(111) film is that in Al(110) film the reflections are round spots instead of short arcs. Compared with Al(111) grains that have $[-8°, 8°]$ in-plane rotations relative to the perfect alignment Y and Y', the Al(110) film has much less rotation.

Similar with Figure 4.4, there are also double-diffracted reflections in the diffraction pattern in Figure 4.13. Here the blue circle marks the one that is most important to the discussion in the dark-field imaging part, which is the beam diffracted by Al(1$\bar{1}\bar{1}$) and Sm(2$\bar{2}$0). The g-vector of this double-diffracted beam is the vector resultant of the two, $\mathbf{g}_{\mathrm{dd}} = \mathbf{g}_{\mathrm{Al}(1\bar{1}\bar{1})} + \mathbf{g}_{\mathrm{Sm}(2\bar{2}0)}$. Figure 4.14 shows the geometric relationship of the reflections.

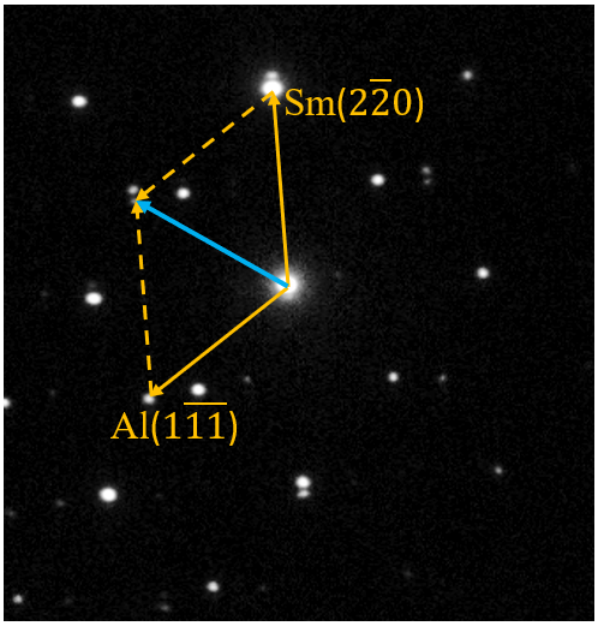

Figure 4.14. The g-vectors of Al(1$\bar{1}\bar{1}$) planes and Sm(2$\bar{2}$0) planes are drawn by orange arrow. The g-vector of the beam that is diffracted by Al(1$\bar{1}\bar{1}$) planes and Sm(2$\bar{2}$0) planes is the resultant of the two orange vectors, drawn by blue arrow.

The distance between the double-diffracted reflection marked in blue is very close to the reflection of Al($1\bar{1}1$) because the vector subtraction is

$$\begin{aligned}\Delta\mathbf{g} &= \mathbf{g}_{\mathrm{Al}(1\bar{1}1)} - [\mathbf{g}_{\mathrm{Al}(1\bar{1}\bar{1})} + \mathbf{g}_{\mathrm{Sm}(2\bar{2}0)}] \\ &= \mathbf{g}_{\mathrm{Al}(1\bar{1}1)} - \mathbf{g}_{\mathrm{Al}(1\bar{1}\bar{1})} - \mathbf{g}_{\mathrm{Sm}(2\bar{2}0)} \\ &= \mathbf{g}_{\mathrm{Al}(002)} - \mathbf{g}_{\mathrm{Sm}(2\bar{2}0)}.\end{aligned} \tag{4.13}$$

The result shows that the relative position between the Al($1\bar{1}1$) reflection and the double-diffracted reflection is equivalent to the relative position between Al(002) and Sm($2\bar{2}0$) reflections, which is very small (show in Figure 4.13). As discussed in the dark-field imaging part, Moire fringes is observed when putting an objective aperture on Al($1\bar{1}1$) to create dark-field images, since the aperture also includes the double-diffracted reflection.

Dark-field imaging

Figure 4.15 shows a dark-field TEM image of the plan view sample. To take the image, an objective aperture was put onto the diffraction pattern in Figure 4.13 to allow only the transmission of Al($1\bar{1}1$) beam. The plan view image is very different from the plan view image of Al(111) in Figure 4.8. There is no obvious grain boundary in the image. There are dark areas, which cannot be related to those dark areas in Figure 4.8 as the objective aperture includes the whole reflection. Here the darker areas are best interpreted as less ordered areas that include defects.

The most obvious feature in Figure 4.15 is the Moire fringes that cover the entire image. An average interval of 3.5 nm was measured by the image processing software. As discussed in Figure 4.13 and Figure 4.14, the Moire pattern is created by the interference between the Al($1\bar{1}1$) reflection and the double-diffracted reflection by Al($1\bar{1}\bar{1}$) and Sm($2\bar{2}0$). From

Equation 4.13, given no rotation between Al[002] and Sm[2$\bar{2}$0], the interval of the Moire fringes is calculated as:

$$d_M = \frac{1}{|\Delta \mathbf{g}|} = \frac{d_{\mathrm{Al}(002)} d_{\mathrm{Sm}(2\bar{2}0)}}{|d_{\mathrm{Al}(002)} - d_{\mathrm{Sm}(2\bar{2}0)}|} = 3.5 \text{ nm}. \tag{4.14}$$

The result matches the measured result of the interval of the Moire fringes and confirms the hypothesis of why the Moire fringes are formed.

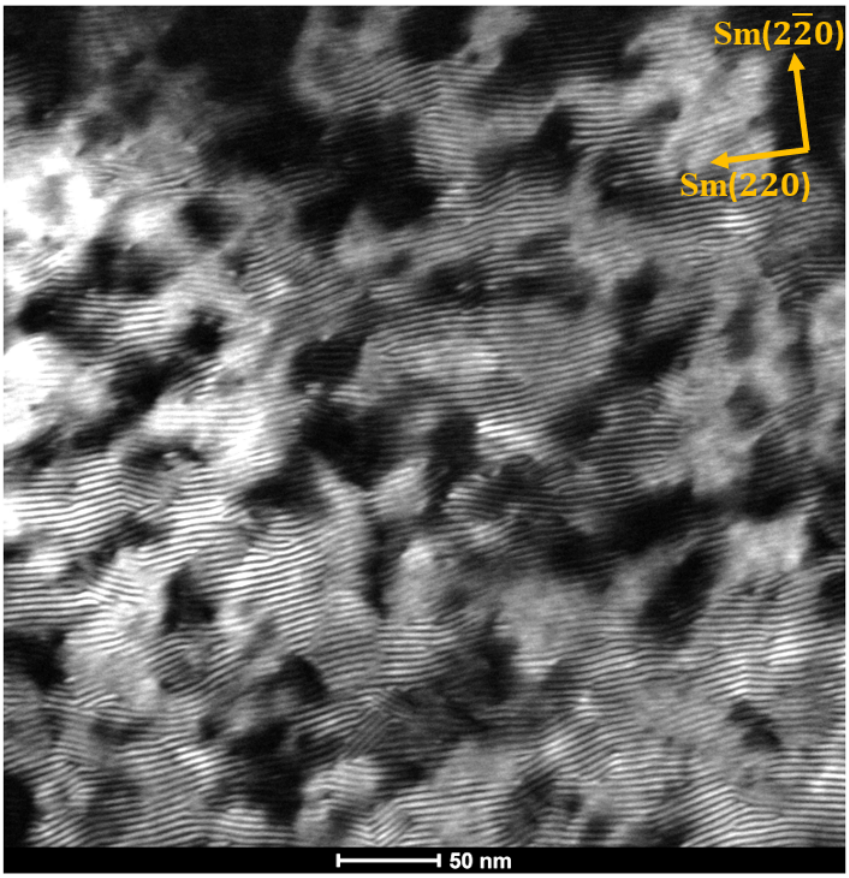

Figure 4.15. Dark-field TEM imaging of the plan view sample from S5. The aperture was used to pick up the Al(1$\bar{1}\bar{1}$) reflection in the diffraction pattern in Figure 4.13.

There are both Moire fringes created by overlapping of aluminum film and semiconductor layers in Figure 4.8 and 4.15. The difference is noteworthy. In Figure 4.8, the double-diffracted beam included in the objective aperture is diffracted by Al($\bar{2}$20) and Sm(6$\bar{6}$0).

The diffraction of Sm($6\bar{6}0$) is weak. In Figure 4.15, the double-diffracted beam is diffracted by Al($1\bar{1}\bar{1}$) and Sm($2\bar{2}0$). The diffraction of Sm($2\bar{2}0$) is much stronger than Sm($6\bar{6}0$). This can explain why the Moire pattern is obvious in the entire image of Figure 4.15.

From Equation 4.13, the direction of the Moire fringes can also be determined. Given θ is the rotation angle of the aluminum crystal from the perfect alignment X and α is the angle between the wave vector of the fringes $\Delta\mathbf{g}$ and Sm[$2\bar{2}0$], one can calculate:

$$|\Delta\mathbf{g}| = (|\mathbf{g}_{\mathrm{Al}(002)}|^2 + |\mathbf{g}_{\mathrm{Sm}(2\bar{2}0)}|^2 - 2|\mathbf{g}_{\mathrm{Al}(002)}||\mathbf{g}_{\mathrm{Sm}(2\bar{2}0)}|\cos\theta)^{\frac{1}{2}} \tag{4.15}$$

and

$$\begin{aligned}
\cos\alpha &= \frac{\Delta\mathbf{g}\cdot\mathbf{g}_{\mathrm{Sm}(2\bar{2}0)}}{|\Delta\mathbf{g}||\mathbf{g}_{\mathrm{Sm}(2\bar{2}0)}|} \\
&= \frac{\mathbf{g}_{\mathrm{Al}(002)}\cdot\mathbf{g}_{\mathrm{Sm}(2\bar{2}0)} - |\mathbf{g}_{\mathrm{Sm}(2\bar{2}0)}|^2}{|\Delta\mathbf{g}||\mathbf{g}_{\mathrm{Sm}(2\bar{2}0)}|} \\
&= \frac{|\mathbf{g}_{\mathrm{Al}(002)}||\mathbf{g}_{\mathrm{Sm}(2\bar{2}0)}|\cos\theta - |\mathbf{g}_{\mathrm{Sm}(2\bar{2}0)}|^2}{|\Delta\mathbf{g}||\mathbf{g}_{\mathrm{Sm}(2\bar{2}0)}|} \\
&= \frac{|\mathbf{g}_{\mathrm{Al}(002)}|\cos\theta - |\mathbf{g}_{\mathrm{Sm}(2\bar{2}0)}|}{(|\mathbf{g}_{\mathrm{Al}(002)}|^2 + |\mathbf{g}_{\mathrm{Sm}(2\bar{2}0)}|^2 - 2|\mathbf{g}_{\mathrm{Al}(002)}||\mathbf{g}_{\mathrm{Sm}(2\bar{2}0)}|\cos\theta)^{\frac{1}{2}}} \\
&= \frac{d_{\mathrm{Sm}(2\bar{2}0)}\cos\theta - d_{\mathrm{Al}(002)}}{(d^2_{\mathrm{Al}(002)} + d^2_{\mathrm{Sm}(2\bar{2}0)} - 2d_{\mathrm{Al}(002)}d_{\mathrm{Sm}(2\bar{2}0)}\cos\theta)^{\frac{1}{2}}}.
\end{aligned} \tag{4.16}$$

The relationship between α and θ in Equation 4.16 is plotted in Figure 4.16.

The plot in Figure 4.16 shows how Moire fringes rotate as a function of the rotation angle between aluminum and semiconductor. The rotation of the crystal is highly magnified by the rotation of the Moire fringes as a 1° rotation can cause a 16° rotation of the Moire fringes. This agrees with the observation in Figure 4.15. The relative rotation between Moire fringes is an obvious characteristics of the image, which implies relative rotation between aluminum crystal in different area. These areas can also be treated as grains although no obvious grain boundaries are observed. In rough measurements, in all areas, the rotation angles of Moire fringes from Sm[220] direction is less than 20°. According to the plot in Figure 4.16, this

indicates the rotation angle of the crystal is less than 1.3°.

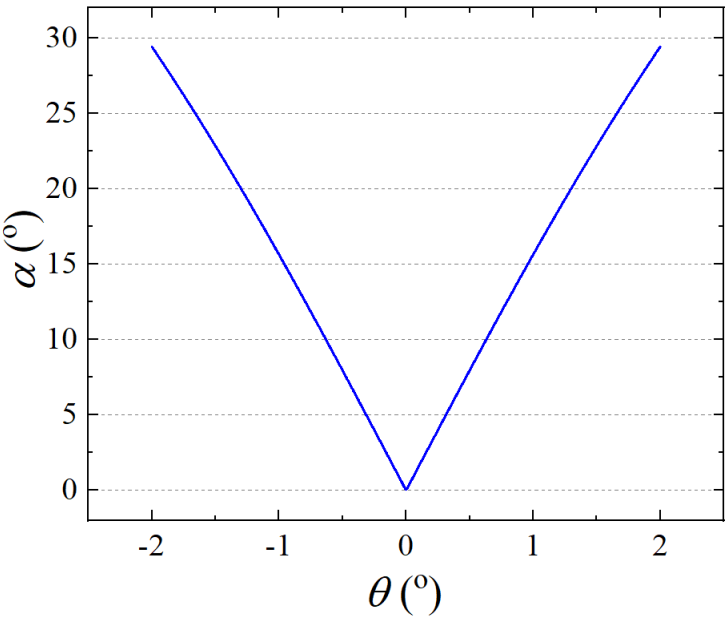

Figure 4.16. The blue curve plots the relationship between α and θ in Equation 4.16.

More than rough measurement, the plot in Figure 4.16 can be used to mark out the area and rotation angle of each grain in Figure 4.15. A proposed analysis is presented in the next section.

4.2.3 Plan view TEM imaging of Al(110) - Bright-field

This section describes the bright-field and high-resolution TEM imaging focusing on the thin area of the same plan view sample of S5. The thin area contains only the aluminum layer, which implies the thickness of this area is only about 10 nm. It did not fall off because it is connected and supported by the surrounding thicker areas. High-resolution TEM imaging is able to perform on the area that shows atomic resolution of the film.

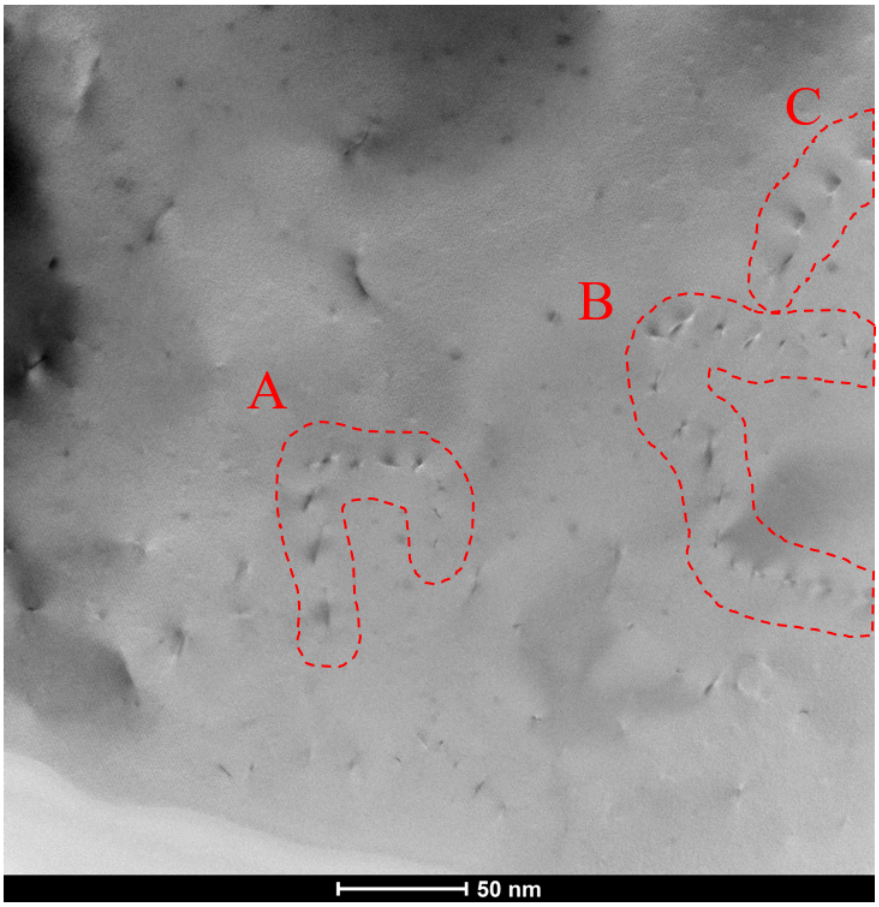

Figure 4.17. A bright-field TEM imaging of the thin area in the plan view sample from S5. The zone-axis is Sm[00$\bar{1}$]. The red dashed lines mark out areas with defect arrays.

Figure 4.17 shows a bright-field TEM image of this thin region. The sample was tilted in the microscope to the correct zone-axis, in this case Sm[00$\bar{1}$]. The most obvious features in this image can be seen in the areas marked by A, B, and C. An array of defects with short dark line contrast appears in each area. The dark lines in bright-field imaging indicates dislocations [93]. An array of dislocations represents a low-angle misorientation between the crystal on the two sides of the dislocation array (a low-angle grain boundary) [103]. To detect the relative rotation between the crystals on the two sides, a higher magnification image of the defect array in area A is shown in Figure 4.18.

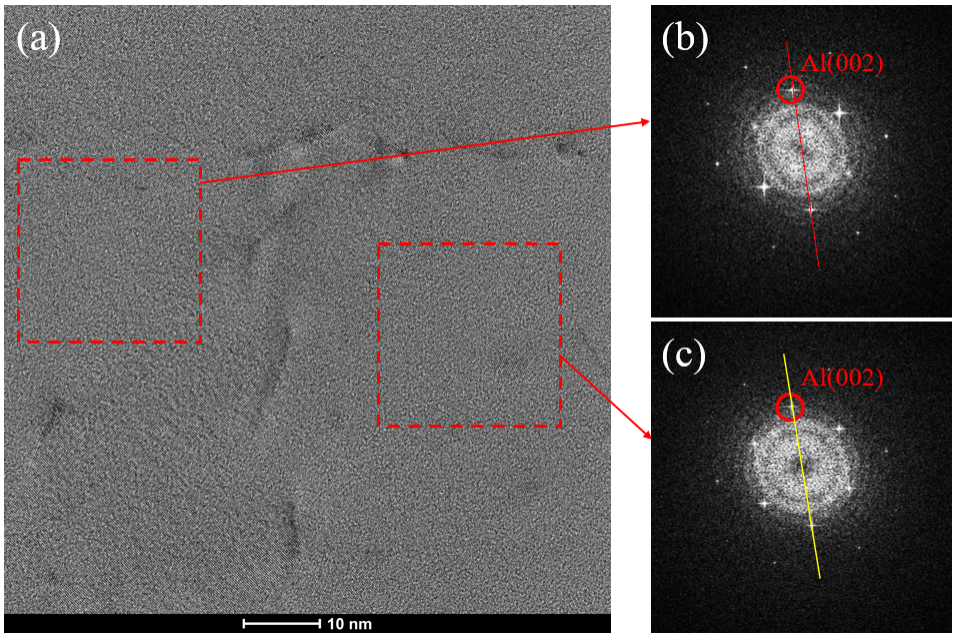

Figure 4.18. (a) is a higher magnification image of the defect array near the letter "A" in Figure 4.17. (b) and (c) are FFT patterns of the image on the left-hand side of the defects and the image on the right-hand side of the defects. The direction of the FFT patterns are marked by connecting the Al{002} spots. A 0.91° rotation can be measured between the red and yellow lines.

Fast Fourier transformation (FFT) is performed on the image on both sides of the defect array in Figure 4.18 (a). The FFT patterns are shown in Figure 4.18 (b) for the left-hand side and Figure 4.18 (c) for the right hand side, respectively. A 0.91° degree rotation is observed between the FFT patterns, measured by counting pixels in image processing software. This confirms the low-angle rotation between the two areas. The angle of the rotation is also in the range determined by the analysis of Moire pattern directions in Figure 4.15.

Assume the magnitude of the Burgers vector of the dislocation is the displacement of moving the Al crystal by one atom along Al[110] direction, $b = 0.286$ nm. (Note for aluminum which is FCC, the Burgers vector depends on the type of the dislocation, full or partial [104]. But the assumption is approximately valid.) Then the average distance of the dislocations can be calculated by the rotation angle θ [103]:

$$d = \frac{b}{\theta} = 18.0 \text{ nm}, \tag{4.17}$$

which agrees with the observation in Figure 4.18.

Now the grain properties of the Al(110) film becomes clearer. The film is made up of slightly rotated grains with low-angle grain boundaries formed between them. To get a good picture of grain distribution, a divison-FFT method to analyze Figure 4.17 is described as follows.

The image is divided into very small areas, and the information of the crystal rotation for each small area is extracted. For instance, in the following process, Figure 4.17 is cut into 20×20=400 squares. The size of each small image is approxmiately 16.5×16.5 nm^2. Figure 4.19 (a) shows the first small image (the one on the top-left) among these 400 pictures. Note the resolution of the original image is good so one can still see very detailed information, such as atomic planes, in the small image. Figure 4.19 (b) shows the FFT pattern of Figure 4.19 (a).

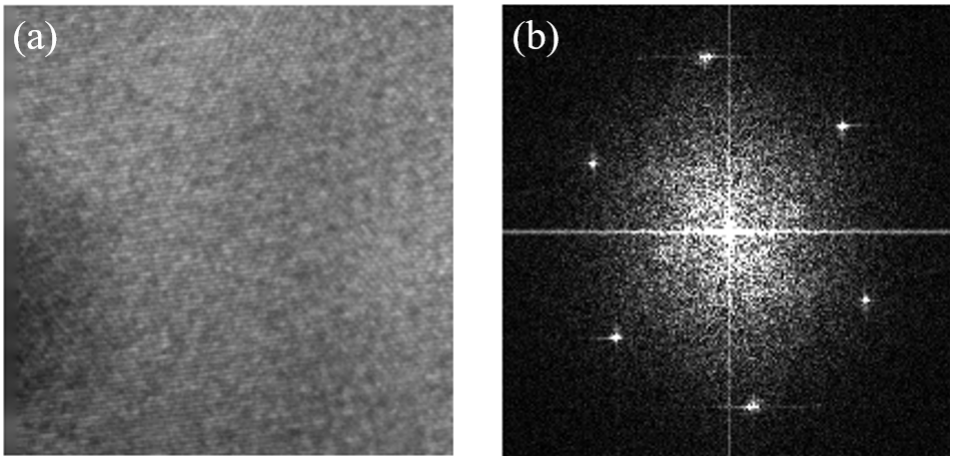

Figure 4.19. The HRTEM image in Figure 4.17 is divived into 20×20 small images. As an example, (a) shows the first (top-left) small image. (b) shows the FFT pattern of (a).

The orientation of the FFT pattern can be extracted by the position of the Al(002) spot. To be specific, in the FFT pattern which is also an image, each pixel has a X-coordinate (the number of the coloumn the pixel is in, counting from the left), a Y-coordinate (the number of row the pixel is in, couting from the top), and the intensity. By comparing the intensities

of the pixels in the first 20% rows of the FFT pattern, the Al(002) spot can be located as the pixel with the largest intensity. The range, first 20% rows of the pattern, is to exclude other spots of the pattern from being extracted. Assume the X-coordinate and Y-coordinate of the Al(002) spot are X_m and $_m$, the rotation angle θ can be calculated as:

$$\theta = \arctan \frac{X_0 - X_m}{Y_0 - Y_m} - \theta_0, \tag{4.18}$$

where X_0 and Y_0 are the coordinates of the center of the FFT pattern and θ_0 is the angle between Sm[1$\bar{1}$0] and the vertical direction of the image, which represents the orientation of the FFT pattern of exact Al(110) [001] || Sm(001)[1$\bar{1}$0] alignment. By performing FFT on all small images, the angle of rotation can be extracted for each small image. Finally a colored contour of the angle value can be obtained. The division, FFT, and angle measurement were realized by writing a program in MATLAB. In MATLAB, the input image is treated as a matrix.

After several attempts, the 20×20 division was found to give the best result. Ideally denser division leads to higher resolution of the final contour map. However, if the image was divided into more pieces, the number of pixels in the resulting small image would be lower, which affected the angular resolution of their FFT patterns. Assume the number of division is N. The pixel number of the original image is 4096×4096. Therefore, the small images after division and their FFT patterns have a pixel number of $(4096/N) \times (4096/N)$. The angular resolution of the FFT pattern is approximately the opening angle of one pixel to the center, which can be expressed as:

$$\Delta\theta = \frac{1}{d}, \tag{4.19}$$

where d is the distance from the extracted pixel to the center, in the unit of pixels. The example in Figure 4.19 (b) shows that d is approximately 40% of the height of the FFT pattern image, $4096/N$. As a result, the angular resolution depends on N as follows:

$$\Delta\theta = \frac{N}{0.4 \times 4096}. \tag{4.20}$$

For 20×20 division, $\Delta\theta = 0.7°$, which leads to an error bar of $\pm 0.35°$. For 25×25 division, $\Delta\theta = 0.9°$, which leads to an error bar of $\pm 0.45°$.

Figure 4.20 shows the rotation angle contour of the Figure 4.17 using the division-FFT method described above. This contour shows that the rotation angles are all lower than 1.2°, or lower than 1.6° if considering the error bar.

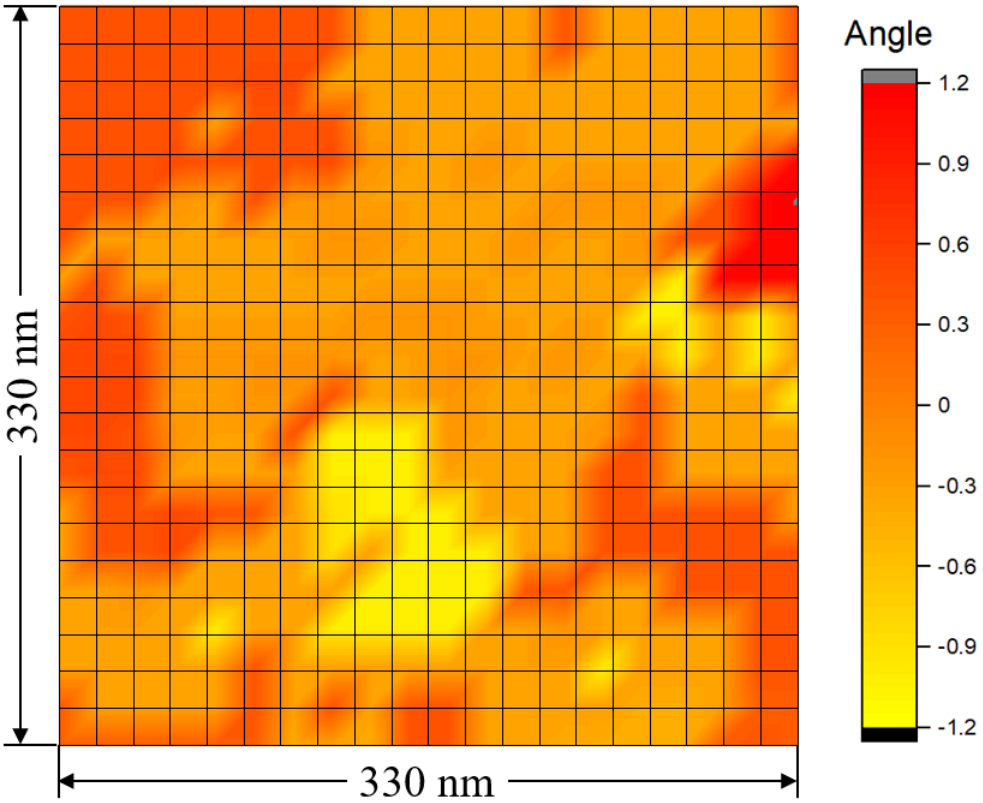

Figure 4.20. The rotation angle contour of Figure 4.17. The contour is obtained using the division-FFT method described in the text. The black grid lines shows how the image is divided. 0° is the exact Al(110) [001] ‖ Sm(001)[1$\bar{1}$0] orientation (X). The clockwise rotation is positive.

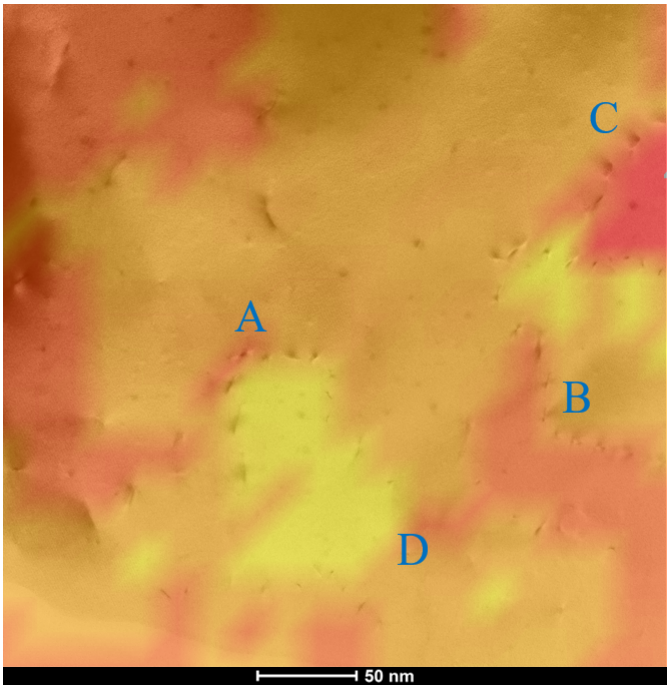

Figure 4.21. The rotation angle contour of Figure 4.17 overlapped with the original image.

By adjusting the transparency of the rotation angle contour, it can be overlapped with the original image in Figure 4.17, as shown in Figure 4.21. From this image, one can see the position of the low-angle grain boundaries in area A, B, and C fits the position of the color change very well. The yellow color of the area below the dislocation array in area A also tells the rotation angle of the area is approximately -1°, which agrees with the analysis of Figure 4.18. However, there is also area like area D, where rotation occurs (color change observed) but there are not as many defects to form a grain boundary. The main reason of this is the rotation angle is very small. In equation 4.17, if θ is small, for instance, 0.3°, the average distance of the dislocations becomes 54 nm, so one should expect only few dislocations that do not look like a boundary.

The size of the areas in different color can be extracted from Figure 4.20 by counting the number of squares contained and can be used to estimate the grain size. However, based on the calculation of error bars above, the size of the large orange region should not be considered since low angle relative rotations can exist but is not detected by the contour. The yellow area below the dislocation array in area A however can be used to estimate the

grain size since the rotation angle is larger enough to be detected. It can be divided into two areas by the orange area in between. Each yellow area contains 10 sqaures (2772 nm^2). The average edge length of this yellow area is about $\sqrt{2772} = 52$ nm.

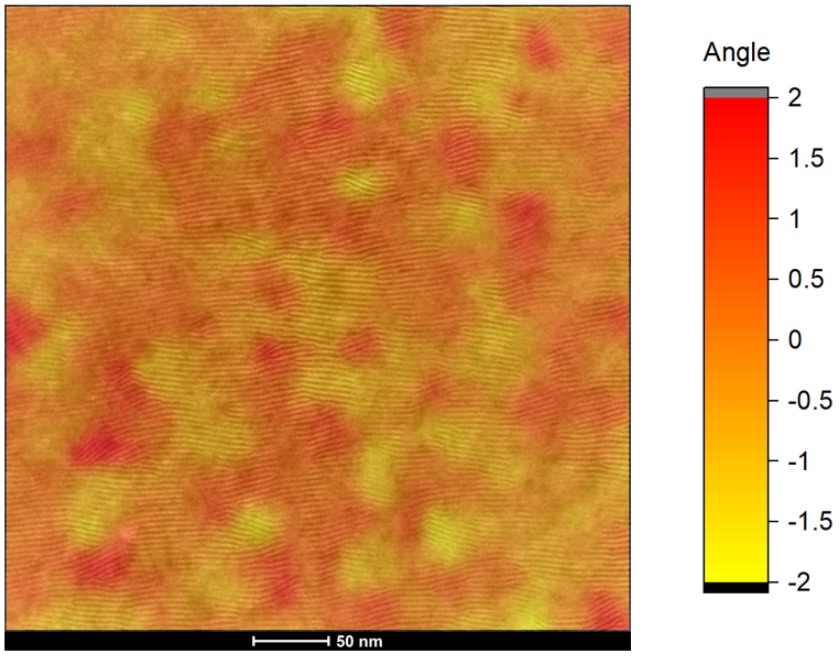

Figure 4.22. The rotation angle contour of a bright-field images of the Al/Sm overlapped area in the plan view sample from S5. The contour is obtained using the division-MF method described in the text. 0° is the exact Al(110) [001] ‖ Sm(001)[1$\bar{1}$0] orientation (X). The clockwise rotation is positive.

The division-FFT method introduced above matches the dislocation arrays and the change of angles. However, the above estimation of the average grain size only considers the sizes of one or two grains. It is limited by the angular resolution of the method. To get a more statistical result of the average grain size, a division-MF method is used based on the magnification effect of the angle of Moire-fringes (MF) discussed in Figure 4.16. This method must be applied on the images in the areas that contain both aluminum and semiconductor. After dividing the original image into small pieces, instead of measuring the orientation of the FFT pattern, the angle of the fringes are measured. And then, the rotation angle of aluminum is obtained using the relationship plotted in Figure 4.16. Figure

4.22 shows a rotation angle contour obtained using the division-MF method. The contour has been overlapped with the original image. The image is taken from the area with both aluminum and semiconductor so the Moire fringes can be observed. The original image is divided into 30×30=900 squares. The angle of Moire fringes in these 900 small images are measured manually.

The error bar of the division-MF method mainly comes from the error of manual measurements of the angle of fringes. A good estimation of the error bar of manual measurements is ±1°. However, because the fringe angle magnifies the rotation angle by approximately 16×, the error bar of the real rotation angle is $\pm 1/16 = \pm 0.06°$, which is much smaller than the error bar of division-FFT method. In Figure 4.22, one can see the color change matches exactly with the change of angle of Moire fringes.

The average grain size can be obtained by applying the average-intercept method, shown in Figure 4.23. The resulting average grain size is 50 nm.

4.2.4 Discussion

The experimental results presented in this chapter mainly focuses on two aspects of the grain properties of Al(111) and Al(110) films. One is the grain size. The other one is the orientation of different grains. The grain size of Al(111) is about 50 nm, directly measured from the dark field imaging. The grain size of Al(110) is also about 50 nm, although division-FFT and division-MF method must be used to distinguish the grains. On the other hand, the in-plane rotation of grains is very different between Al(111) and Al(110). For Al(111), the rotation angle is in the range of [-8°,8°]. For Al(110), the rotation angle is in the range of [-1.5°,1.5°], much less than Al(111). Discussion is presented focusing on these two aspects.

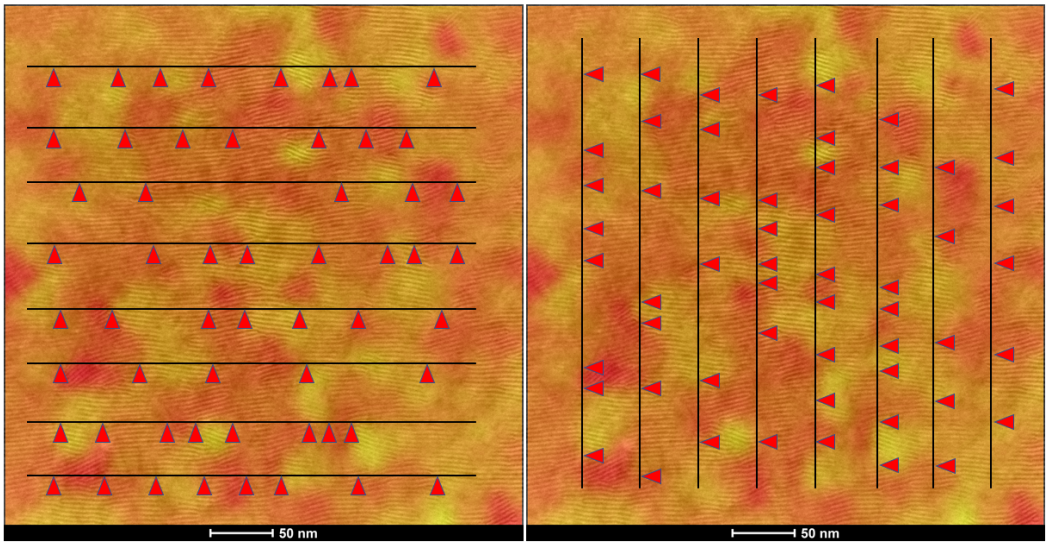

Figure 4.23. The average-intercept method to determine the average grain size of Al(110) film in S5. Sixteen 350-nm lines are drawn on the image. Eight of them are along Sm[110] (on the left) and eight of them are along Sm[1$\bar{1}$0] (on the right). The red triangles mark the intersections of the lines and the grain boundaries. In the left image, there are 56 intersections in the left picture, so the average intercept is 8×350/56=50 nm. In the right image, there are 57 intersections in the right picture, so the average intercept is 8×350/57=49 nm. The overall average grain size is 16×350/99= 50 nm.

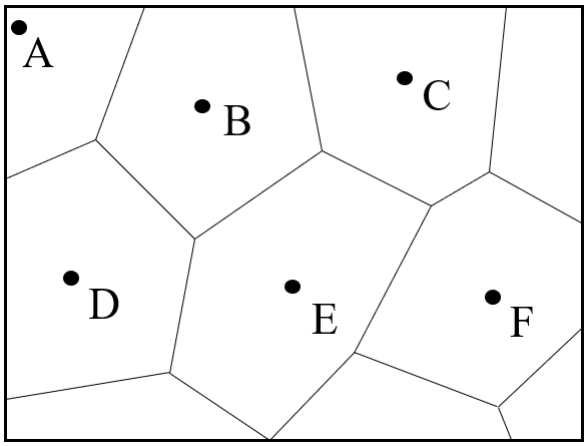

Figure 4.24. A schematic diagram of an aluminum film area that contains several grains. The grain boundaries are drawn in black lines. The black spots mark the initial nucleus of each grain.

Grain size

The similarity of the average grain size between Al(111) and Al(110) is not a surprising result. One should consider the relationship between the average grain size and the density

of nucleation events at the beginning of the growth. Figure 4.24 shows a schematic diagram of an area of aluminum film that contains several grains. The black lines represent the grain boundaries. The black round spots mark the initial nucleus of each grain. The size of the grain shows how far a nucleus can grow before it collides with the islands grown from other nuclei. Therefore, ignoring the difference in growth speed, the average grain size gives a rough measurement of the average distance between the initial nucleation events.

The initial nucleation events happen when a group of aluminum atoms diffusing on the semiconductor surface meet each other and make a cluster. If the Gibbs free energy of this cluster exceeds a critical barrier, the growth of an island starts [54]. The distance of these initial nucleation events mainly depends on growth rate and substrate temperature, because these two growth conditions determines the average diffusion length, which is the distance that an atom travels before colliding with other atoms and making a cluster. Therefore, the similarity of the growth rates and substrate temperatures between Al(111) and Al(110) films explains the similarity of their grain sizes.

In-plane rotation

The difference between Al(111) and Al(110) in the range of in-plane rotation needs to be understood. The rotation of the grains comes from the misalignment of their initial nucleus. As discussed above, there is a critical Gibbs free energy barrier that a cluster must come across to start the island growth. The critical Gibbs free energy barrier depends mainly on the surface energy and interfacial energy [54], so the barrier is different for clusters with different misalignment angle because of the difference in the interfacial energy (surface energy does not depend on the misalignment). As a result, if a cluster has too large a rotation angle, the energy barrier of successful nucleation is too large to start the island growth.

Therefore, the preliminary conclusion is, the different range of in-plane rotation reflects how the interfacial energy of Al(111) and Al(110) depend on the rotation angle. Based on symmetry, the precisely aligned orientation X: Al(110) [001] $\parallel$ Sm(001)[1$\bar{1}$0] and Y: Al(111) [1$\bar{1}$0] $\parallel$ Sm(001)[1$\bar{1}$0] have the lowest interfacial energy. With some degree of in-plane rota-

tion, the interfacial energy of Al(111) is less sensitive, so clusters with higher rotation angle can survive. However, the interfacial energy of Al(110) is more sensitive to rotation, so even slightly rotated clusters will not start the island growth. Figure 4.25 draws the expected angular dependence of interfacial energy for Al(111) and Al(110).

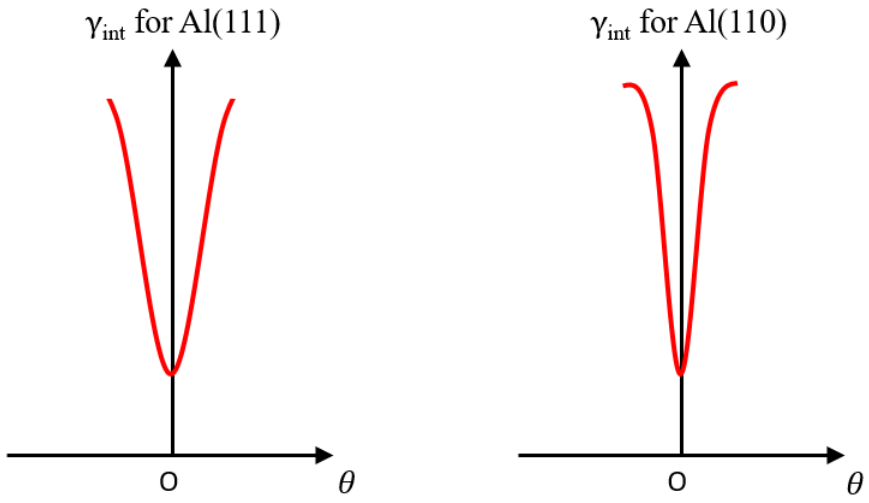

Figure 4.25. The expected relationship between in-plane rotation angle and interfacial energy of Al(111) (on the left) and Al(110) (on the right) film.

It is noteworthy that it is a normal case in the literature that films with FCC(111) normal orientation is less sensitive to in-plane rotation [102], [105]–[107]. Reference [105] studied gold deposited on (001) surface of alkali halide substrates. When the growth orientation is (111) (grown at room temperature), the gold film showed textural orientation. When the growth orientation is (001) (grown at raised temperature), the gold film also showed in-plane alignment. This result is explained by the similarity of the contacting atomic planes. For (111) growth orientation, the gold (111) plane with a hexagonal symmetry is in contact with the alkali halide substrate with a square symmetry. Since the similarity is weak, the gold crystal showed more rotation freedom. On the other hand, for (001) growth orientation, two surfaces with square symmetry are in contact, which permits better alignment.

In this thesis, in Al(111)/Sm(001) interface, a hexagonal plane is in contact with a

square plane. In Al(110)/Sm(001) interface, a rectangular plane is in contact with a square plane. Al(110)/Sm(001) interface can be more sensitive to alignment since compared with a square plane, a rectangular plane has more similarity than a hexagonal plane. More quantitative understanding requires theoretical calculations of the interfacial energies, which is an interesting direction of future study.

REFERENCES

[1] A. Klapwijk, "Proximity Effect from an Andreev Perspective," *Journal of Superconductivity*, vol. 17, no. 5, pp. 593–611, 2004. DOI: 10.1007/s10948-004-0773-0.

[2] B. Pannetier and H. Courtois, "Andreev Reflection and Proximity Effect," *Journal of Low Temperature Physics*, vol. 118, no. 5/6, pp. 599–615, 2000. DOI: 10.1023/a:1004635226825.

[3] A. Y. Kitaev, "Unpaired Majorana Fermions in Quantum Wires," *Psychological Review*, vol. 44, pp. 131–136, 10S 2001. DOI: 10.1070/1063-7869/44/10s/s29.

[4] Y. Oreg, G. Refael, and F. V. Oppen, "Helical Liquids and Majorana Bound States in Quantum Wires," *Physical Review Letters*, vol. 105, no. 17, 2010. DOI: 10.1103/physrevlett.105.177002.

[5] R. M. Lutchyn, J. D. Sau, and S. D. Sarma, "Majorana Fermions and a Topological Phase Transition in Semiconductor-Superconductor Heterostructures," *Physical Review Letters*, vol. 105, no. 7, 2010. DOI: 10.1103/physrevlett.105.077001.

[6] J. D. Sau, R. M. Lutchyn, S. Tewari, and S. D. Sarma, "Generic New Platform for Topological Quantum Computation Using Semiconductor Heterostructures," *Physical Review Letters*, vol. 104, no. 4, 2010. DOI: 10.1103/physrevlett.104.040502.

[7] J. Alicea, "Majorana Fermions in a Tunable Semiconductor Device," *Physical Review B*, vol. 81, no. 12, 2010. DOI: 10.1103/physrevb.81.125318.

[8] R. M. Lutchyn, E. P. A. M. Bakkers, L. P. Kouwenhoven, P. Krogstrup, C. M. Marcus, and Y. Oreg, "Majorana Zero Modes in Superconductor-Semiconductor Heterostructures," *Nature Reviews Materials*, vol. 3, no. 5, pp. 52–68, 2018. DOI: 10.1038/s41578-018-0003-1.

[9] A. Y. Kitaev, "Quantum Computations: Algorithms and Error Correction," *Russian Mathematical Surveys*, vol. 52, no. 6, pp. 1191–1249, 2003. DOI: 10.1070/rm1997v052n06abeh002155.

[10] A. Y. Kitaev, "Fault-tolerant Quantum Computation by Anyons," *Annals of Physics*, vol. 303, no. 1, pp. 2–30, 2003. DOI: 10.1016/s0003-4916(02)00018-0.

[11] D. A. Ivanov, "Non-Abelian Statistics of Half-Quantum Vortices in p-Wave Superconductors," *Physical Review Letters*, vol. 86, no. 2, pp. 268–271, 2001. DOI: 10.1103/physrevlett.86.268.

[12] C. Nayak, S. H. Simon, A. Stern, M. Freedman, and S. D. Sarma, "Non-Abelian Anyons and Topological Quantum Computation," *Reviews of Modern Physics*, vol. 80, no. 3, pp. 1083–1159, 2008. DOI: 10.1103/revmodphys.80.1083.

[13] P. W. Shor, "Scheme for Reducing Decoherence in Quantum Computer Memory," *Physical Review A*, vol. 52, no. 4, 1995. DOI: 10.1103/physreva.52.r2493.

[14] V. Mourik, K. Zuo, S. M. Frolov, S. R. Plissard, E. P. A. M. Bakkers, and L. P. Kouwenhoven, "Signatures of Majorana Fermions in Hybrid Superconductor - Semiconductor Nanowire Devices," *Science*, vol. 336, no. 6084, pp. 1003–1007, 2012. DOI: 10.1126/science.1222360.

[15] M. T. Deng, C. L. Yu, G. Y. Huang, M. Larsson, P. Caroff, and H. Q. Xu, "Anomalous Zero-Bias Conductance Peak in a Nb-InSb Nanowire-Nb Hybrid Device," *Nano Letters*, vol. 12, no. 12, pp. 6414–6419, 2012. DOI: 10.1021/nl303758w.

[16] H. O. H. Churchill, V. Fatemi, K. Grove-Rasmussen, M. T. Deng, P. Caroff, H. Q. Xu, and C. M. Marcus, "Superconductor-Nanowire Devices from Tunneling to the Multichannel Regime: Zero-Bias Oscillations and Magnetoconductance Crossover," *Physical Review B*, vol. 87, no. 24, 2013. DOI: 10.1103/physrevb.87.241401.

[17] S. Takei, B. M. Fregoso, H. Hui, A. M. Lobos, and S. D. Sarma, "Soft Superconducting Gap in Semiconductor Majorana Nanowires," *Physical Review Letters*, vol. 110, no. 18, 2013. DOI: 10.1103/physrevlett.110.186803.

[18] M. A. Paalanen, D. C. Tsui, A. C. Gossard, and J. C. M. Hwang, "Disorder and the Fractional Quantum Hall effect," *Solid State Communications*, vol. 50, no. 9, pp. 841–844, 1984. DOI: 10.1016/0038-1098(84)90343-0.

[19] P. Krogstrup, N. L. B. Ziino, W. Chang, S. M. Albrecht, M. H. Madsen, E. Johnson, J. Nygård, C. M. Marcus, and T. S. Jespersen, "Epitaxy of Semiconductor-Superconductor Nanowires," *Nature Materials*, vol. 14, no. 4, pp. 400–406, 2015. DOI: 10.1038/nmat4176.

[20] W. Chang, S. M. Albrecht, T. S. Jespersen, F. Kuemmeth, P. Krogstrup, J. Nygård, and C. M. Marcus, "Hard Gap in Epitaxial Semiconductor-Superconductor Nanowires," *Nature Nanotechnology*, vol. 10, no. 3, pp. 232–236, 2015. DOI: 10.1038/nnano.2014.306.

[21] J. Shabani, A. P. Mcfadden, B. Shojaei, and C. J. Palmstrøm, "Gating of High-Mobility InAs Metamorphic Heterostructures," *Applied Physics Letters*, vol. 105, no. 26, p. 262 105, 2014. DOI: 10.1063/1.4905370.

[22] A. T. Hatke, T. Wang, C. Thomas, G. C. Gardner, and M. J. Manfra, "Mobility in Excess of 10^6 cm^2/Vs in InAs Quantum Wells Grown on Lattice Mismatched InP substrates," *Applied Physics Letters*, vol. 111, no. 14, p. 142 106, 2017. DOI: 10.1063/1.4993784.

[23] J. Shabani, M. Kjaergaard, H. J. Suominen, Y. Kim, F. Nichele, K. Pakrouski, T. Stankevic, R. M. Lutchyn, P. Krogstrup, R. Feidenhans'l, S. Kraemer, C. Nayak, M. Troyer, C. M. Marcus, and C. J. Palmstrøm, "Two-Dimensional Epitaxial Superconductor-Semiconductor Heterostructures: A Platform for Topological Superconducting Networks," *Physical Review B*, vol. 93, no. 15, 2016. DOI: 10.1103/physrevb.93.155402.

[24] F. Nichele, A. C. C. Drachmann, A. M. Whiticar, E. C. T. O'Farrell, H. J. Suominen, A. Fornieri, T. Wang, G. C. Gardner, C. Thomas, A. T. Hatke, P. Krogstrup, M. J. Manfra, K. Flensberg, and C. M. Marcus, "Scaling of Majorana Zero-Bias Conductance Peaks," *Physical Review Letters*, vol. 119, no. 13, 2017.

[25] W. M. Haynes, T. J. Bruno, and D. R. Lide, *CRC Handbook of Chemistry and Physics*. Taylor & Francis, 2016.

[26] J. S. Blakemore, "Semiconducting and Other Major Properties of Gallium Arsenide," *Journal of Applied Physics*, vol. 23, 1982.

[27] D. Pettifor, *Bonding and Structure of Molecules and Solids*. Clarendon Press, 1995.

[28] A. Y. Cho, "GaAs Epitaxy by a Molecular Beam Method: Observations of Surface Structure on the (001) Face," *Journal of Applied Physics*, vol. 42, no. 5, pp. 2074–2081, 1971.

[29] I. Markov, E. Stoycheva, and D. Dobrev, "Electrolytic Epitaxial Nucleation and Growth of Cu on Ag(111)," *Communications in Department of Chemistry Bulgarian Academy of Sciences*, vol. 3, no. 377, 1978.

[30] J. Massies and N. Linh, "On the Growth of Silver on GaAs{001} Surfaces," *Journal of Crystal Growth*, vol. 56, no. 1, pp. 25–38, 1982.

[31] J. Massies and N. Linh, "Epitaxial Relationships between Al, Ag and GaAs{001} Surfaces," *Surface Science*, vol. 114, no. 1, pp. 147–160, 1982.

[32] J. Massies and N. Linh, "Ag M4, 5N4, 5N4, 5 Auger Lineshape Variation during the Epitaxial Growth of Ag onto GaAs{001}," *Journal de Physique*, vol. 43, no. 6, pp. 939–944, 1982.

[33] A. G. Cullis and R. F. C. Farrow, "A Study of the Structure and Properties of Epitaxial Silver Deposited by Atomic Beam Techniques on (001) InP," *Thin Solid Films*, vol. 58, no. 1, pp. 197–202, 1979.

[34] K. Morita, K. Soda, K. Katoh, and M. Hanebuchi, "Atomic Structures of Au and Ag Films Epitaxially Grown on the InP(001)-p(2×4)," *Journal of Electronic Materials*, vol. 25, pp. 727–731, 1996.

[35] A. Y. Cho, "Recent Developments in Molecular Beam Epitaxy (MBE)," *Journal of Vacuum Science and Technology*, vol. 16, no. 2, pp. 275–284, 1979. DOI: 10.1116/1.569926.

[36] P. M. Petroff, L. C. Feldman, A. Y. Cho, and R. S. Williams, "Properties of Aluminum Epitaxial Growth on GaAs," *Journal of Applied Physics*, vol. 52, no. 12, pp. 7317–7320, 1981. DOI: 10.1063/1.328722.

[37] G. Landgren, R. Ludeke, and C. Serrano, "Epitaxial Al Films on GaAs(100) Surfaces," *Journal of Crystal Growth*, vol. 60, no. 2, pp. 393–402, 1982.

[38] C. J. Kiely and D. Cherns, "On the Atomic Structure of the Al-GaAs(100) Interface," *Philosophical Magazine A*, vol. 59, no. 1, pp. 1–29, 1989.

[39] S. Lin, J. Wu, S. Lin, M. Lo, M. Lin, and C. Liang, "Characterization of Single-Crystalline Aluminum Thin Film on (100) GaAs Substrate," *Japanese Journal of Applied Physics*, vol. 52, p. 045 801, 2013. DOI: 10.7567/jjap.52.045801.

[40] R. Ludeke, L. L. Chang, and L. Esaki, "Molecular Beam Epitaxy of Alternating Metal-Semiconductor Films," *Applied Physics Letters*, vol. 23, no. 4, pp. 201–203, 1973. DOI: 10.1063/1.1654858.

[41] W. L. Sarney, S. P. Svensson, K. S. Wickramasinghe, J. Yuan, and J. Shabani, "Reactivity Studies and Structural Properties of Al on Compound Semiconductor Surfaces," *Journal of Vacuum Science and Technology B*, vol. 36, no. 6, p. 062 903, 2018. DOI: 10.1116/1.5053987.

[42] W. L. Sarney, S. P. Svensson, A. C. Leff, W. F. Schiela, J. O. Yuan, M. C. Dartiailh, W. Mayer, K. S. Wickramasinghe, and J. Shabani, "Aluminum Metallization of III–V Semiconductors for the Study of Proximity Superconductivity," *Journal of Vacuum Science and Technology B*, vol. 38, p. 032 212, 2020.

[43] C. Thomas, R. E. Diaz, J. H. Dycus, M. E. Salmon, R. E. Daniel, T. Wang, G. C. Gardner, and M. J. Manfra, "Toward Durable Al-InSb Hybrid Heterostructures via Epitaxy of 2ML Interfacial InAs Screening Layers," *Physical Review Materials*, vol. 3, no. 12, 2019.

[44] L. Bruce and H. Jaeger, "Geometric Factors in F.C.C. and B.C.C. Metal-on-Metal Epitaxy. Part I. Deposits of Cu and Ni on (001) Ag," *Philosophical Magazine*, vol. 36, no. 6, pp. 1331–1354, 1977.

[45] W. Bollmann, "On the Geometry of Grain and Phase Boundaries I. General Theory," *Philosophical Magazine*, vol. 16, no. 140, pp. 363–381, 1967.

[46] J. Hornstra, "Dislocations in the Diamond Lattice," *Journal of Physics and Chemistry of Solids*, vol. 5, no. 1-2, pp. 129–141, 1958.

[47] D. B. Holt, "Misfit Dislocations in Semiconductors," *Journal of Physics and Chemistry of Solids*, vol. 27, no. 6-7, pp. 1053–1067, 1966.

[48] R. T. Bate, "Nanoelectronics," *Nanotechnology*, vol. 1, no. 1, pp. 1–7, 1990. DOI: 10.1088/0957-4484/1/1/001.

[49] D. B. Janes, V. R. Kolagunta, M. Batistuta, B. L. Walsh, R. P. Andres, J. Liu, J. Dicke, J. Lauterbach, T. Pletcher, E. H. Chen, and et al., "Nanoelectronic Device Applications of a Chemically Stable GaAs Structure," *Journal of Vacuum Science and Technology B: Microelectronics and Nanometer Structures*, vol. 17, no. 4, p. 1773, 1999. DOI: 10.1116/1.590824.

[50] D. Bimberg, G. Fiol, M. Kuntz, C. Meuer, M. Lämmlin, N. N. Ledentsov, and A. R. Kovsh, "High Speed Nanophotonic Devices based on Quantum Dots," *Physica Status Solidi (a)*, vol. 203, no. 14, pp. 3523–3532, 2006. DOI: 10.1002/pssa.200622488.

[51] A. Y. Cho and P. D. Dernier, "Single-Ccrystal-Aluminum Schottky-Barrier Diodes Prepared by Molecular-Beam Epitaxy (MBE) on GaAs," *Journal of Applied Physics*, vol. 49, no. 6, pp. 3328–3332, 1978. DOI: 10.1063/1.325286.

[52] T. Zheleva, K. Jagannadham, and J. Narayan, "Epitaxial Growth in Large-Lattice-Mismatch Systems," *Journal of Applied Physics*, vol. 75, no. 2, pp. 860–871, 1994. DOI: 10.1063/1.356440.

[53] R. J. Needs, "Calculations of the Surface Stress Tensor at Aluminum (111) and (110) Surfaces," *Physical Review Letters*, vol. 58, no. 1, pp. 53–56, 1987.

[54] I. Markov, *Crystal Growth for Beginners: Fundamentals of Nucleation, Crystal Growth and Epitaxy*. World Scientific, 2017.

[55] M. H. Grabow and M. H. Gilmer, "Thin Film Growth Modes, Wetting and Cluster Nucleation," *Surface Science*, vol. 194, no. 3, pp. 333–346, 1988.

[56] S. Stoyanov, "Layer Growth of Epitaxial Films and Superlattices," *Surface Science*, vol. 199, no. 1-2, pp. 226–242, 1986.

[57] E. Bauer, "Phnomenologische Theorie der Kristallabscheidung an Oberflchen. I," *Zeitschrift fr Kristallographie - Crystalline Materials*, vol. 110, no. 1-6, pp. 372–394, 1958.

[58] C. T. Horng and R. W. Vook, "The Initial Epitaxy of Cu on (111) Ag Films," *Journal of Vacuum Science and Technology*, vol. 11, no. 1, pp. 140–143, 1974.

[59] E. Bauer, H. Poppa, G. Todd, and F. Bonczek, "Adsorption and Condensation of Cu on W Single-Crystal Surfaces," *Journal of Applied Physics*, vol. 45, no. 12, pp. 5164–5175, 1974.

[60] E. Bauer, "Epitaxy of Metals on Metals," *Applications of Surface Science*, vol. 11-12, no. 1, pp. 479–494, 1982.

[61] U. Gradmann, W. Kummerle, and P. Tillmanns, "Epitaxial Growth and Ferromagnetic Order of FCC Iron Films on (111) Cu," *Thin Solid films*, vol. 34, no. 2, pp. 249–253, 1976.

[62] J. Venables, J. Derrien, and A. Janssen, "Direct Observation of the Nucleation and Growth Modes of Ag/Si(111)," *Surface Science*, vol. 95, no. 2-3, pp. 411–430, 1980.

[63] M. Hanbucken and H. Neddermeyer, "A LEED-AES Study of the Growth of Ag Films on Si(100)," *Surface Science*, vol. 114, no. 2-3, pp. 563–573, 1990.

[64] D. Bolmont, P. Chen, C. A. Sebenne, and F. Proix, "Structural and Electronic Properties of Cleaved Si(111) Upon Room-Temperature Formation of an Interface with Ag," *Physical Review B*, vol. 24, no. 8, pp. 4552–4559, 1981.

[65] W. C. Fan, N. J. Wu, and A. Ignatiev, "Observation of Ordered Structures of Sr on the Si(100) Surface," *Physical Review B*, vol. 42, no. 2, pp. 1254–1257, 1990.

[66] K. Shoji, M. Hyodo, H. Ueba, and C. Tatsuyama, "LEED/AES Studies of the Ge on Si(111) 7×7 Surface," *Japanese Journal of Applied Physics*, vol. 22, no. 2, pp. 1459–1462, 1983.

[67] M. Asai, H. Ueba, and C. Tatsuyama, "Heteroepitaxial Growth of Ge Films on the Si(100)-2×1 Surface," *Journal of Applied Physics*, vol. 58, no. 7, pp. 2577–2583, 1985.

[68] P. M. J. Maree, K. Nakagawa, F. M. Mulders, J. I. van der Veen, and K. L. Kavanagh, "Thin Epitaxial Ge-Si(111) Films: Study and Control of Morphology," *Surface Science Letters*, vol. 191, no. 3, pp. 305–328, 1987.

[69] E. Kasper, H. J. Herzog, and H. Kibbel, "A One-Dimensional SiGe Superlattice Grown by UHV Epitaxy," *Applied Physics*, vol. 8, no. 3, pp. 199–205, 1975.

[70] J. C. Bean, L. C. Feldman, A. T. Fiory, S. Nakahara, and I. K. Robinson, "Ge_xSi_{1-x}/Si Strained-Layer Superlattice Grown by Molecular Beam Epitaxy," *Journal of Vacuum Science and Technology A: Vacuum, Surfaces, and Films*, vol. 2, no. 2, pp. 436–440, 1984.

[71] P. Imperatori, D. Ferro, and V. Piacente, "Study of the Vaporization of Solid AlAs," *Journal of the Less Common Metals*, vol. 90, no. 1, pp. 57–63, 1983.

[72] J. R. Arthur, "Interaction of Ga and As_2 Molecular Beams with GaAs Surfaces," *Journal of Applied Physics*, vol. 39, no. 8, pp. 4032–4034, 1968. DOI: 10.1063/1.1656901.

[73] A. Y. Cho and J. R. Arthur, "Molecular Beam Epitaxy," *Progress in Solid State Chemistry*, vol. 10, pp. 157–191, 1975. DOI: 10.1016/0079-6786(75)90005-9.

[74] A. Y. Cho, "How Molecular Beam Epitaxy (MBE) Began and its Projection into the Future," *Journal of Crystal Growth*, vol. 201-202, pp. 1–7, 1999. DOI: 10.1016/s0022-0248(98)01265-2.

[75] W. P. Mccray, "MBE Deserves a Place in the History Books," *Nature Nanotechnology*, vol. 2, no. 5, pp. 259–261, 2007. DOI: 10.1038/nnano.2007.121.

[76] M. Knudsen, "Experimentelle Bestimmung des Druckes gesttigter Quecksilberdämpfe bei 0^o und hheren Temperaturen," *Annalen der Physik*, vol. 334, no. 6, pp. 179–193, 1909. DOI: 10.1002/andp.19093340614.

[77] C. Thomas, A. Hatke, A. Tauz, R. Kallaher, T. Wu, T. Wang, R. E. Diaz, G. C. Gardner, M. A. Capano, and M. J. Manfra, "High-Mobility InAs 2DEGs on GaSb Substrates: A Platform for Mesoscopic Quantum Transport," *Physical Review Materials*, vol. 2, no. 10, 2018.

[78] J. H. Neave and J. A. Joyce, "Structure and Stoichiometry of {100} GaAs Surfaces during Molecular Beam Epitaxy," *Journal of Crystal Growth*, vol. 44, no. 4, pp. 387–397, 1978.

[79] E. Ruska, "The Early Development of Electron Lenses and Electron Microscopy," *Microscopica Acta*, no. S5, pp. 1–140, 1980.

[80] P. W. Hawkes, *The Beginnings of Electron Microscopy*. Academic Press, 1985.

[81] G. I. Goldstein, D. E. Newbury, P. Echlin, D. C. Joy, C. Fiori, and E. Lifshin, *Scanning Electron Microscopy and X-ray Microanalysis*. Plenum Press, 1981.

[82] A. J. Schwartz, M. Kumar, B. L. Adams, and D. P. Field, *Electron Backscatter Diffraction in Materials Science*. Kluwer Academic, 2000.

[83] R. A. Jenkins and J. L. De Vries, *Practical X-Ray Spectrometry*. Springer, 1982.

[84] S. J. Pennycook and D. E. Jesson, "High-Resolution Z-Contrast Imaging of Crystals," *Ultramicroscopy*, vol. 37, no. 1-4, pp. 14–38, 1991.

[85] J. C. H. Spence, *Experimental High-Resolution Electron Microscopy*. Oxford U. Press, 1988.

[86] J. C. H. Spence, "Imaging Dislocation Cores - The Way Forward," *Philosophical Magazine*, vol. 86, no. 29-31, pp. 4781–4796, 2006.

[87] P. Hirsch, A. Howie, R. Nicholson, D. W. Pashley, and M. J. Whelan, *Electron Microscopy of Thin Crystals*. Krieger, 1977.

[88] H. H. Rose, "Optics of high-performance electron Microscopes," *Science and Technology of Advanced Materials*, vol. 9, no. 1, p. 014 107, 1991.

[89] R. Erni, D. Marta, C. K. Rossell, and U. Dahmen, "Atomic-Resolution Imaging with a Sub-50-pm Electron Probe," *Physical Review Letters*, vol. 102, p. 096 101, 2009.

[90] S. J. Pennycook, M. Varela, C. J. D. Hetherington, and A. I. Kirkland, "Materials Advances through Aberration-Corrected Electron Microscopy," *MRS Bulletin*, vol. 31, pp. 36–43, 2011.

[91] C. Kisielowski, B. Freitag, M. Bischoff, H. van Lin, S. Lazar, G. Knippels, P. Tiemeijer, M. van der Stam, S. von Harrach, M. Stekelenburg, M. Haider, H. Muller, P. Hartel, B. Kabius, D. Miller, I. Petrov, E. Olson, T. Donchev, E. A. Kenik, A. Lupini, J. Bentley, S. Pennycook, A. M. Minor, A. K. Schmid, T. Duden, V. Radmilovic, Q. Ramasse, R. Erni, M. Watanabe, E. Stach, P. Denes, and U. Dahmen, "Detection of Single Atoms and Buried Defects in Three Dimensions by Aberration-Corrected Electron Microscopy with 0.5 Information Limit," *Microscopy and Microanalysis*, vol. 14, no. 5, pp. 469–477, 2008.

[92] R. Erni, *Aberration-Corrected Imaging in Transmission Electron Microscopy*. Imperial College Press, 2010.

[93] D. B. Williams, C. B. Carter, and J. C. H. Spence, *Transmission Electron Microscopy. A Textbook for Materials Science*. Springer, 2009.

[94] C. A. Volkert and A. M. Minor, "Focused Ion Beam: Microscopy and Micromachining," *Philosophical Magazine*, vol. 32, no. 5, pp. 389–399, 2007.

[95] P. F. Fewster, "Reciprocal Space Mapping," *Critical Reviews in Solid State and Material Sciences*, vol. 22, no. 2, pp. 69–110, 1997.

[96] Y. Cordier and D. Ferre, "InAlAs Buffer Layers Grown Lattice Mismatched on GaAs with Inverse Steps," *Journal of Crystal Growth*, vol. 201-202, pp. 263–266, 1999.

[97] X. Wallart, J. Lastennet, D. Vignaud, and F. Mollot, "Performances and Limitations of InAs/InAlAs Metamorphic Heterostructures on InP for High Mobility Devices," *Applied Physics Letters*, vol. 87, no. 8, p. 043 504, 2005.

[98] B. Shojaei, A. C. Drachmann, M. Pendharkar, D. J. Pennachio, M. P. Echlin, P. G. Callahan, S. Kraemer, T. M. Pollock, C. M. Marcus, and C. J. Palmstrøm, "Limits to Mobility in InAs Quantum Wells with Nearly Lattice-Matched Barriers," *Physical Review B*, vol. 94, no. 24, 2016.

[99] J. Vallin, M. Mongy, K. Salama, and O. Beckman, "Elastic Constants of Aluminum," *Journal of Applied Physics*, vol. 35, no. 6, pp. 1825–1826, 1964.

[100] T. Zheleva, K. Jagannadham, and J. Narayan, "Epitaxial growth in large-lattice-mismatch systems," *Journal of Applied Physics*, vol. 75, no. 2, pp. 860–871, 1994. DOI: 10.1063/1.356440.

[101] D. A. Brine and R. A. Young, "Common Epitaxial Features of Various Thin Film Textures," *The Philosophical Magazine: A Journal of Theoretical Experimental and Applied Physics*, vol. 8, no. 88, pp. 651–662, 1963.

[102] B. Mutaftschiev, *The Atomistic Nature of Crystal Growth*. Springer, 2001.

[103] J. D. Clayton, *Nonlinear Mechanics of Crystals*. Springer, 2010.

[104] J. P. Hirth and J. Lothe, *Theory of Dislocations*. Krieger Pub. Co, 1992.

[105] P. F. Fewster, "Nucleation of Vapor Deposits," *Journal of Chemical Physics*, vol. 37, no. 10, p. 2182, 1962.

[106] T. N. Rhodin and D. Walton, *Metal Surfaces: Structure, Energetics and Kinetics*. American Society for Metals, 1963.

[107] Z. Li, H. Xu, and S. Gong, "Texture Formation Mechanism of Vapor-Deposited FCCThin Film on Polycrystal or Amorphous Substrate," *Journal of Chemical Physics B*, vol. 108, no. 39, pp. 15 165–15 171, 2004.